

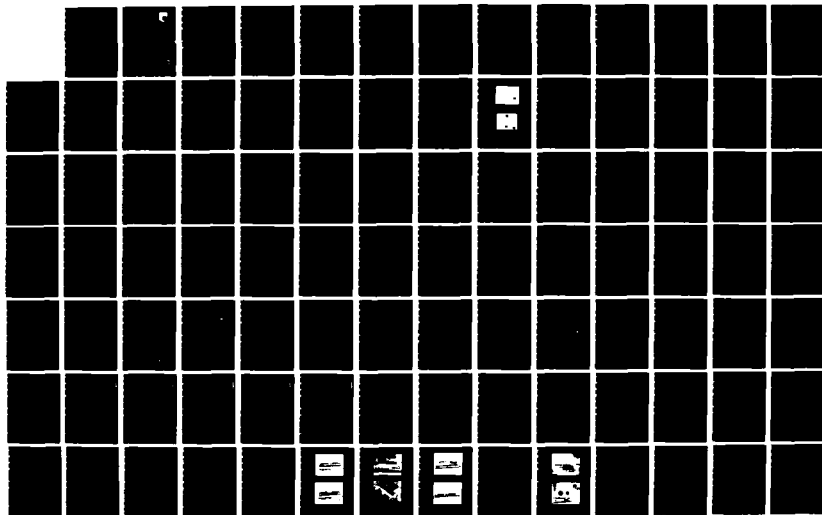
NO-A177 448

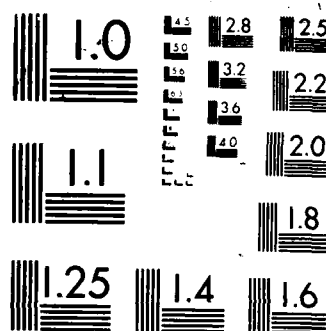
MULTIPLE COUPLED WAVEGUIDE LASER ARRAY(U) SCHAFER (W J) 1/2
ASSOCIATES INC CHELMSFORD MA D G YOUHANS 05 NOV 86
WJSA-FR-86-014 AFMAL-TR-86-2053 F33615-84-C-2445

UNCLASSIFIED

F/G 20/5

NL





MICROCOPY RESOLUTION TEST CHART

U.S. GOVERNMENT PRINTING OFFICE: 1963 O 344-100

2

AFWAL-TR-86-2053



MULTIPLE COUPLED WAVEGUIDE LASER ARRAY

Douglas G. Youmans
W. J. Schafer Associates, Inc.
321 Billerica Road
Chelmsford, MA 01824

November 1986

Final Report for Period July 1984 - June 1986

Approved for public release; distribution unlimited.

AERO PROPULSION LABORATORY
AIR FORCE WRIGHT AERONAUTICAL LABORATORIES
AIR FORCE SYSTEMS COMMAND
WRIGHT-PATTERSON AIR FORCE BASE, OHIO 45433

DTIC
ELECTE
MAR 06 1987
S E D

97 2 0 013

AD-A177 448

DTIC FILE COPY

NOTICE

When Government drawings, specifications, or other data are used for any purpose other than in connection with a definitely related Government procurement operation, the United States Government thereby incurs no responsibility nor any obligation whatsoever; and the fact that the Government may have formulated, furnished, or in any way supplied the said drawings, specifications, or other data, is not to be regarded by implication or otherwise as in any manner licensing the holder or any other person or corporation, or conveying any rights or permission to manufacture, use, or sell any patented invention that may in any way be related thereto.

This report has been reviewed by the Information Office and is releasable to the National Technical Information Service (NTIS). At NTIS, it will be available to the general public, including foreign nations.

This technical report has been reviewed and is approved for publication.




PETER BLETZINGER
Electronics Engineer
Power Components Branch
Aerospace Power Division
Aero Propulsion Laboratory



WILLIAM A. SEWARD, Major, USAF
TAM, Advanced Plasma Research
Power Components Branch
Aerospace Power Division
Aero Propulsion Laboratory

FOR THE COMMANDER



JAMES D. REAMS
Chief, Aerospace Power Division
Aero Propulsion Laboratory

"If your address has changed, if you wish to be removed from our mailing list, or if the addressee is no longer employed by your organization please notify AFWAL/POOC, WPAFB, OH 45433-6563 to help us maintain a current mailing list."

Copies of this report should not be returned unless return is required by security considerations, contractual obligations, or notice on a specific document.

REPORT DOCUMENTATION PAGE

1a. REPORT SECURITY CLASSIFICATION Unclassified			1b. RESTRICTIVE MARKINGS AD-AM7448		
2a. SECURITY CLASSIFICATION AUTHORITY			3. DISTRIBUTION/AVAILABILITY OF REPORT Approved for public release; distribution unlimited		
2b. DECLASSIFICATION/DOWNGRADING SCHEDULE					
4. PERFORMING ORGANIZATION REPORT NUMBER(S) WJSA-FR-86-014			5. MONITORING ORGANIZATION REPORT NUMBER(S) AFWAL-TR-86-2053		
6a. NAME OF PERFORMING ORGANIZATION W. J. Schafer Assoc, Inc.		6b. OFFICE SYMBOL (If applicable)		7a. NAME OF MONITORING ORGANIZATION Aero Propulsion Laboratory (AFWAL/POOC) Air Force Wright Aeronautical Laboratories	
6c. ADDRESS (City, State, and ZIP Code) 321 Billerica Road Chelmsford, MA 01824-4191			7b. ADDRESS (City, State, and ZIP Code) Air Force Systems Command Wright-Patterson Air Force Base, OH 45433		
8a. NAME OF FUNDING/SPONSORING ORGANIZATION Power Components Branch		8b. OFFICE SYMBOL (If applicable) AFWAL/POOC-3		9. PROCUREMENT INSTRUMENT IDENTIFICATION NUMBER F33615-84-C-2445	
8c. ADDRESS (City, State, and ZIP Code) Air Force Wright Aeronautical Laboratories Wright-Patterson AFB, OH 45433			10. SOURCE OF FUNDING NUMBERS		
			PROGRAM ELEMENT NO. 61102F	PROJECT NO. 2301	TASK NO. S2
			WORK UNIT ACCESSION NO. 34		
11. TITLE (Include Security Classification) Multiple Coupled Waveguide Laser Array					
12. PERSONAL AUTHOR(S) Douglas G. Youmans					
13a. TYPE OF REPORT Final Report		13b. TIME COVERED FROM 840701 TO 860602		14. DATE OF REPORT (Year, Month, Day) 861105	
15. PAGE COUNT 137					
16. SUPPLEMENTARY NOTATION					
17. COSATI CODES			18. SUBJECT TERMS (Continue on reverse if necessary and identify by block number)		
FIELD	GROUP	SUB-GROUP			
20	05		Laser, waveguide, infrared, mode coupling, multiple waveguide		
19. ABSTRACT (Continue on reverse if necessary and identify by block number)					
<p>The purpose of this effort was to extend the principle of waveguide mode coupling previously established for two waveguides to a two-dimensional array. In the theoretical portion of the program, two-dimensional array mode relative oscillator strengths (E-field distributions) were derived analytically for the first time. Fourier analysis of these array-modes indicated that almost an $(nxm)^2$ increase (as for an array which is superimposed into one waveguide) in the far-field peak irradiance distribution would be achieved. The experimental program employed 1x7 and 2x3 arrays. Severe vacuum and materials problems were encountered with the 1x7 array. The 2x3 array achieved output powers of up to 8W per channel; on installation of ZnSe coupling windows the power decreased by an order of magnitude. Lasing could be achieved with all channels. No phase-locking was observed with either the 1x7 or 2x3 array for any of twenty different resonator configuration employed, including those using focussed and unfocussed gratings. "Folded resonator" modes were found to dominate certain resonator configurations. Coupling analysis indicated that very little radiation could leak between adjacent waveguides (contd)</p>					
20. DISTRIBUTION/AVAILABILITY OF ABSTRACT <input type="checkbox"/> UNCLASSIFIED/UNLIMITED <input checked="" type="checkbox"/> SAME AS RPT. <input type="checkbox"/> DTIC USERS			21. ABSTRACT SECURITY CLASSIFICATION Unclassified		
22a. NAME OF RESPONSIBLE INDIVIDUAL Peter Bletzinger			22b. TELEPHONE (Include Area Code) (513) 255-2923		22c. OFFICE SYMBOL AFWAL/POOC-3

SECURITY CLASSIFICATION OF THIS PAGE

Block 19 Continued

when using good optical quality ZnSe plates. Instead of using coupling between the waveguides, which proved to be technically very difficult to achieve, a better method may be the use of a phase grating in a common cavity, as suggested for semiconductor laser arrays.

Accession For	
NTIS GRA&I	<input checked="" type="checkbox"/>
DTIC TAB	<input type="checkbox"/>
Unannounced	<input type="checkbox"/>
Justification	
By	
Distribution/	
Availability Codes	
Dist	Avail and/or Special
A-1	



SUMMARY

The objective of this research effort was to carry out experiments to investigate a two-dimensional waveguide CO_2 laser array. Under a previous contract we demonstrated phase-locking of two parallel waveguide lasers separated by ZnSe plates. Stationary interference fringes and increased far-field irradiances were observed.

In the work reported here, we fabricated and tested a 1x7 and a 2x3 waveguide laser array employing DC excitation. We also examined the exact mechanism of mode coupling, computed the relative oscillator strengths for both one dimensional and two dimensional array-modes, and analyzed the far-field irradiance distributions of these array-modes.

We obtained output power of up to 8 watts per channel, and simultaneous lasing on 6 channels in the 1x7 array and 6 channels in the 2x3 array. The single channel output power was smaller by a factor of 10 below that achieved earlier with Al_2O_3 walls and identical optics due to increased distributed optical loss from the ZnSe walls. Also, the segmented walls and high voltage DC excitation resulted in cross-channel discharges and some plasma oscillations which reduced outputs when more than one channel was excited. No phase-locking was observed with either the 1x7 or 2x3 array for any of the twenty resonator configurations employed. "Folded resonator" modes were found to dominate certain resonator configurations. The results of the coupling analysis indicated that very little radiation could leak between adjacent waveguides when using good optical quality ZnSe plates. The two devices had been fabricated at this point and could not be modified to increase coupling without damaging them.

Two-dimensional array mode relative oscillator strengths (E-field distributions) were derived analytically for the first time. In addition Fourier analysis of these array-modes indicated that almost an

$(nxm)^2$ increase in the far-field peak irradiance distribution would be achieved. For example, for a 2×7 array an increase of 177 in the far-field irradiance peak, relative to a single laser, would be achievable versus $(2 \times 7)^2$ or 196 for a perfect summation.

Additional coupling between waveguides is needed in order to attain phase-locking. An antireflection coating on each plate would increase coupling without greatly changing the HE_{11} mode of an individual waveguide. Also, beveling the ends of each ZnSe plate would reflect leaked radiation into the adjacent waveguide increasing coupling. Finally, transverse or longitudinal RF excitation is recommended to reduce cross-channel discharges and plasma oscillations.

TABLE OF CONTENTS

<u>Section</u>	<u>Title</u>	<u>Page</u>
1.0	INTRODUCTION	1
2.0	WAVEGUIDE CO ₂ LASER TECHNOLOGY STATUS	
2.1	Waveguide Laser Modes and Attenuation Coefficients	3
2.2	Waveguide Input/Output Coupling Losses	5
2.3	Rigrod Output Power Analysis	6
2.4	Arrays of Waveguide Lasers	8
3.0	ELECTRIC FIELD DISTRIBUTION FOR WAVEGUIDES SEPARATED BY ZnSe WINDOWS	11
3.1	Refraction Angles of Waveguide Modes and Leaked Radiation	19
3.2	Power Flow into the ZnSe Walls	21
3.3	Coupling of the Leaked Radiation into the Adjacent Channel	23
3.4	Coupling Coefficient for TM Polarization	28
4.0	CALCULATION OF ARRAY-MODE (SUPERMODE) RELATIVE OSCILLATOR STRENGTHS	30
4.1	Two Dimensional Array-Mode Oscillator Strengths.	32
5.0	ARRAY-MODE FAR-FIELD ENERGY DISTRIBUTION STUDIES	41
6.0	EXPERIMENTAL RESULTS	55
6.1	One by Seven Array Device	72
6.2	Two by Three Array Device	94
7.0	CONCLUSIONS AND RECOMMENDATIONS	131
	REFERENCES	135

LIST OF FIGURES

<u>Number</u>	<u>Title</u>	<u>Page</u>
1.	Cutaway Drawing of the Leaky-Waveguide CO ₂ Laser	9
2.	Typical Noncoherent Summation, 1x2 Array	10
3.	Coherent Summation, 1x2 Array	10
4.	E-Field Functions	12
5.	Transverse E-Field Analytical Functions	18
6.	Electric Field of Parallel Waveguides with Optimum In-Phase Coupling Through ZnSe	22
7.	Horizontal Axis Calibration and Magnitude Calibration of FFT Analysis	42
8.	Far-Field Patterns of $v = 1$ Supermodes for 1x2 Through 1x7 Arrays	44
9.	Far-Field Magnitude of Higher Order Supermodes for 1x7 Array	46
10.	Far-Field Pattern of Slightly Truncated Best Fit TEM ₀₀ Gaussian Mode	50
11.	Far-Fields of Fundamental Supermodes of 1x2 Through 1x7 Linear Arrays - TEM ₀₀ Individual Modes	51
12.	Far-Field Pattern of Uniform (No Supermode) Phase-Locked Array of Seven HE ₁₁ Mode Lasers	53
13.	Far-Field of Fundamental Supermode of Seven HE ₁₁ Waveguide Lasers Separated by 0.5 mm	54
14.	Thermal Conductivity of Combat Boron Nitride	56
15.	Single-Channel Test Device	57
16.	Test Channel Discharge Current vs Voltage	59
17.	Test Channel Power Loading	60
18.	Test Channel Power Loading	61
19.	Test Channel Resistivity	62
20.	Test Channel Resistivity	63
21.	Waveguide Array Experiment	65
22.	IR Grating Selection	68
23.	Waveguide Array Gas Flow System	71
24.	Power Supply for Split-Discharge Waveguide Laser Array (Six)	73
25.	Hippotronics Power Pack Schematic	74
26.	Waveguide Array (1x7) External Structure	75
27.	1x7 Waveguide Array End View	76
28.	1x7 Array Device Structures (a, b, c, d, e, f)	77
29.	1x7 Device with Gas Flow, Vacuum, Water and Electrical Connections	81
30.	1x7 Device with Gas Flow Controls, Gas Tanks, and Pressure Gauges	81
31.	Intensity Distribution of Channels 1 to 7 at a Distance of 76 cm	87

LIST OF FIGURES (Continued)

<u>Number</u>	<u>Title</u>	<u>Page</u>
32.	Multichannel Lasing Output Distribution at a Distance of 76 cm	89
33.	Representative Mode Shapes at 10 cm Distance	90
34.	Representative Mode Shapes at 14 cm Distance	91
35.	Discharge Current vs Voltage	93
36a.	One Half of Macor 2x3 Waveguide Device	95
36b.	Closeup of Cooling Channels, Electrode Insertion Holes and Electrode Pins	95
37.	Side View and End View of 2x3 Array Device	97
38.	Representative Mode Shapes	99
39.	2x3 Device Channel Numbering, Output End	100
40.	Far-Field Patterns Due to Simultaneous Channel Lasing Al_2O_3 Separated 2x3 Device	101
41.	Discharge Current vs Voltage 2x3 Device	103
42.	Rigrod Analysis 2x3 Device, Al_2O_3 Plates	105
43.	Mode Shapes with Spherical Copper Mirror/90% Reflector Individual Waveguides Separated by Al_2O_3 Plates	106
44.	Folded Cavity Resonator Mode Geometries	107
45.	Folded Resonator Mode of Channels #2 and #5 Separated by Al_2O_3 Plates, 9" R.C. Copper Mirror	108
46.	Diagonal-Folded Resonator Mode of Channels #1 and #5 Separated by Al_2O_3 Plates, 9" R.C. Copper Mirror	110
47.	Reflection Grating Mode Structures, Grating at 4.1 cm Channels Separated by Al_2O_3	111
48.	Folded Cavity Mode, #2 and #5, ZnSe Walls, 9-inch R.C. Copper Mirror	115
49.	Folded Cavity Mode, #2 and #3, ZnSe Walls, Lens with Flat Copper Mirror	117
50.	Two Diagonal Folded Cavity Modes, #2/#6 and #3/#5, ZnSe Walls, Lens with Flat Mirror	119
51.	Two Long Diagonal-Folded Cavity Modes, #1/#6 and #3/#4, ZnSe Walls, Lens with Flat Mirror	121
52.	Three Folded Cavity Modes #1/#6, #3/#4, #2/#5, ZnSe Walls, Lens with Flat Mirror	122
53.	Folded Cavity Mode #1/#3, Vertical Detector, 5% O.C., Focal Length 6.25 cm, z = 54 cm	124
54.	Folded Cavity Mode #1/#3 and #2, Vertical Detector, 1% O.C., Focal Length 25 cm, z = 58 cm	124
55.	Channels #4, #5, #6, ZnSe Walls, Flat Mirror Only, 5% O.C., z = 59 cm	126

LIST OF FIGURES (Continued)

<u>Number</u>	<u>Title</u>	<u>Page</u>
56.	Channels #5 and #6, ZnSe Walls, Grating Only, 1% O.C., Detector Vertical, $z = 47$ cm	128
57.	Channels #1 and #2, ZnSe Walls, Grating Only, 1% O.C., Detector Vertical, $z = 52$ cm	128
58.	Channels #2 and #3, ZnSe Walls, Grating Only, 4% O.C., Detector Vertical, $z = 45$ cm	129
59.	Channels #2 and #5, ZnSe Walls, Grating Only 4% O.C., Detector Horizontal, $z = 45$ cm	129
60.	Binary Phase-Grating Combination Resonator for nxm Array of Waveguide Lasers	133

LIST OF TABLES

<u>Section</u>	<u>Title</u>	<u>Page</u>
I.	Array-Modes for 1x2 Through 1x7 Arrays	33
II.	Array-Modes: Rectangular Coordinates	36
III.	Array-Modes: Cylindrical Coordinate (Honeycomb Structure)	39
IV.	Summary of Tested Resonator Configurations Using ZnSe Walls	131

1.0 INTRODUCTION

Waveguide CO_2 lasers are technologically well developed and are a widely used source of coherent laser radiation. Applications have included laser designators, master oscillators, local oscillators, tunable IR spectroscopy, low-power cutting and heating of materials, and more recently as coherent laser radar sources.

A typical waveguide CO_2 laser consists of a bore or groove one or two millimeters in cross-section in a ceramic or similar material. An electrical discharge is run down or across the bore to excite the gain medium. The bore confines or "guides" the IR radiation, so the recirculating radiation does not obey the laws of free space propagation as in conventional lasers. Because the bore confines both the gain medium and the laser radiation to the same region, very compact and reasonably efficient devices are possible. A typical waveguide CO_2 laser might be packaged into a 2" x 2" x 12" box having an output power of 30-W multiline.

In section 2.0 a brief review of waveguide CO_2 laser technology is given. It is shown that gain saturation in single channel waveguide CO_2 lasers limits output power to about 40 W single line, single mode. Beyond this point wavefront aberrations, higher order modes, and multiline lasing begin to occur. More single mode coherent laser power may be obtained from a phase-locked array of waveguides. Previous work, carried out under Air Force contract F33615-82-C-2217, in which we attained phase-locking of a 1x2 waveguide laser, is also reviewed in Section 2.0.

In Section 3.0 an exact electric field distribution across a gas-filled waveguide bounded by ZnSe walls is calculated. The strength of the leaked radiation is also calculated. We show that "trapping" of the leaked radiation severely reduces the amount of energy getting into an adjacent waveguide.

In order to determine what electric field distribution should occur in a phased-locked array, the relative oscillator strengths of one dimensional and two dimensional array-modes or "supermodes" are derived in Section 4.0. In Section 5.0 the far-field energy distributions of these various laser arrays are computed. The results demonstrate that somewhat less than an $(mxn)^2$ increase in the peak of the far-field laser irradiance distribution results for rectangular arrays. There is still a considerable increase in the far-field "photons in the bucket" over a single waveguide laser.

In Section 6.0 the experimental results are presented. While the 1×2 array demonstrated phase-locking, neither the outputs of the 1×7 array nor the 2×3 array demonstrated phase-locking. The main difficulties suspected are the mentioned laser light trapping by the optical quality ZnSe windows and plasma oscillation and discharges between adjacent waveguides causing very low output powers. The low cavity flux levels also reduced interwaveguide coupling.

Conclusions and recommendations are given in Section 7.0. We recommend that transverse RF excitation be used to reduce both plasma oscillations and interwaveguide discharges through cracks and gaps. Thicker and longer ZnSe windows would also reduce these waveguide gaps. Also beveling of the ZnSe plate ends and antireflection coating them should improve coupling.

2.0 WAVEGUIDE CO₂ LASER TECHNOLOGY STATUS

A brief review of waveguide laser technology is presented here for reference purposes.

2.1 Waveguide Laser Modes and Attenuation Coefficients

Marcatili and Schmeltzer¹ were among the first to analyze the propagation of electro-magnetic waves in hollow dielectric waveguides. They showed that for the circular waveguide case the electric and magnetic fields were functions of Bessel functions and the modes could be circular electric, circular magnetic, or hybrid with all components present. In general, the lowest-loss mode is the hybrid mode HE₁₁:

$$HE_{11} = J_0(2.4r/a) \cos \theta \quad (1)$$

where a is the waveguide bore radius.

The HE_{mn} loss coefficient¹ is given by

$$\alpha_{nm} = \left(\frac{u_{nm}}{2\pi}\right)^2 \frac{8\lambda^2}{a^3} \operatorname{Re} \left\{ \frac{1/2(n^2 + 1)}{(n^2 - 1)^{1/2}} \right\} \quad (2)$$

where

$$u_{nm} = m^{\text{th}} \text{ root of } J_{n-1}$$

$$u_{11} = 2.405$$

$$n = n' - ik \text{ complex refractive index of waveguide material}$$

The loss coefficient is seen to be proportional to λ^2 and inversely proportional to a^3 . The bore radius cannot be made arbitrarily large, however, as this would allow higher-order transverse mode operation and not confine and control the discharge.

The loss coefficients of the HE_{11} mode for various materials are

$$\begin{aligned}\alpha_{11} &= 4.3 \times 10^{-5} \text{cm}^{-1} \text{ for BeO (ref. 2)} \\ &= 1.8 \times 10^{-3} \text{cm}^{-1} \text{ for SiO}_2 \text{ (ref. 2)} \\ &= 1.6 \times 10^{-2} \text{cm}^{-1} \text{ for ZnSe}\end{aligned}$$

for $a = 0.5 \text{mm}$ radius at $\lambda = 10.6 \mu\text{m}$.

Also, Abrams²⁻³ showed that the Gaussian TEM_{00} mode which most closely matches the EH_{11} mode is that with a $1/e^2$ intensity beam radius of

$$w_0 = 0.6435a \quad (3)$$

The rectangular case was analyzed by Krammer⁴ and Laakman and Steier⁵. Only hybrid modes, HE_{nm} , are supported having the form

$$\begin{aligned}H_x &= -E_y \sqrt{\frac{\epsilon_0}{\mu_0}} = M \begin{Bmatrix} \cos(p_1 \pi x / 2a) \\ \sin(p_2 \pi x / 2a) \end{Bmatrix} \begin{Bmatrix} \cos(q_1 \pi y / 2b) \\ \sin(q_2 \pi y / 2b) \end{Bmatrix} \\ H_z &= \pi M / 2jka \begin{Bmatrix} -p_1 \sin(p_1 \pi x / 2a) \\ p_2 \cos(p_2 \pi x / 2a) \end{Bmatrix} \begin{Bmatrix} \cos(q_1 \pi y / 2b) \\ \sin(q_2 \pi y / 2b) \end{Bmatrix} \approx 0 \\ E_z &= -\pi M \sqrt{\frac{\mu_0}{\epsilon_0}} / 2jkb \begin{Bmatrix} \cos(p_1 \pi x / 2a) \\ \sin(p_2 \pi x / 2a) \end{Bmatrix} \begin{Bmatrix} -q_1 \sin(q_1 \pi y / 2b) \\ q_2 \cos(q_2 \pi y / 2b) \end{Bmatrix} \approx 0\end{aligned} \quad (4)$$

$$p_1, q_1 \text{ odd}$$

or

$$p_2, q_2 \text{ even}$$

for the HE_{nm}^x modes with similar equations for the HE_{nm}^y modes. The waveguide is $2a \times 2b$ in dimension, M is a constant, and the mode propagates in the z direction.

The attenuation coefficient is

$$\alpha_{pq} = \frac{(p\pi)^2}{4k^2 a^3} \operatorname{Re}\left\{\frac{1}{\sqrt{n^2 - 1}}\right\} + \frac{(q\pi)^2}{4k^2 b^3} \operatorname{Re}\left\{\frac{n^2}{\sqrt{n^2 - 1}}\right\} \quad (5)$$

and for the HE_{11} ($p=1$ and $q=1$) mode with $a = b$

$$\alpha_{11} = \frac{\lambda^2}{16a^3} \operatorname{Re}\left\{\frac{n^2 + 1}{\sqrt{n^2 - 1}}\right\} \quad (5a)$$

$$\begin{aligned} &= 1.74 \times 10^{-3} \text{cm}^{-1} \text{ for ZnSe } (a = 0.5\text{mm}) \\ &= 1.6 \times 10^{-4} \text{cm}^{-1} \text{ for SiO}_2 \text{ } (a \equiv 0.5\text{mm}) \text{ (ref. 5)} \\ &= 3.0 \times 10^{-5} \text{cm}^{-1} \text{ for ReO } (a \equiv 0.5\text{mm}) \text{ (ref. 5)} \\ &= 1.8 \times 10^{-4} \text{cm}^{-1} \text{ for Al}_2\text{O}_3 \text{ } (a \equiv 0.5\text{mm}) \text{ (ref. 5)} \end{aligned}$$

Also Laakman and Steier⁵ and Henderson⁶ showed that the matching TEM_{00} beam waist is

$$\omega_0 = 0.70a \quad (6)$$

2.2 Waveguide Input/Output Coupling Losses

Degnan and Hall⁷ showed that there are three mirror (or lens) locations for maximum mode coupling (minimum loss) of the reflected radiation back into the waveguide:

1. A flat mirror at the end of the waveguide
2. A distant mirror with radius of curvature equal to the distance from the waveguide aperture
3. A mirror at the Rayleigh range, $\frac{\pi \omega_0^2}{\lambda}$, with a curvature of twice this distance

For the waveguide configurations of interest, case 1 is the important condition. Hill and Hall⁸ showed that as the flat mirror is slightly moved away from the waveguide aperture, the coupling losses for square guides are approximately given by

$$\text{loss} \cong 1310 \left(\frac{\lambda z}{2\pi a} \right)^2 \quad (7)$$

$$= 0.4\% \text{ at } z = 1 \text{ mm}$$

$$= 1.5\% \text{ at } z = 2 \text{ mm}$$

$$= 3.4\% \text{ at } z = 3 \text{ mm}$$

for $a = 1 \text{ mm}$ where z is the aperture to mirror distance. For circular guides the losses are given by

$$\text{loss} \cong 3686 \left(\frac{z\lambda}{2\pi a} \right)^2 \quad (8)$$

2.3 Rigrod Output Power Analysis

It is now possible to perform a first order analysis of the wave guide laser output power for various small signal gains and output couplings. Rigrod⁹ and Casperson¹⁰ have shown that the output power from a homogeneously broadened laser is approximately given by

$$P_{\text{out}} = \frac{I_s}{2} A t \left[\frac{2g_0 l}{t + 1} - 1 \right] \quad (9)$$

where

$$I_s = \begin{cases} 4,000\text{W/cm}^2 \text{ (100 torr) (ref. 2)} \\ 15,000\text{W/cm}^2 \text{ (200 torr) (ref. 2)} \end{cases} \text{ saturation intensity}$$

$$A = 2a \text{ mm} \times 2a \text{ mm area} \times \pi/4 \text{ (~ mode area)}$$

$$t = \text{transmission of output coupler}$$

$$g_0 = \text{small signal gain} \approx 2\%/cm \text{ as a function of pressure}$$

l = discharge length

L = round trip losses other than output transmission

$\cong 2 \times (\text{waveguide loss}) + (\text{reflector loss}) + 2 \times (\text{coupling loss})$

Note that the optimum output coupling determined by differentiating eq. (8) is given by

$$t_{\text{opt}} = (2g_0 l L)^{1/2} - L \quad (10)$$

once g_0 and round trip loss, L , are known.

In practice equation (8) reduces to

0.4 to 0.8 W/(cm length) RF excitation
0.25 to 0.5 W/(cm length) DC excitation

for well-designed waveguide CO_2 lasers. With transverse RF excitation it is easier to maintain optimum E/p (Volts/cm)/Torr for maximum g_0 over the entire length of the waveguide; hence higher output power per unit length is achievable.

As the discharge tube length is made longer in order to obtain more power, the gain of the laser gas mixture begins to saturate as characterized by the saturation parameter of equation 9. As the output power approaches typically 40W, the laser becomes multimode and multiline because of lower saturation of the higher order transverse modes and the other lasing transitions. These effects are documented in reference 11 for example. In addition to multimode and multiline effects, saturation of the media can cause large wavefront aberrations seriously degrading the far field irradiance distribution and focusability.

2.4 Arrays of Waveguide Lasers

The potential for increased laser powers using parallel arrays of lasers was realized in 1970 by Ripper and Paoli¹² as applied to semiconductor laser diodes. It has only been in the last few years, that reasonably successful phase-locking of these semiconductor laser arrays has been achieved¹³⁻¹⁵.

With respect to waveguide CO₂ lasers, WJSA demonstrated under Air Force contract F33615-82-C-2217 that it is possible to phase-lock adjacent waveguide CO₂ lasers by separating them with a transparent (at 10.6 μ m) material. The proof-of-principle device is shown in Figure 1. A typical noncoherent summation, when the two lasers were operating on different CO₂ molecular transitions, is shown in Figure 2. The laser modes were partially focussed to show the near Gaussian far-field patterns. When the two waveguides lased on to the same transition, stationary interference fringes were observed. These interference fringes were immune to mechanical shock and vibration and immune to extreme variations of discharge current in either waveguide such that lasing would have ceased ordinarily. Phase-locking was thus demonstrated. Polarization of the laser modes was found to be parallel to the ZnSe plate surfaces due to the minimum propagation loss as shown by equation (5). This is the only demonstration of waveguide CO₂ laser phase-locking published to date.

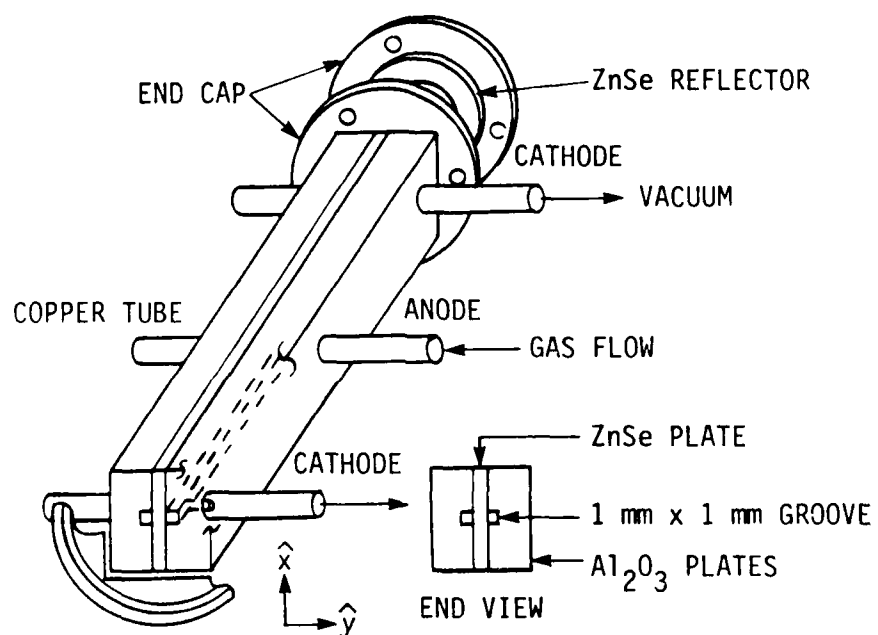
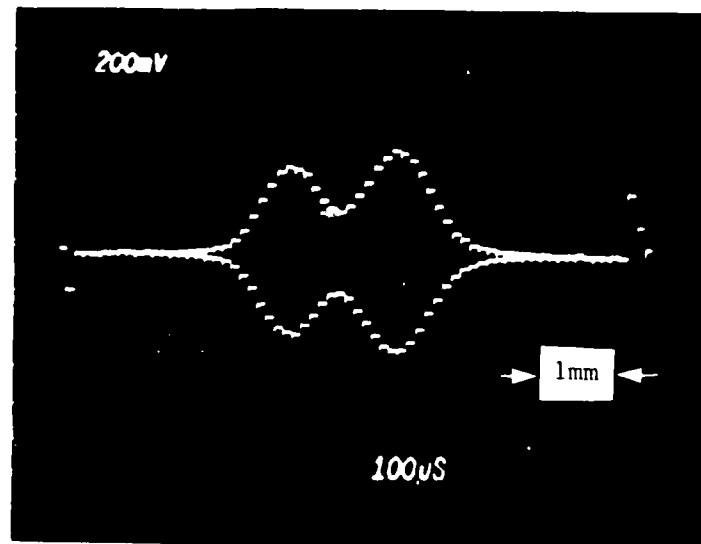
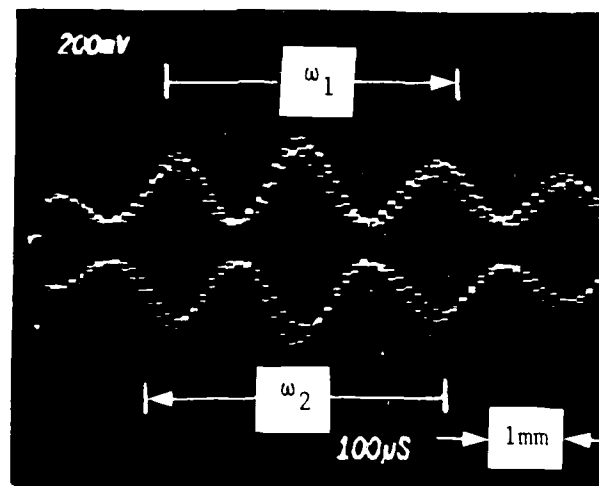


FIGURE 1. CUTAWAY DRAWING OF THE LEAKY-WAVEGUIDE CO₂ LASER



Typical noncoherent summation, partially focussed for clarity. Horizontal scale corresponds to horizontal direction in Fig. 1.

FIGURE 2. TYPICAL NONCOHERENT SUMMATION OF LASER OUTPUTS²⁹



Coherent summation of two waveguide lasers unfocussed at 35 cm from the output aperture. Horizontal scale corresponds to horizontal direction in Fig. 1.

FIGURE 3. COHERENT SUMMATION OF LASER OUTPUTS²⁹

3.0 ELECTRIC FIELD DISTRIBUTION FOR WAVEGUIDES SEPARATED BY ZnSe WINDOWS

We now present a derivation of the electric field distribution for waveguides separated by ZnSe or other transparent dielectric plates. The analysis is typical of mode propagation literature in that there are many variables but the mathematics are reasonably straightforward. Figure 4 is a drawing of a single waveguide channel bounded by two ZnSe (or other transparent dielectric) plates. Following the analytical procedures of Yariv, "Introduction to Optical Electronics", 2nd Ed., Chapter 13, the E-field distribution across a waveguide and the ZnSe window on each side may be written as shown in Figure 4:

Region 1. (ZnSe, $n = 2.4$)

$$A \exp [i(k_{x_1} x + k_z z - wt)] \quad (11)$$

Region 2. (He, N₂ CO₂, $n_0 = 1$)

$$[B \cos (k_{x_2} x) + C \sin (k_{x_2} x)] \exp [i(k_z z - wt)] \quad (12)$$

Region 3. (ZnSe, $n = 2.4$)

$$D \exp [i(-k_{x_1} x + k_z z - wt)] \quad (13)$$

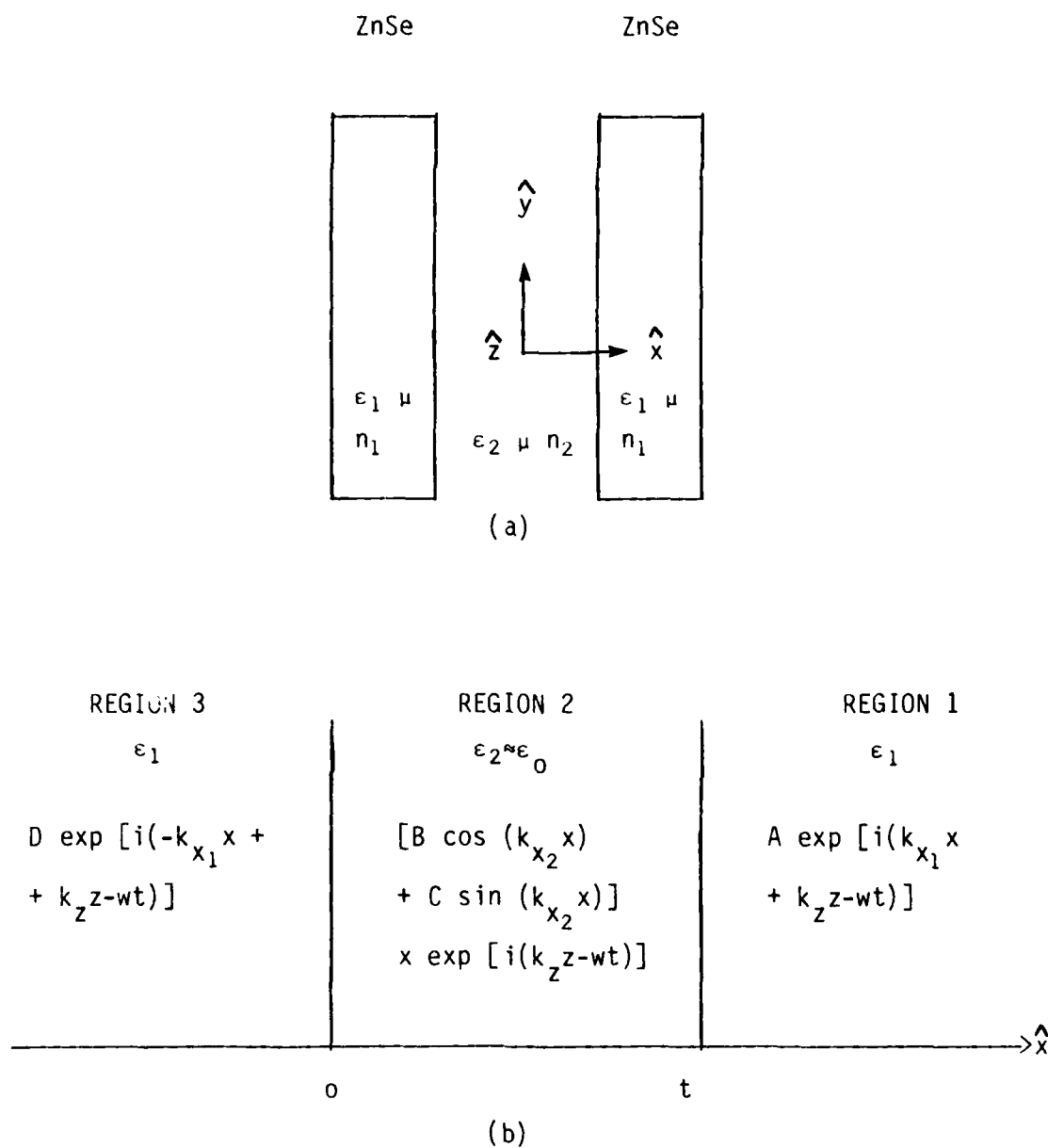


FIGURE 4. E-FIELD FUNCTIONS
(Note coordinate difference between (a) and (b))

for a "slab" waveguide analysis. Here

k_{x_1} = transverse phase constant, medium 1.

k_{x_2} = transverse phase constant, medium 2.

k_z = longitudinal or axial propagation constant.

$k_i^2 = k_z^2 + k_{x_i}^2 = n_i^2 k_0^2$ propagation constant for medium i.

$n_i^2 = \epsilon_i/\epsilon_0$ refractive index for medium i.

Substituting into Maxwell's equation:

$$\nabla^2 \vec{E}(\vec{r}) + k^2 n^2(\vec{r}) \vec{E}(\vec{r}) = 0 \quad (14)$$

which for the TE case (polarized in the y direction) becomes

$$(-k_z^2 + \frac{\partial^2}{\partial x^2}) E_y + k_i^2 E_y = 0 \quad (15)$$

and we have three equations (two of which are redundant in this case):

$$k_{x_1}^2 = k_2^2 \left(\frac{\epsilon_1}{\epsilon_2} \right) - k_z^2 \quad (16)$$

$$k_{x_2}^2 = k_2^2 - k_z^2 \quad (17)$$

$$k_{x_1}^2 = k_2^2 \left(\frac{\epsilon_1}{\epsilon_2} \right) - k_z^2 \quad (18)$$

From the continuity of E_y and $\partial E_y / \partial x$ at $x=0$ and $x=t$, there are four equations:

$$A \exp(ik_{x_1} t) - B \cos(k_{x_2} t) - C \sin(k_{x_2} t) = 0 \quad (19)$$

$$k_{x_1} A \exp(ik_{x_1} t) - iBk_{x_2} \sin(k_{x_2} t) + iCk_{x_2} \cos(k_{x_2} t) = 0 \quad (20)$$

$$B - D = 0 \quad (21)$$

$$ik_{x_2} C - k_{x_1} D = 0 \quad (22)$$

In order to have a non-trivial solution for A, B, C, and D the determinant of the matrix of coefficients from the left side of equations (19) to (22) must equal zero. This requires that

$$\tan(k_{x_2} t) = -i \frac{2k_{x_1} k_{x_2}}{k_{x_1}^2 + k_{x_2}^2} \quad (23)$$

Also, because we are looking for symmetric HE_{11} mode-like E-field solutions, the regions 1 and 3 are symmetric and $D=A$.

Using equation (16) and the fact that $k_z \approx k_2 \gg k_{x_2}$ and $\epsilon_1/\epsilon_2 = (2.4)^2$ for ZnSe,

$$k_{x_1} \approx k_2 (\epsilon_1/\epsilon_2 - 1)^{1/2} \quad (24)$$

$$= 2\pi/(\lambda_0/(2.4^2 - 1)^{1/2}) \quad (25)$$

$$= 2\pi/(10.6 \text{ } \mu\text{m}/2.18) \quad (26)$$

$$= 2\pi/4.86 \text{ } \mu\text{m} \quad (27)$$

Thus the transverse spatial variation in the ZnSe has a periodicity of $\lambda_0/2.18$ or $4.86 \text{ } \mu\text{m}$. Since the imaginary part of ϵ_1 is very small, the imaginary part of k_{x_1} is zero and there is almost no attenuation.

From equation (23)

$$k_{x_2} t = \tan^{-1} \left[-i \frac{2k_{x_1} k_{x_2}}{k_{x_2}^2 + k_{x_1}^2} \right] + n\pi \quad (28)$$

$$(k_{x_1} \gg k_{x_2}) \quad \cong \tan^{-1} \left[-i \frac{2k_{x_2}}{k_{x_1}} \right] + n\pi \quad (29)$$

$$\cong -i \frac{2k_{x_2}}{k_2(\epsilon_1/\epsilon_2 - 1)^{1/2}} + n\pi \quad (30)$$

$$\text{therefore } k_{x_2} t = \frac{n\pi}{1 + \frac{2i}{k_2 t(\epsilon_1/\epsilon_2 - 1)^{1/2}}} \quad (31)$$

$$\cong n\pi \left(1 - \frac{2i}{k_2 t(\epsilon_1/\epsilon_2 - 1)^{1/2}} - \frac{4}{k_2^2 t^2(\epsilon_1/\epsilon_2 - 1)} \right) \quad (32)$$

$$\text{Therefore } \text{Re} \{ k_{x_2} \} = \frac{n\pi}{t} \left(1 - \frac{4}{k_2^2 t^2(\epsilon_1/\epsilon_2 - 1)} \right) \quad (33)$$

$$= \frac{n\pi}{t} (1 - 6.0 \times 10^{-7}) \quad (34)$$

for $t = 2 \text{ mm}$, $k_2 = 2\pi/10.6 \text{ } \mu\text{m}$, and $\epsilon_1/\epsilon_2 = (2.4)^2$, and

$$\text{Im} \{ k_{x_2} \} = \frac{-2n\pi}{k_2^2 t^2(\epsilon_1/\epsilon_2 - 1)^{1/2}} \cong 0.56 \text{ m}^{-1} \quad (35)$$

Before using equations (24) and (33) to find the transverse E-field distribution, it is useful to find k_z , the imaginary part of which gives the propagation loss. (This is the parameter of interest in most waveguide papers.)

$$k_z^2 = k_2^2 - k_{x_2}^2 \quad (36)$$

$$= k_2^2 - \frac{n^2 \pi^2}{t^2} \left[1 - \frac{4}{k_2^2 t^2 (\epsilon_1/\epsilon_2 - 1)} - \frac{2i}{k_2 t (\epsilon_1/\epsilon_2 - 1)^{1/2}} \right]^2 \quad (37)$$

$$\cong k_2^2 \left(1 - \frac{n^2 \pi^2}{k_2^2 t^2} + i \frac{4 n^2 \pi^2}{k_2 t^3 (\epsilon_1/\epsilon_2 - 1)^{1/2}} \right) \quad (38)$$

Using an identity for the square root of a complex number and keeping higher order terms,

$$k_z \cong k_2 \left(1 - \frac{n^2 \pi^2}{2 k_2^2 t^2} \right) + i \frac{2 n^2 \pi^2}{k_2^2 t^3 (\epsilon_1/\epsilon_2 - 1)^{1/2}} \quad (39)$$

Therefore the intensity attenuation coefficient is

$$\alpha_{TE} = 2 \operatorname{Im} \{ k_z \} = \frac{4 n^2 \pi^2}{k_2^2 t^3 (\epsilon_1/\epsilon_2 - 1)^{1/2}} = \frac{\lambda^2}{t^3 (\epsilon_1/\epsilon_2 - 1)^{1/2}} \quad (40)$$

$$\cong 6.4 \times 10^{-3} \text{ m}^{-1} \text{ (ZnSe walls)}$$

and the well known $1/t^3$ and $1/(n^2_{\text{rel}} - 1)^{1/2}$ relationship for TE

polarization is seen¹ as in equation 5a.

To obtain the analytic functions for the transverse E-field, we move the coordinate system to the center of the waveguide and use the cosine term for Region 2 which is slightly different from a first-order HE_{11} cosine distribution (See equation 4):

$$E_y = \cos \left[\left(\pi/t \right) \left(1 - \frac{4}{k_2^2 t^2 (\epsilon_1/\epsilon_2 - 1)} \right) x \right] \quad 0 < x < t/2 \quad (41)$$

as shown in Figure 4. At $x = t/2$ this has a value of $2\pi/k_2^2 t^2 (\epsilon_1/\epsilon_2 - 1) \approx 9.4 \times 10^{-7}$. Thus we would expect a form of

$$E_y = -A' \sin \left[k_2 (\epsilon_1/\epsilon_2 - 1)^{1/2} (x - t/2) - \phi \right] \quad (42)$$

in Region 1. Equating equations (31) and (32) and their derivatives at $x = t/2$, the amplitude and phase delay in Region 1 are given by:

$$A' = \frac{\lambda_0}{2t(\epsilon_1/\epsilon_2 - 1)^{1/2}} \quad (43)$$

$$= 1.21 \times 10^{-3} \quad (44)$$

and

$$\phi = \sin^{-1} \left[\frac{2}{k_2 t (\epsilon_1/\epsilon_2 - 1)^{1/2}} \right] \quad (45)$$

$$\cong \frac{\lambda_0}{\pi t (\epsilon_1/\epsilon_2 - 1)^{1/2}} \quad (46)$$

$$= .044^\circ \quad (47)$$

The waveforms are shown in Figure 5.

It can be seen that the transverse E-field in the interwaveguide ZnSe window is an undamped sine wave of greatly reduced amplitude having a periodicity of $4.86 \mu\text{m}$. Across a 1-mm ZnSe plate there would be about 206 oscillations. An interwaveguide window thickness of a half-integer multiple of $\lambda_0/(\epsilon_1/\epsilon_2 - 1)^{1/2}$ or $4.86 \mu\text{m}$ would be desired so as to keep the adjacent HE_{11} modes in phase with their respective leaked radiation fields (mutual phase-locking):

HE₁₁ WAVEGUIDE MODE

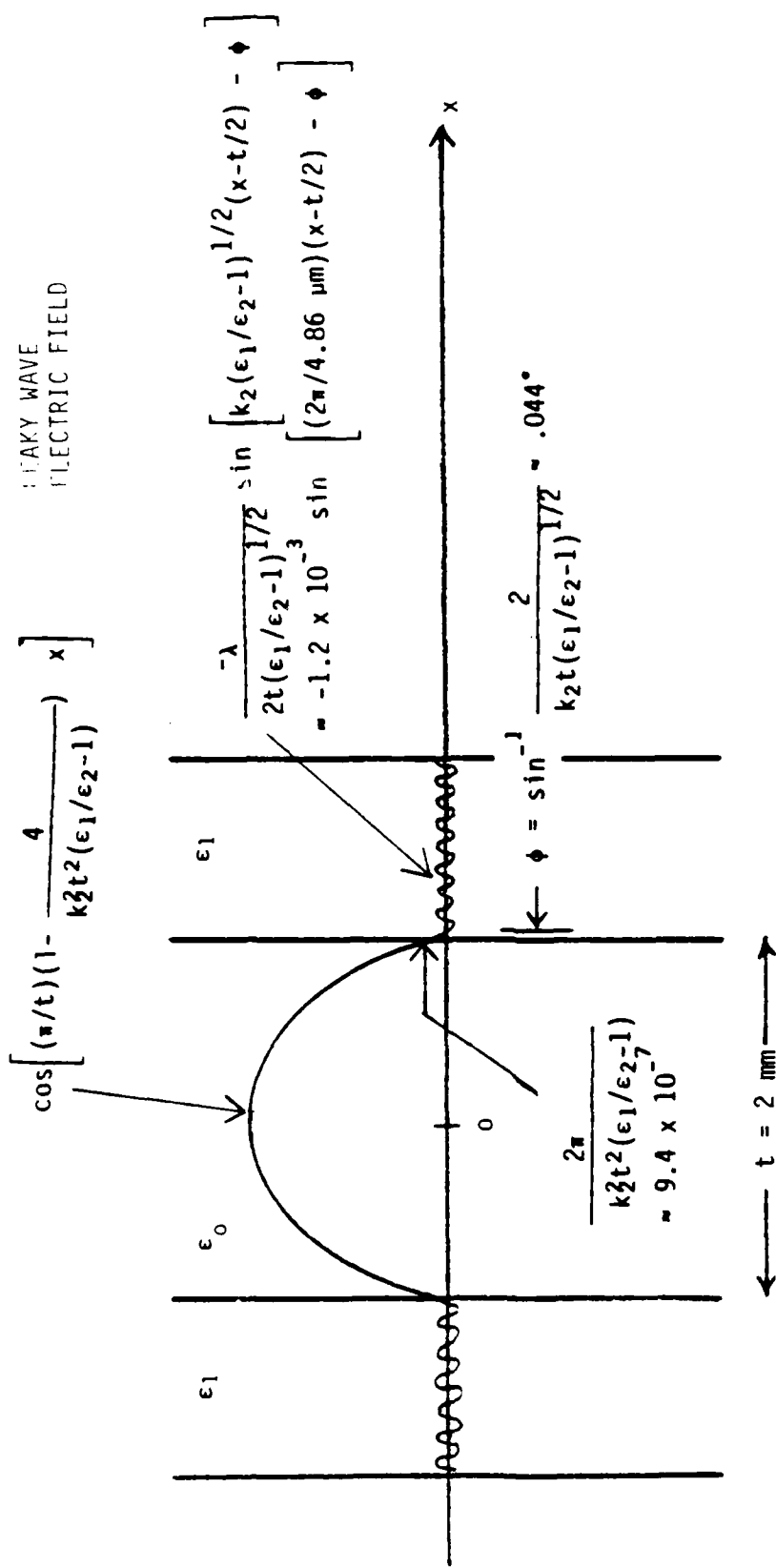


FIGURE 5. TRANSVERSE E-FIELD ANALYTICAL FUNCTIONS

$$\begin{aligned}
\text{thickness} &= (N+1/2) \lambda_0 / (\epsilon_1 / \epsilon_2 - 1)^{1/2} \\
&= (N+1/2) 4.86 \mu\text{m (ZnSe)} \\
&= 1.0036 \text{ mm for example}
\end{aligned}$$

This would lead to the formation of the lowest order array-mode, described in Section 4, and result in a single lobe far-field pattern as analyzed in Section 5.

3.1 Refraction Angles of Waveguide Modes and Leaked Radiation

Having found the \hat{x} and \hat{z} propagation constants inside the waveguide given by equations 31 (k_{x_2}) and 39 (k_z) and the x and z propagation constants in the ZnSe given by equations 24 (k_{x_1}) and 39 (k_{z_1}), it is possible now to calculate the refraction angles of the modes in the ZnSe walls. The treatment follows that for semiconductor guided laser modes¹⁶⁻¹⁹.

Inside the waveguide from equation 7 we have

$$k_z^2 + k_{x_2}^2 = k_2^2 \quad (48)$$

The angle between the z axis and \vec{k}_2 is then

$$\sin \theta_2 = \sqrt{k_2^2 - k_z^2} / k_2 \quad (49)$$

Multiply the numerator and denominator by $(\lambda_0/2\pi)$, and we have

$$\sin \theta_2 = \sqrt{n_2^2 - n_{eq}^2} / n_2 \quad (50)$$

where n_2 is the relative refractive index of the gas (≈ 1.0) and n_{eq} is defined by the literature as

$$n_{eq} \equiv k_z (\lambda_0/2\pi) \quad (51)$$

From equation (39)

$$n_{eq}^2 = \left(\frac{\lambda_0}{2\pi}\right)^2 k_2^2 \left(1 - \frac{n^2 \pi^2}{k_2^2 t^2} + i \frac{4n^2 \pi^2}{k_2^2 t^3 (\epsilon_1/\epsilon_2 - 1)^{1/2}}\right) \quad (52)$$

$$n_{eq}^2 \approx 1 - \frac{\lambda_0^2}{8t^2} \quad (53)$$

and equation (50) becomes ($n_2 \approx 1.0$)

$$\theta_2 \approx \pm \frac{\lambda_0}{\sqrt{8t}} \quad (54)$$

$$= \pm 1.87 \text{ mr} \quad (t = 2 \text{ mm}) \quad (55)$$

$$= \pm 3.75 \text{ mr} \quad (t = 1 \text{ mm}) \quad (56)$$

Thus, inside the waveguide the field is represented by two plane waves propagating at angles $\pm\theta_2$ w.r.t. z down the waveguide²⁰. This is shown greatly exaggerated in Figure 6.

Similarly inside the ZnSe walls

$$k_z^2 + k_{x_1}^2 = k_1^2 \quad (57)$$

$$\sin \theta_1 = \frac{\sqrt{k_1^2 - k_z^2}}{k_1} \quad (58)$$

$$= \frac{\sqrt{n_1^2 - n_{eq}^2}}{n_1} \quad (59)$$

$$\approx (2.4^2 - (1 - \lambda_0^2/8t^2))^{1/2}/2.4 \quad (60)$$

$$\theta_1 \approx 65.38^\circ \quad t=2 \text{ mm}, 1 \text{ mm} \quad (61)$$

(This can also be calculated using Snell's law on equation 54.)

These wavefronts are also shown in Figure 6. In this figure two waveguides are shown, and the ZnSe thickness is exactly a half-integer multiple of $\lambda_0/(\epsilon_1/\epsilon_2-1)^{1/2}$ so that the two laser channels are in perfect phase as in an ideal 1x2 array. In addition to the waves traveling to the right there will be waves traveling to the left 180° out-of-phase due to the laser Fabry Perot resonance condition.

3.2 Power Flow into the ZnSe Walls

To calculate the percentage of power flowing into each ZnSe wall, it is necessary to compute the power flow in the x direction, S_x , per unit waveguide length and the power that is being carried in the z direction, $t(S_z)$. Here, S_x and S_z are the components of the Poynting vector. The power outflow into the ZnSe is

$$S_x = 1/2 E_y H_z^* = \frac{k_x}{2\omega\mu} |A'|^2 \quad (62)$$

where μ is the magnetic permeability and ω is the E-field oscillation frequency. The power being carried by the waveguide along the waveguide axis is

$$S_z = 1/2 E_y H_x^* = \frac{k_z}{2\omega\mu} |C(=1)|^2 \quad (63)$$

Forming the ratio of S_x to tS_z and substituting from equations 14, 43, and 39

$$\frac{S_x}{tS_z} \approx \frac{k_z (\epsilon_1/\epsilon_2-1)^{1/2}}{tk_2} \left(\frac{\lambda_0^2}{4t^2(\epsilon_1/\epsilon_2-1)} \right) \quad (64)$$

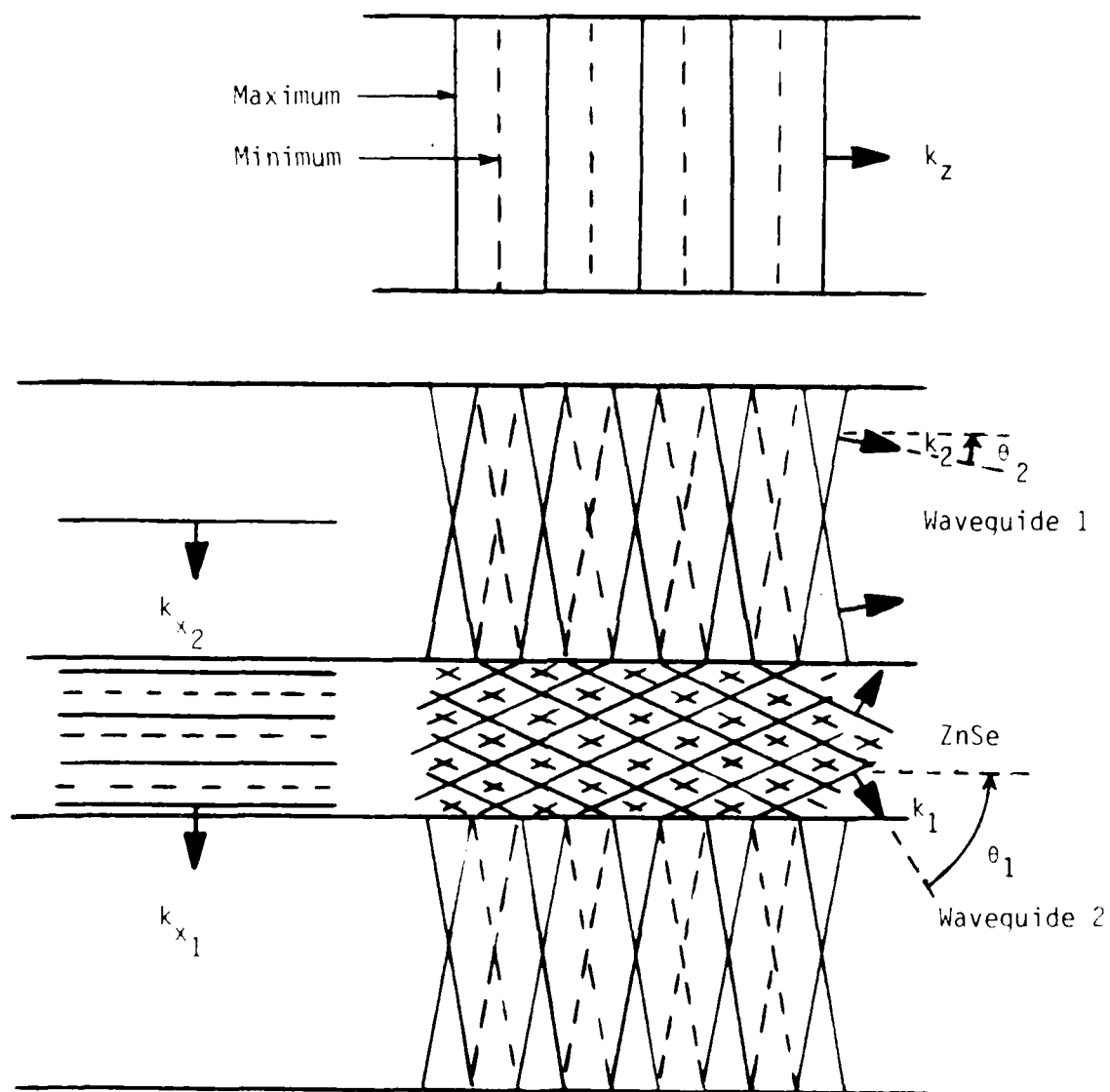


FIGURE 6. ELECTRIC FIELD OF PARALLEL WAVEGUIDES WITH OPTIMUM IN-PHASE COUPLING THROUGH ZnSe

$$= \frac{\lambda_0^2}{4t^3 (\epsilon_1/\epsilon_2 - 1)^{1/2}} \quad (65)$$

$$= 1.6 \times 10^{-3} \text{ m}^{-1} \text{ per wall (2 mm)} \quad (66)$$

$$= 1.3 \times 10^{-2} \text{ m}^{-1} \text{ per wall (1 mm)} \quad (66a)$$

Multiplying by 2 for the other ZnSe wall loss (or equivalently the $+0_2$, -0_2 waves each have one-half the power), and we see that equation 65 is identical to the imaginary part of k_z as given by equation 29 for an HE_{11} mode

$$\frac{2S_x}{tS_z} = \text{Im}(k_z) = 1/2 \alpha_{TE} \quad (67)$$

which is a good check on the analysis. We have two identical numbers for the energy lost into a ZnSe wall.

3.3 Coupling of the Leaked Radiation into the Adjacent Channel

Next it is necessary to calculate the energy getting into an adjacent waveguide. The leaked radiation propagates through the ZnSe material as shown in Figure 6 and reflects off of the ZnSe adjacent waveguide interface. The Fresnel reflection coefficient for TE polarization is given by

$$\frac{E_r}{E_i} = \frac{\cos \theta_i - \sqrt{n^2 - \sin^2 \theta_i}}{\cos \theta_i + \sqrt{n^2 - \sin^2 \theta_i}} \quad (68)$$

where $n = 1/2.4$ for internal reflection where θ_i is the angle of incidence at the ZnSe to gas interface. From equations 59 and 60.

$$\sin^2 \theta_1 = (n_1^2 - n_{eq}^2) / n_1^2 \quad (69)$$

$$= \cos^2 \theta_i = 1 - \sin^2 \theta_i \quad (70)$$

Therefore

$$\sin^2 \theta_i = \frac{1}{2.4^2} (1 - \lambda_0^2 / 8t^2) \quad (71)$$

The quantity $\sqrt{n^2 - \sin^2 \theta_i}$ from equation 68 becomes

$$\sqrt{n^2 - \sin^2 \theta_i} = \lambda_0 / \sqrt{8} (2.4) t \quad (72)$$

and equation 68 becomes

$$\frac{E_r}{E_i} = \frac{\cos \theta_i - \lambda / \sqrt{8} (2.4) t}{\cos \theta_i + \lambda / \sqrt{8} (2.4) t} \quad (73)$$

$$= \frac{\cos \theta_i (1 - \lambda_0 / \cos \theta_i \sqrt{8} nt)}{\cos \theta_i (1 + \lambda_0 / \cos \theta_i \sqrt{8} nt)} \quad (74)$$

$$\cong 1 - (2\lambda_0 / \cos \theta_i \sqrt{8} nt) \quad (75)$$

where n is redefined as 2.4. Transmission into the adjacent waveguide is thus

$$T_{TE} = 2 \lambda_0 / \cos \theta_0 \sqrt{8} nt \quad (76)$$

Since

$$\cos^2 \theta_i = 1 - \sin^2 \theta_i = 1 - 1/2.4^2 + \frac{\lambda_0^2}{8t^2 (2.4)^2} \quad (77)$$

$$\cong 1 - 1/2.4^2 \quad (78)$$

$$\cos \theta_i \cong (1 - 1/2.4^2)^{1/2} \quad (79)$$

for all waveguide thicknesses, and we have

$$T_{TE} = 2\lambda_0 / (n^2 - 1)^{1/2} \sqrt{8} t \quad (80)$$

$$= \begin{cases} 3.4 \times 10^{-3} & t = 1 \text{ mm} \\ 1.7 \times 10^{-3} & t = 2 \text{ mm} \end{cases} \quad (81)$$

Thus about 99.8% of the light is reflected off of the second ZnSe to gas interface for a single reflection.

To determine the effects of multiple internal reflections, we form an infinite series summation of the E-field transmissions after making round trip bounces through the ZnSe plate. This series reduces to

$$T' = \frac{e^{-\alpha x} e^{-i\delta} T_{TE}}{1 + e^{-2\alpha x} e^{-i2\delta} (1 - T_{TE})^2 (T_{TE})} \quad (82)$$

where

$$\begin{aligned} \delta &= \frac{2\pi}{\lambda} n_1 d \cos (\pi/2 - \theta_1) \\ d &= 1 \text{ mm (plate thickness)} \\ \alpha &\cong 0.001/2 \text{ cm}^{-1} \text{ (absorption coefficient)} \\ x &= d / \cos (\pi/2 - \theta_1) \end{aligned}$$

The refractive index of ZnSe has been approximated as completely real, and a small absorption coefficient has been included corresponding to its very small imaginary part.

The transmitted intensity coefficient is given by

$$n_0 T' T'^* = \frac{n_0 T_{TE}^2 e^{-2\alpha x}}{1 + 2(1-T_{TE})^2 T_{TE} e^{-2\alpha x} \cos 2\delta + e^{-4\alpha x} (1-T_{TE})^4 T_{TE}^2} \quad (83)$$

$$\left\{ \begin{array}{l} < \frac{T_{TE}^2 e^{-2\alpha x}}{1 - 2(1-T_{TE})^2 T_{TE}} \cong 1.01 T_{TE}^2 \quad (\text{max}) \end{array} \right. \quad (84)$$

$$\left\{ \begin{array}{l} > \frac{T_{TE}^2 e^{-2\alpha x}}{1 + 2(1-T_{TE})^2 T_{TE}} \cong 0.94 T_{TE}^2 \quad (\text{min}) \end{array} \right. \quad (85)$$

corresponding to maximum constructive and destructive interference. Assuming that the transmitted wavefronts are all in phase for the correct plate thickness as in Figure 6, the multiple-bounce E-field transmission coefficient is:

$$|n_0 T' T'^*|^{1/2} \cong \frac{T_{TE}}{[1 - 2(1-T_{TE})^2 T_{TE}]^{1/2}} \quad (86)$$

$$\cong T_{TE} \quad (87)$$

Similarly it is possible to calculate the energy transmitted back into the first waveguide from the ZnSe plate. This is somewhat different from a reflection coefficient because the light is leaked into the ZnSe and some escapes back into the original channel. Forming an infinite sum of these rays:

$$R' = \frac{e^{-2i\delta} (1-T_{TE}) T_{TE} e^{-2\alpha x}}{1 - (1-T_{TE})^2 T_{TE} e^{-2\alpha x} e^{-2i\delta}} \quad (88)$$

For intensity:

$$n_0 R' R'^* \cong \frac{e^{-2i\delta} (1-T_{TE})^2 e^{-4\alpha x}}{1 - 2(1-T_{TE})^2 \cos(2\delta) T_{TE} e^{-2\delta x}} \quad (89)$$

$$n_0 R R^* = \begin{cases} < \frac{T_{TE}^2 (1-T_{TE})^2 e^{-4\alpha x}}{1 - 2(1-T_{TE})^2 T_{TE} e^{-2\alpha x}} \quad (\text{max}) \end{cases} \quad (90)$$

$$> \frac{T_{TE}^2 (1-T_{TE})^2 e^{-4\alpha x}}{1 + 2(1-T_{TE})^2 T_{TE} e^{-2\alpha x}} \quad (\text{min}) \quad (91)$$

$$n_0 R R^* = \begin{cases} < 1.01 T_{TE2}^2 \\ > 0.99 T_{TE}^2 \end{cases} \cong T_{TE}^2 \quad (92)$$

for the constructive and destructive interference cases. The amplitude coefficient is

$$(R'R'^*)^{1/2} = T_{TE} \quad (93)$$

The energy trapped inside the ZnSe plate once it has leaked in is thus

$$\begin{aligned} \text{Trapped Energy} &= 1 - (n_0 T'T'^*) - (n_0 R'R'^*) \\ &= 0.99998 \end{aligned} \quad (94)$$

The coupling coefficient, κ , from one waveguide to an adjacent waveguide is then equation 65 multiplied by equation 86 where T_{TE} is given by equation 80:

$$\kappa_{TE} \cong \frac{\lambda_0^3}{2 \sqrt{8} (n^2 - 1) t^4} \quad (95)$$

$$\begin{aligned} &= 4.69 \times 10^{-5} \text{ m}^{-1} \quad (t=1 \text{ mm}) \\ &= 2.92 \times 10^{-6} \text{ m}^{-1} \quad (t=2 \text{ mm}) \end{aligned} \quad (96)$$

Almost all of this coupled energy is retained in the adjacent waveguide because of the $(\pi/2 - \lambda_0/\sqrt{8}t)$ angle of refraction (almost along the z axis).

3.4 Coupling Coefficient for TM Polarization

For TM polarization the Fresnel equation becomes ($n = 1/2.4$)

$$\frac{E_r}{E_i} = \frac{-n^2 \cos \theta_i + \sqrt{n^2 - \sin^2 \theta_i}}{n^2 \cos \theta_i + \sqrt{n^2 - \sin^2 \theta_i}} \quad (97)$$

thus using equations 72, 79, and 80 (again leaving n as 2.4)

$$T_{TM} \approx 2n^2 \lambda_0 / ((n^2 - 1)^{1/2} \sqrt{8} t) \quad (98)$$

$$= n^2 T_{TE} = \begin{cases} 2.0 \times 10^{-2} & (t = 1 \text{ mm}) \\ 9.8 \times 10^{-3} & (t = 2 \text{ mm}) \end{cases} \quad (99)$$

To calculate the coupling coefficient for the TM polarization we note that from equation 5a the loss coefficient for TM polarization is n^2 as high as for the TE polarization. (This is why the TE polarization dominates. Note also in equations 5 and 5a that $a = t/2$.) From equation 95 the TM coupling coefficient is written

$$k_{TM} = \frac{n^4 \lambda_0^3}{2 \sqrt{8} (n^2 - 1) t^4} \quad (100)$$

$$\begin{aligned} &= 1.6 \times 10^{-3} \text{ m}^{-1} \quad (t = 1 \text{ mm}) \\ &= 9.7 \times 10^{-5} \text{ m}^{-1} \quad (t = 2 \text{ mm}) \end{aligned} \quad (101)$$

Since the TE mode dominates in waveguide which is walled on opposite sides with ZnSe, the coupling coefficient of equation 95 shows us that very little radiation reaches an adjacent waveguide. Indeed,

99.998% of the leaked radiation is trapped inside the ZnSe walls as shown by equation 95 if these walls are of perfect optical quality. Consequently, the likelihood of phase locking adjacent channels is very small. It is believed that the poor optical quality of the ZnSe windows of the 1x2 device shown in Figure 1 caused scattering off the clearly visible crystalline boundaries (grains) to send radiation into the adjacent waveguide. This small amount was enough to phase-lock the two waveguides. Antireflection coating or beveling the ends of the plates may be a better method of increasing the coupling. This will be discussed further in Section 7.0, Conclusions and Recommendations.

4.0 CALCULATION OF ARRAY-MODE (SUPERMODE) RELATIVE OSCILLATOR STRENGTHS

When phase-locked arrays of semiconductor lasers were experimentally tested, it was found¹³⁻¹⁴ that the far-field patterns did not agree with a multiple slit interference pattern analysis. The explanation for the observed far-field patterns and a narrow spectral width led to the development of "super" mode or "array" mode theory. In this theory the eigenmodes or "natural modes" of the whole laser array are calculated.

In the coupled-mode analysis of linear phase locked laser arrays recently developed by Butler²¹ and by Kapon²², the electric field of each isolated channel is

$$E_{\ell}(x,y,z) = \tilde{E}_{\ell}(x,y) \exp(i\tilde{k}_{z\ell}z) \quad \ell = 1, 2, \dots, N \quad (102)$$

where $\tilde{k}_{z\ell}$ is the complex propagation constant in the ℓ^{th} channel. The total electric field of the array is thus

$$E_y(x,y,z) = \sum_{\ell=1}^N \tilde{E}_{\ell}(x,y) A_{\ell}(z) \exp(i\tilde{k}_{z\ell}z) \quad (103)$$

where $A_{\ell}(z)$ is due to the interaction among waveguides. The electric field is given in the y polarization as shown in Figure 4 because the TE polarization has the lower waveguide propagation loss and was found to be the preferred lasing polarization in the previous 2×1 array device. (Semiconductor laser arrays are of "slab" geometry and generally operate in modes polarized in the x direction of Figure 4.)

The coupling between adjacent waveguides (nearest neighbor approximation) is expressed by the "coupled-mode" equation²³

$$\frac{dE_l}{dz} = i\tilde{k}_{z\ell} E_\ell + i\kappa_{\ell,\ell+1} E_{\ell+1} + i\kappa_{\ell,\ell-1} E_{\ell-1} \quad (104)$$

Here, the transverse dependence, (x,y) , has been integrated out, and the coupling coefficient, κ_{ij} , is a function of the transverse E-field overlap. Substituting equation 103 for the total E-field into equation 104 and assuming symmetric coupling $\kappa_{ij} = \kappa$ and $\tilde{k}_{z\ell} = \tilde{k}_z$ for single mode operation, we have

$$\frac{d}{dz} \begin{bmatrix} A_1 \\ A_2 \\ \vdots \\ \vdots \\ A_N \end{bmatrix} = i \begin{bmatrix} \tilde{k}_z & \kappa & 0 & \dots & 0 \\ \kappa & \tilde{k}_z & \kappa & \dots & 0 \\ \vdots & \vdots & \vdots & \ddots & \vdots \\ \vdots & \vdots & \vdots & \vdots & \kappa & \tilde{k}_z & \kappa \\ 0 & \dots & \dots & 0 & \kappa & \tilde{k}_z \end{bmatrix} \begin{bmatrix} A_1 \\ A_2 \\ \vdots \\ \vdots \\ A_N \end{bmatrix} \quad (105)$$

$$A_i \equiv E_i(z) \exp(i\tilde{k}_z z) \quad (106)$$

Note the asymmetry of the first and last equations due to the waveguide array geometry. Equation 105 may be written

$$\frac{d\tilde{E}}{dz} = i \tilde{A} \tilde{E} \quad (107)$$

where \tilde{A} is a complex tridiagonal matrix.

Butler²¹ and Kapon²² next solved for the eigenvectors and eigenvalues of the \tilde{A} matrix:

$$(\tilde{A} - \tilde{k}_z^\nu I) \tilde{E}^\nu = 0 \quad (108)$$

where ν represents the eigenmode or "array-mode" mode number, and

$$\tilde{k}_z^\nu = \tilde{k}_z + 2\kappa \cos\left(\frac{\pi\nu}{N+1}\right) \quad (109)$$

and the eigenvectors have the components

$$(\vec{E}^v)_\ell = \sin \left(\ell \frac{\pi v}{N+1} \right) \quad \ell = 1, 2, \dots, N \quad (110)$$

where $v = 1, 2, \dots, N$ (array-mode number) for a $1 \times N$ linear array.

The E-field distributions for 1×2 through 1×7 arrays are listed in Table I along with each array-mode propagation constant. The components of each array-mode are the relative E-field strengths of the individual waveguides. It is noted that the $v=1$ or fundamental array-mode has the highest oscillator frequency, and the highest order mode, $v=N$, has the lowest operating frequency. For a symmetric array of lasers, the individual oscillators would either be in phase or 180° out of phase with its nearest neighbor. Consequently, only lowest order or highest order array-modes would operate. Plots of these array-modes will be presented in Section 5.

It should be noted that the coupled-mode equation (105) is a simple model. Recently Hadley²⁴ has included gain medium saturation effects into the analysis. Liang and Chu²⁵ have included spatial hole burning, and Hardy and Streifer²⁶ have rederived the theory. All published analyses concern semiconductor laser arrays.

4.1 Two-Dimensional Array-Mode Oscillator Strengths

We next extend the linear array coupled-mode theory to two dimensions. For a two-dimensional array the individual oscillator amplitudes may be written A_{ij} where i is the column number and j is the row number of the oscillator. By forming a "long" vector from the A_{ij} 's, the coupled-mode equation (105) can be written for a 3×3 array for example as:

TABLE I. ARRAY-MODES FOR 1 x 2 THROUGH 1 x 7 ARRAYS
 $(\beta = k_z) \quad (k = \kappa)$

N=2

$$\vec{E}^1 = (0.866, 0.866)$$

$$\beta^1 = \beta + \kappa$$

$$\vec{E}^2 = (0.866, -0.866)$$

$$\beta^2 = \beta - \kappa$$

N=3

$$\vec{E}^1 = (0.707, 1, 0.707)$$

$$\beta^1 = \beta + 1.414 \kappa$$

$$\vec{E}^2 = (1, 0, -1)$$

$$\beta^2 = \beta$$

$$\vec{E}^3 = (0.707, -1, 0.707)$$

$$\beta^3 = \beta - 1.414 \kappa$$

N=4

$$\vec{E}^1 = (0.588, 0.951, 0.951, 0.588)$$

$$\beta^1 = \beta + 1.618 \kappa$$

$$\vec{E}^2 = (0.951, 0.588, -0.588, -0.951)$$

$$\beta^2 = \beta + 0.618 \kappa$$

$$\vec{E}^3 = (0.951, -0.588, -0.588, 0.951)$$

$$\beta^3 = \beta - 0.618 \kappa$$

$$\vec{E}^4 = (0.588, -0.951, 0.951, -0.588)$$

$$\beta^4 = \beta - 1.618 \kappa$$

N=5

$$\vec{E}^1 = (0.5, 0.866, 1, 0.866, 0.5)$$

$$\beta^1 = \beta + 1.732 \kappa$$

$$\vec{E}^2 = (0.866, 0.866, 0, -0.866, -0.866)$$

$$\beta^2 = \beta + \kappa$$

$$\vec{E}^3 = (1, 0, -1, 0, 1)$$

$$\beta^3 = \beta$$

$$\vec{E}^4 = (0.866, -0.866, 0, 0.866, -0.866)$$

$$\beta^4 = \beta - \kappa$$

$$\vec{E}^5 = (0.5, -0.866, 1, -0.866, 0.5)$$

$$\beta^5 = \beta - 1.732 \kappa$$

TABLE I (CONTINUED)

N=6

$\vec{E}^1 = (0.434, 0.782, 0.975, 0.975, 0.782, 0.434)$	$\beta^1 = \beta + 1.802 \kappa$
$\vec{E}^2 = (0.782, 0.975, 0.434, -0.434, -0.975, -0.782)$	$\beta^2 = \beta + 1.247 \kappa$
$\vec{E}^3 = (0.975, 0.434, -0.782, -0.782, 0.434, 0.975)$	$\beta^3 = \beta + 0.445 \kappa$
$\vec{E}^4 = (0.975, -0.434, -0.782, 0.782, 0.434, -0.975)$	$\beta^4 = \beta - 0.445 \kappa$
$\vec{E}^5 = (0.782, -0.975, 0.434, 0.434, -0.975, 0.782)$	$\beta^5 = \beta - 0.1247 \kappa$
$\vec{E}^6 = (0.434, -0.782, 0.975, -0.975, 0.782, -0.434)$	$\beta^6 = \beta - 1.802 \kappa$

N=7

$\vec{E}^1 = (0.383, 0.707, 0.924, 1, 0.924, 0.707, 0.383)$	$\beta^1 = \beta + 1.848 \kappa$
$\vec{E}^2 = (0.707, 1, 0.707, 0, -0.707, -1, -0.707)$	$\beta^2 = \beta + 1.414 \kappa$
$\vec{E}^3 = (0.924, 0.707, -0.383, -1, -0.383, 0.707, 0.924)$	$\beta^3 = \beta + 0.765 \kappa$
$\vec{E}^4 = (1, 0, -1, 0, 1, 0, -1)$	$\beta^4 = \beta$
$\vec{E}^5 = (0.924, -0.707, -0.383, 1, -0.383, -0.707, 0.924)$	$\beta^5 = \beta - 0.765 \kappa$
$\vec{E}^6 = (0.707, -1, 0.707, 0, -0.707, 1, -0.707)$	$\beta^6 = \beta - 1.414 \kappa$
$\vec{E}^7 = (0.383, -0.707, 0.924, -1, 0.924, -0.707, 0.383)$	$\beta^7 = \beta - 1.848 \kappa$

$$\frac{d}{dt} \begin{bmatrix} A_{11} \\ 12 \\ 13 \\ \vdots \\ 21 \\ 22 \\ 23 \\ \vdots \\ 31 \\ 32 \\ 33 \end{bmatrix} = i \begin{bmatrix} \beta \kappa 0 & \kappa 0 0 & 0 0 0 \\ \kappa \beta \kappa & 0 \kappa 0 & 0 0 0 \\ 0 \kappa \beta & 0 0 \kappa & 0 0 0 \\ \vdots & \vdots & \vdots \\ \kappa 0 0 & \beta \kappa 0 & \kappa 0 0 \\ 0 \kappa 0 & \kappa \beta \kappa & 0 \kappa 0 \\ 0 0 \kappa & 0 \kappa \beta & 0 0 \kappa \\ \vdots & \vdots & \vdots \\ 0 0 0 & \kappa 0 0 & \beta \kappa 0 \\ 0 0 0 & 0 \kappa 0 & \kappa \beta \kappa \\ 0 0 0 & 0 0 \kappa & 0 \kappa \beta \end{bmatrix} \begin{bmatrix} A_{11} \\ 12 \\ 13 \\ \vdots \\ 21 \\ 22 \\ 23 \\ \vdots \\ 31 \\ 32 \\ 33 \end{bmatrix} \quad (111)$$

where $\beta \equiv k_z$. The \tilde{A} matrix now becomes (mxn) by (mxn) in size.

To find the eigenvectors and eigenvalues of the \tilde{A} matrix,

$$(\tilde{A} - \beta^v I) \tilde{E}^v = 0 \quad (112)$$


may be divided by κ and a new variable

$$-\beta' = \frac{\beta - \beta^v}{\kappa} \quad (113)$$

defined for the diagonal elements. The rest of the matrix is then 1's or 0's. Scientific subroutine programs can solve for the eigenvalues and eigenvectors of this matrix of 0's and 1's. The computed eigenvalues are then converted to the \tilde{A} matrix eigenvalues by equation 113. Some array-modes in rectangular coordinates are given in Table II where symmetric nearest neighbor coupling of identical waveguide lasers has again been assumed.

Arrays having cylindrical symmetry may also be written in a coupled mode formalism and solved for their array-modes.

TABLE 11.
ARRAY-MODES: RECTANGULAR COORDINATES
(RELATIVE OSCILLATOR AMPLITUDES)

2×2 

$$B^1 = B + 2 \times$$

.5	.5
.5	.5

$$B^2 = B$$

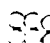
-.5	-.5
.5	.5

$$B^3 = B$$

-.5	.5
-.5	.5

$$B^4 = B - 2 \times$$

-.5	.5
.5	-.5

2×3 

$$B^1 = B + 2.414 \times$$

.35	.5	.35
.35	.5	.35

$$B^2 = B + \times$$

.5	0	-.5
.5	0	-.5

$$B^3 = B + .414 \times$$

.35	.5	.35
-.35	-.5	-.35

$$B^4 = B - .414 \times$$

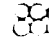
-.35	.5	-.35
-.35	.5	-.35

$$B^5 = B - \times$$

.5	0	-.5
-.5	0	.5

$$B^6 = B - 2.414 \times$$

.35	.5	.35
-.35	-.5	-.35

2×4 

$$B^1 = B + 2.618 \times$$

.26	.43	.43	.26
.26	.43	.43	.26

$$B^2 = B + 1.618 \times$$

.43	.26	-.26	-.43
.43	.26	-.26	-.43

$$B^3 = B + .618 \times$$

.26	.43	.43	.26
-.26	-.43	-.43	-.26

$$B^4 = B + .382 \times$$

.43	-.26	-.26	.43
.43	-.26	-.26	.43

$$B^5 = B - .382 \times$$

.43	.26	-.26	-.43
-.43	-.26	.26	.43

$$B^6 = B - .618 \times$$

.26	-.43	.43	-.26
.26	-.43	.43	-.26

$$B^7 = B - 1.618 \times$$

.43	-.26	-.26	.43
-.43	.26	.26	-.43

$$B^8 = B - 2.618 \times$$

-.26	.43	-.43	.26
.26	-.43	.43	-.26

2×5 

$$B^1 = B + 2.732 \times$$

.20	.35	.41	.35	.20
.20	.35	.41	.35	.20

$$B^2 = B + 2 \times$$

.35	.35	0	-.35	-.35
.35	.35	0	-.35	-.35

$$B^3 = B + \times$$

.41	0	-.41	0	.41
.41	0	-.41	0	.41

$$B^4 = B + .732 \times$$

.20	.35	.41	.35	.20
-.20	-.35	-.41	-.35	-.20

$$B^5 = B$$

-.35	.35	0	-.35	.35
-.35	.35	0	-.35	.35

$$B^6 = B$$

.35	.35	0	-.35	-.35
-.35	-.35	0	.35	.35

$$B^7 = B - .732 \times$$

-.20	.35	-.41	.35	-.20
-.20	.35	-.41	.35	-.20

$$B^8 = B - \times$$

.41	0	-.41	0	.41
-.41	0	.41	0	-.41

$$B^9 = B - 2 \times$$

.35	-.35	0	.35	-.35
-.35	.35	0	-.35	.35

$$B^{10} = B - 2.732 \times$$

.20	-.35	.41	-.35	.20
-.20	.35	-.41	.35	-.20

TABLE II. (CONTINUED)

3 x 3



$$\beta^1 = \beta + 2.828 \kappa$$

.25	.35	.25
.35	.5	.35
.25	.35	.25

$$\beta^2 = \beta + 1.414 \kappa$$

	.35	.5
-.35	0	.35
-.5	-.35	0

$$\beta^3 = \beta + 1.414 \kappa$$

-.5	-.35	0
-.35	0	.35
0	.35	.5

$$\beta^4 = \beta$$

-.34	-.42	.11
.42	.23	.42
.11	-.42	-.34

$$\beta^5 = \beta$$

0	0	.58
0	-.58	0
.58	0	0

$$\beta^6 = \beta$$

.49	-.30	-.07
-.40	0	.40
.07	.30	-.49

$$\beta^7 = \beta - 1.414 \kappa$$

.49	-.30	-.07
-.40	0	.40
.07	.30	-.49

$$\beta^8 = \beta - 1.414 \kappa$$

-.49	.40	-.40
-.30	0	.30
.49	-.40	.07

$$\beta^9 = \beta - 2.828 \kappa$$

.25	-.35	.25
-.34	.5	-.35
.25	-.35	.25

1, 3, 1



$$\beta^1 = \beta + 2 \kappa$$

	.35	
.35	.71	.35
	.35	

$$\beta^2 = \beta$$

	.79	
-.21	0	-.58
	0	

$$\beta^3 = \beta$$

	-.21	
.79	0	-.58
	0	

$$\beta^4 = \beta$$

	.29	
.29	0	.29
	-.87	

$$\beta^5 = \beta - 2 \kappa$$

	.35	
.35	-.71	.35
	.35	

3, 2, 3



$$\beta^1 = \beta + 2 \kappa$$

.35	.35	.35
.35		.35
.35	.35	.35

$$\beta^2 = \beta + 1.414 \kappa$$

-.06	-.39	-.50
.31		-.31
.50	.39	.06

$$\beta^3 = \beta + 1.414 \kappa$$

.50	.31	-.06
.39		-.39
.06	-.31	-.50

$$\beta^4 = \beta$$

.45	.21	-.45
-.21		-.21
-.45	.21	.45

$$\beta^5 = \beta$$

.21	-.45	-.21
.45		.45
-.21	-.45	.21

$$\beta^6 = \beta - 1.414 \kappa$$

.12	-.43	.49
.26		-.26
-.49	.43	-.12

$$\beta^7 = \beta - 1.414 \kappa$$

-.49	.26	.12
.43		-.43
-.12	-.26	.49

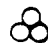
$$\beta^8 = \beta - 2 \kappa$$

-.35	.35	-.35
.35		.35
-.35	.35	-.35

Note that in cylindrically symmetric arrays each waveguide may have as many as six nearest neighbors instead of four or less for rectangular arrays. A few cylindrical array-modes are shown in Table III.

In addition care must be taken in controlling the polarizations of the individual oscillators. If the polarizations are all radial or aximuthal, for example, there will be a null in the center of the far-field pattern, resulting in a doughnut-shape irradiance.

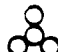
TABLE III.
ARRAY-MODES: CYLINDRICAL COORDINATES (HONEYCOOMB STRUCTURE)
(RELATIVE OSCILLATOR AMPLITUDES)

1, 2 

$$\begin{array}{r} \beta^1 = \beta + 2 \kappa \\ \hline .58 \\ .58 \quad .58 \end{array}$$

$$\begin{array}{r} \beta^2 = \beta - \kappa \\ \hline .41 \\ -.41 \quad 0 \end{array}$$

$$\begin{array}{r} \beta^3 = \beta - \kappa \\ \hline .71 \\ -.71 \quad 0 \end{array}$$


1, 1, 2 

$$\begin{array}{r} \beta^1 = \beta + 1.732 \kappa \\ \hline .41 \\ .71 \\ .41 \quad .41 \end{array}$$

$$\begin{array}{r} \beta^2 = \beta \\ \hline .71 \\ 0 \\ -.71 \quad 0 \end{array}$$

$$\begin{array}{r} \beta^3 = \beta \\ \hline .41 \\ 0 \\ .41 \quad -.82 \end{array}$$

$$\begin{array}{r} \beta^4 = \beta - 1.732 \kappa \\ \hline .41 \\ -.71 \\ .41 \quad .41 \end{array}$$

2, 3 


$$\begin{array}{r} \beta^1 = \beta + 2.935 \kappa \\ \hline .47 \quad .47 \\ .35 \quad .56 \quad .35 \end{array}$$

$$\begin{array}{r} \beta^2 = \beta + .618 \kappa \\ \hline -.37 \quad .37 \\ -.60 \quad 0 \quad .60 \end{array}$$

$$\begin{array}{r} \beta^3 = \beta - .463 \kappa \\ \hline -.51 \quad -.51 \\ .44 \quad .31 \quad .44 \end{array}$$

$$\begin{array}{r} \beta^4 = \beta - 1.473 \kappa \\ \hline -.14 \quad -.14 \\ -.43 \quad .77 \quad -.43 \end{array}$$

$$\begin{array}{r} \beta^5 = \beta - 1.618 \kappa \\ \hline -.60 \quad .60 \\ .37 \quad 0 \quad -.37 \end{array}$$


1, 2, 1 

$$\begin{array}{r} \beta^1 = \beta + 2.562 \kappa \\ \hline .56 \\ .44 \quad .44 \\ .56 \end{array}$$

$$\begin{array}{r} \beta^2 = \beta \\ \hline 0 \\ .71 \quad -.71 \\ 0 \end{array}$$

$$\begin{array}{r} \beta^3 = \beta - \kappa \\ \hline .71 \\ 0 \quad 0 \\ -.71 \end{array}$$

$$\begin{array}{r} \beta^4 = \beta - 1.562 \kappa \\ \hline .44 \\ -.56 \quad -.56 \\ .44 \end{array}$$

1, 2, 3 

$$\begin{array}{r} \beta^1 = \beta + 3.236 \kappa \\ \hline .30 \\ .49 \quad .49 \\ .30 \quad .49 \quad .30 \end{array}$$

$$\begin{array}{r} \beta^2 = \beta + .618 \kappa \\ \hline -.53 \\ .07 \quad -.40 \\ .65 \quad .33 \quad -.12 \end{array}$$

$$\begin{array}{r} \beta^3 = \beta + .618 \kappa \\ \hline .45 \\ .42 \quad -.15 \\ .24 \quad -.28 \quad -.68 \end{array}$$

$$\begin{array}{r} \beta^4 = \beta - 1.236 \kappa \\ \hline -.49 \\ .30 \quad .30 \\ -.49 \quad .30 \quad -.49 \end{array}$$

$$\begin{array}{r} \beta^5 = \beta - 1.618 \kappa \\ \hline .43 \\ -.37 \quad -.32 \\ -.20 \quad .69 \quad -.23 \end{array}$$

$$\begin{array}{r} \beta^6 = \beta - 1.618 \kappa \\ \hline .017 \\ .59 \quad -.61 \\ -.38 \quad .028 \quad .36 \end{array}$$

TABLE III. (CONTINUED)

3, 3



$$\beta^1 = \beta + 3.182 \kappa$$

.41	.50	.29
.29	.50	.29

$$\beta^2 = \beta + 1.247 \kappa$$

-.42	.23	.52
-.52	-.23	.42

$$\beta^3 = \beta + .445 \kappa$$

-.52	-.42	-.23
.23	.42	.52

$$\beta^4 = \beta - .593 \kappa$$

.09	.29	-.64
-.64	.29	.09

$$\beta^5 = \beta - 1.588 \kappa$$

.57	-.40	-.11
-.11	-.40	.57

$$\beta^6 = \beta - 1.802 \kappa$$

-.23	.52	-.42
.42	-.52	.23

2, 1, 2



$$\beta^1 = \beta + 2.562 \kappa$$

.39	.62	.39
.39	.62	.39

$$\beta^2 = \beta + \kappa$$

.5	0	-.5
.5	0	-.5

$$\beta^3 = \beta - \kappa$$

0	0	-.71
0	0	-.71

$$\beta^4 = \beta - \kappa$$

.71	0	0
-.71	0	0

$$\beta^5 = \beta - 1.562 \kappa$$

-.31	.79	-.31
-.31	.79	-.31

1, 2, 1, 2, 1



$$\beta^1 = \beta + 3.642 \kappa$$

.34	.34	.34
.34	.56	.34
.34	.34	.34

$$\beta^2 = \beta + \kappa$$

.03	.51	.03
-.49	0	.51
-.51	-.03	.49

$$\beta^3 = \beta + \kappa$$

.58	.27	.58
.31	0	.27
-.27	-.31	.58

$$\beta^4 = \beta - \kappa$$

.55	-.12	.55
-.43	0	-.12
-.12	-.43	.55

$$\beta^5 = \beta - \kappa$$

-.18	.57	-.18
-.38	0	.57
.57	-.38	-.18

$$\beta^6 = \beta - 1.646 \kappa$$

-.23	-.23	-.23
-.23	.83	-.23
-.23	-.23	-.23

$$\beta^7 = \beta - 2 \kappa$$

.41	.41	.41
-.41	0	-.41
-.41	-.41	.41

5.0 ARRAY-MODE FAR-FIELD ENERGY DISTRIBUTION STUDIES

The far-field electrical-field distributions of the linear array-modes of Section 4.0 are computed in this section. The purpose of this study was to determine what the exact far-field patterns look like and to see if there is really an $(mxn)^2$ improvement in the peak of the irradiance distribution relative to a single waveguide laser.

The far-field or Fraunhofer region electric field distribution can be calculated using Fourier transform numerical analysis. In the notation of Gaskill²⁷, the irradiance in the far-field for any arbitrary source $u_1(x,y)$ is

$$I_2(x,y) = |u_2(x,y)|^2 \\ = \left(\frac{1}{\lambda z_{12}} \right)^2 \left| U_1 \left(\frac{x}{\lambda z_{12}}, \frac{y}{\lambda z_{12}} \right) \right|^2 \quad (114)$$

where z_{12} is the on axis distance to the far-field location and $U_1(\alpha,\beta)$ is the Fourier transform of the source E-field distribution. The intensity distribution is proportional to the magnitude squared, $U_1(\alpha,\beta) U_1^*(\alpha,\beta)$, of the Fourier transform of the source E-field distribution. The Fourier transforms were computed using a scientific subroutine package employing the Sande-Turkey FFT algorithm. The input array-mode electric-field amplitudes consisted of 1,024 data points of amplitude information. That is, the wavefronts were assumed to be in-phase or 180° out of phase (negative) across the emitting apertures.

Figure 7 shows the calibration of the horizontal and vertical far-field axes using the FFT of a single slit and a single HE_{11} mode. The quantity plotted is $(UU^*)^{1/2}$ which is proportional to $|E|$. This would be squared for intensity. From the far-field pattern of a slit aperture, we know the spacing between the zeros is $\lambda/2a = 5.3$ mm where a is the waveguide half-width of 1 mm for these plots. Likewise the Fourier transform of a waveguide HE_{11} mode, a sine function for rectangular waveguides given by equation 4, can be calculated.

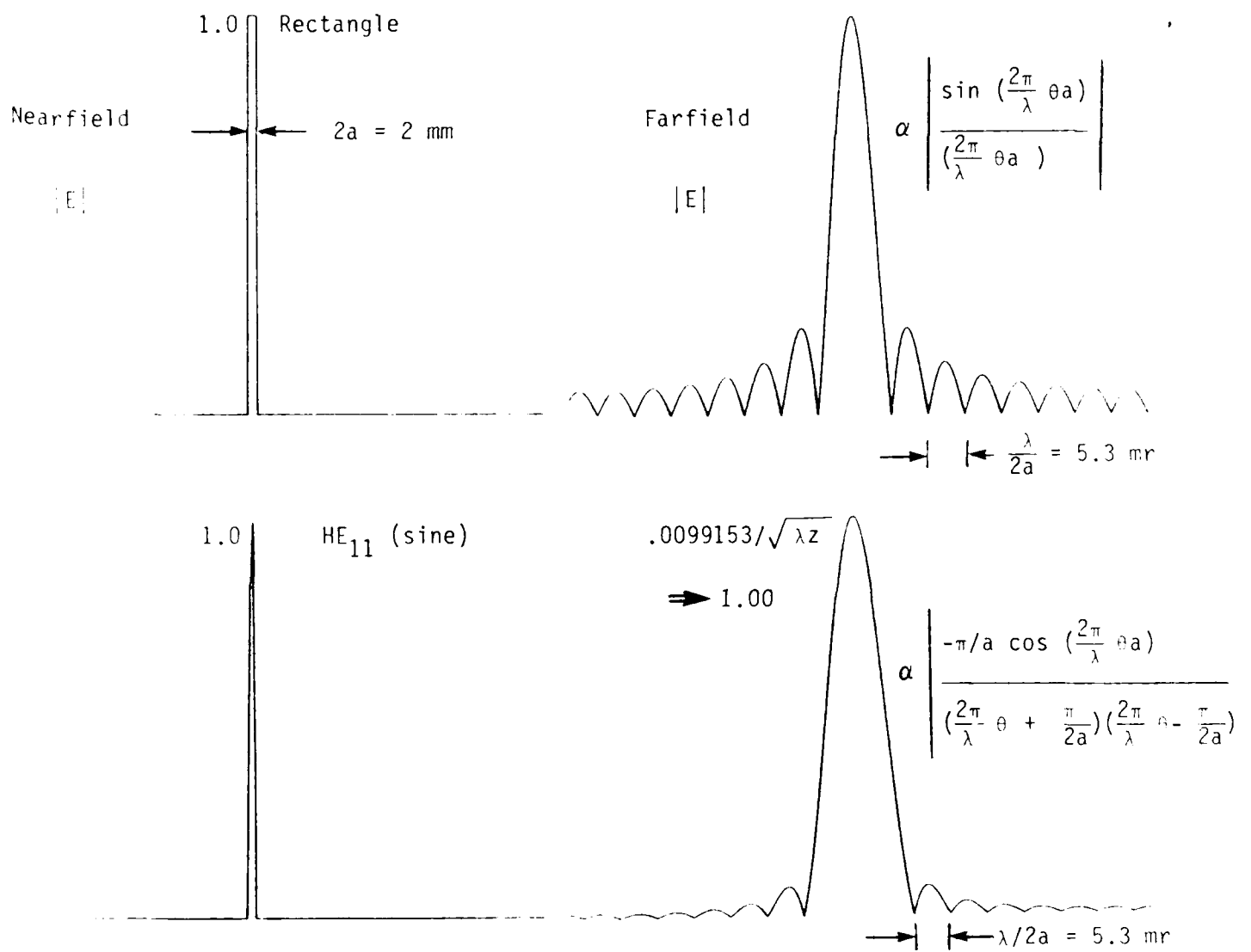


FIGURE 7. HORIZONTAL AXIS CALIBRATION AND MAGNITUDE CALIBRATION OF FFT ANALYSIS

$$\int_{-a}^a \cos(ky) e^{iwy} dy = \frac{(\pi/a) \cos(wa)}{w^2 - (\pi/2a)^2} \quad (115)$$

where $w = \frac{2\pi}{\lambda} \sin \theta \approx \frac{2\pi\theta}{\lambda}$ (116)

The first pole and zero cancel and the zero crossings are 90° out of phase with the slit far-field pattern. The zeros of the HE_{11} far-field pattern are also separated by $\lambda/2a = 5.3$ mrad. We assign the peak of the single HE_{11} far-field pattern a value of 1.00 as indicated. All other FFT's are relative to this number.

Figure 8 is a plot of the far-field of the first ($v=1$) array-modes for 1x2 through 1x7 arrays. The peak of the pattern is normalized with respect to the peak of a single HE_{11} mode as in Figure 7. A 1x7 array thus has a peak E-field magnitude of 6.66 times that of a single waveguide $[(6.66)^2$ in intensity].

Figure 9 shows the far-fields of the higher order array-modes, $v=2$ through $v=7$, for a 1x7 array. The $v=7$ array-mode (π phase shift between adjacent waveguide modes) has the characteristic double lobe pattern seen in semiconductor laser arrays. Surprisingly the peak is 5.56 times that of a single waveguide (vs. 6.66 for $v=1$ mode) due to the wide far-field HE_{11} envelope.

For an $m \times n$ two-dimensional array, the HE_{11} modes of rectangular waveguides are separable in x and y :

$$u_1(x, v) = u_1'(x) u_1''(y) \quad (117)$$

at the array output aperture. Consequently, the far-field pattern is the product of two Fourier transforms, one in the x -axis and one in the y -axis. Thus, the far-field pattern of a 2x7 array would have a peak magnitude of $(2.00 \times 6.66) = 13.32$ times that of a single waveguide

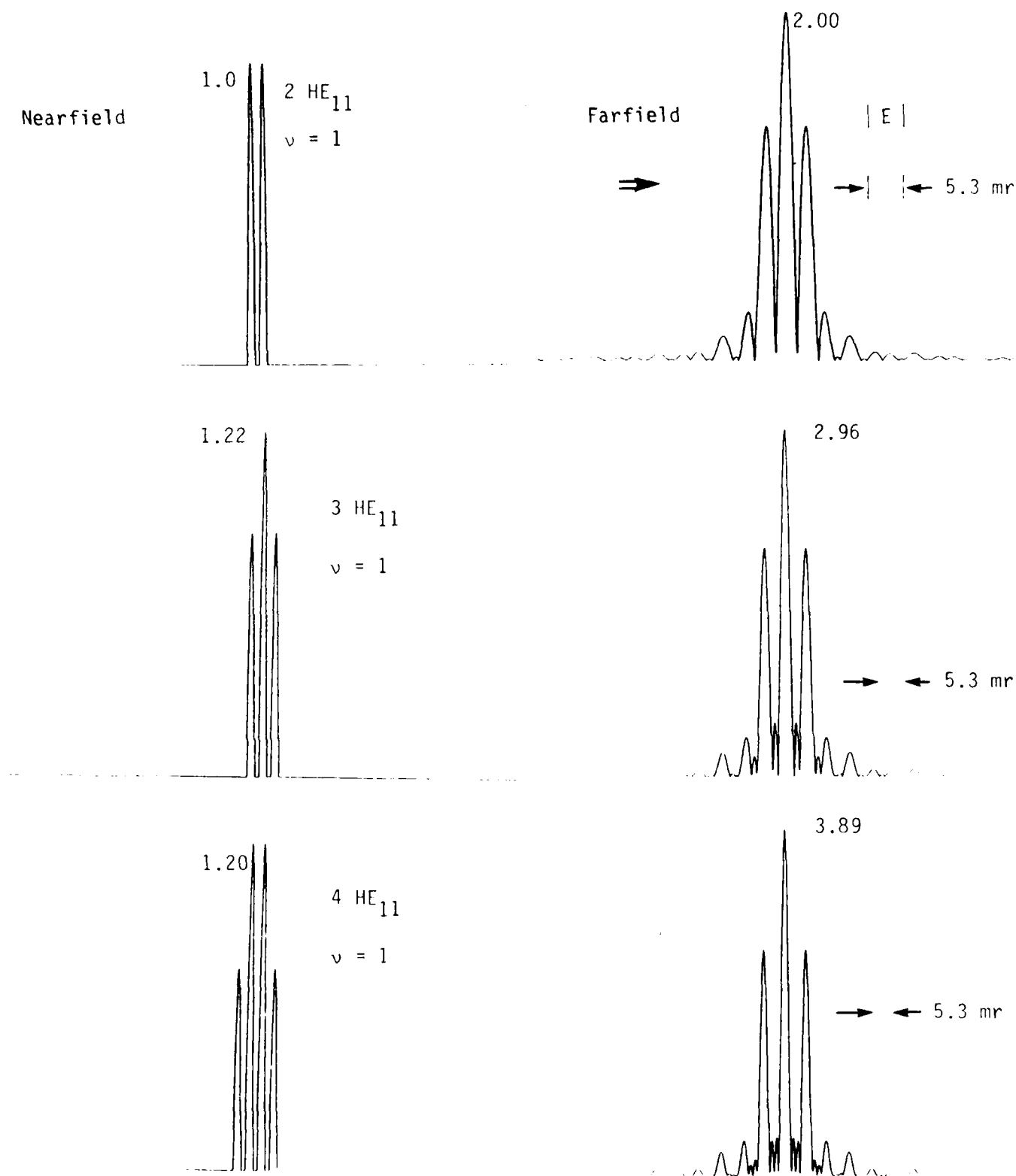


FIGURE 8. FAR-FIELD PATTERNS OF $v = 1$ ARRAY-MODES FOR 1×2 THROUGH 1×7 ARRAYS (ALL ARRAY-MODES NORMALIZED WITH RESPECT TO 1×2 $v = 1$ ARRAY-MODE)

1.29 5 HE₁₁
v = 1



4.82
→ ← 5.3 mr

1.28 6 HE₁₁
v = 1

5.74
→ ← 5.3 mr

1.32 7 HE₁₁
v = 1

6.66
→ ← 5.3 mr

FIGURE 8. CONTINUED

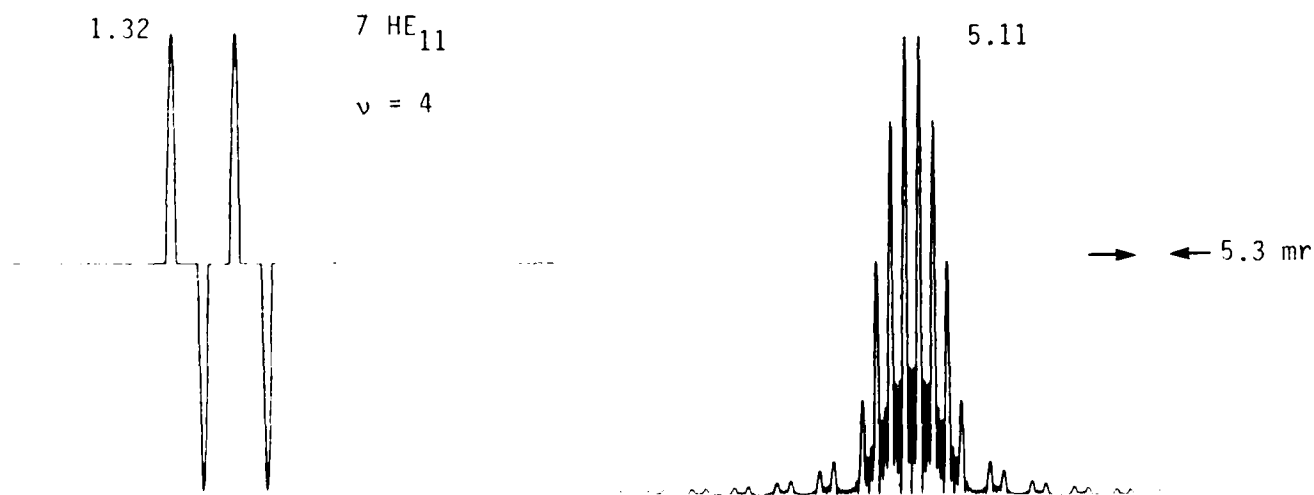
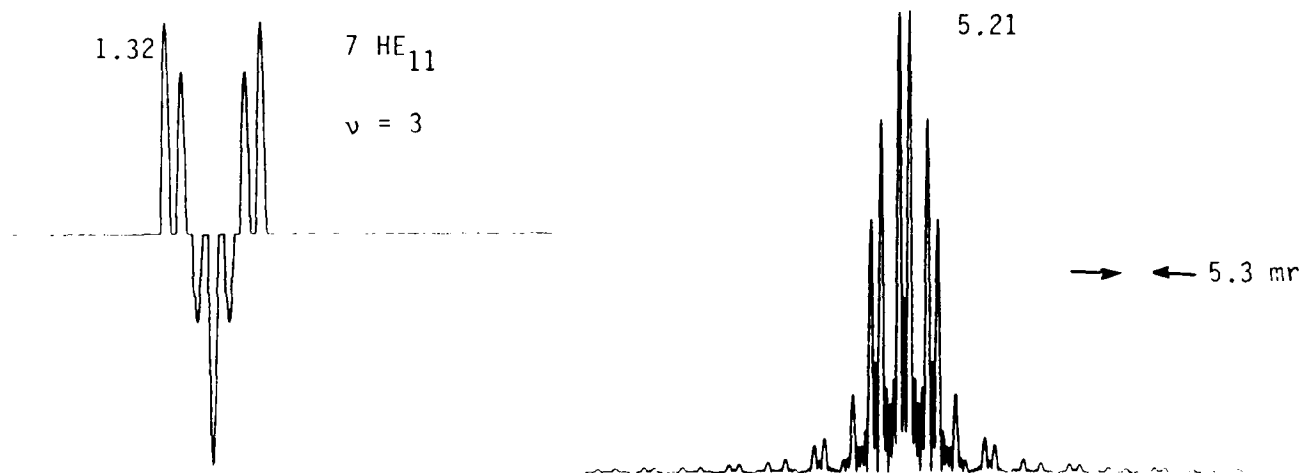
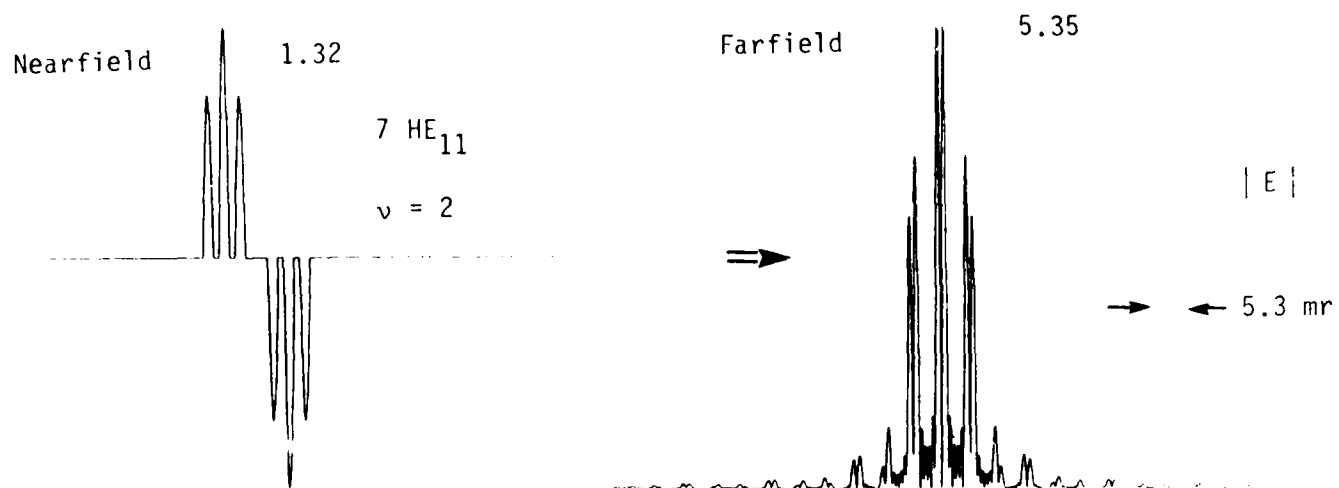


FIGURE 9. FAR-FIELD MAGNITUDE OF HIGHER ORDER ARRAY-MODES
FOR 1 x 7 ARRAY

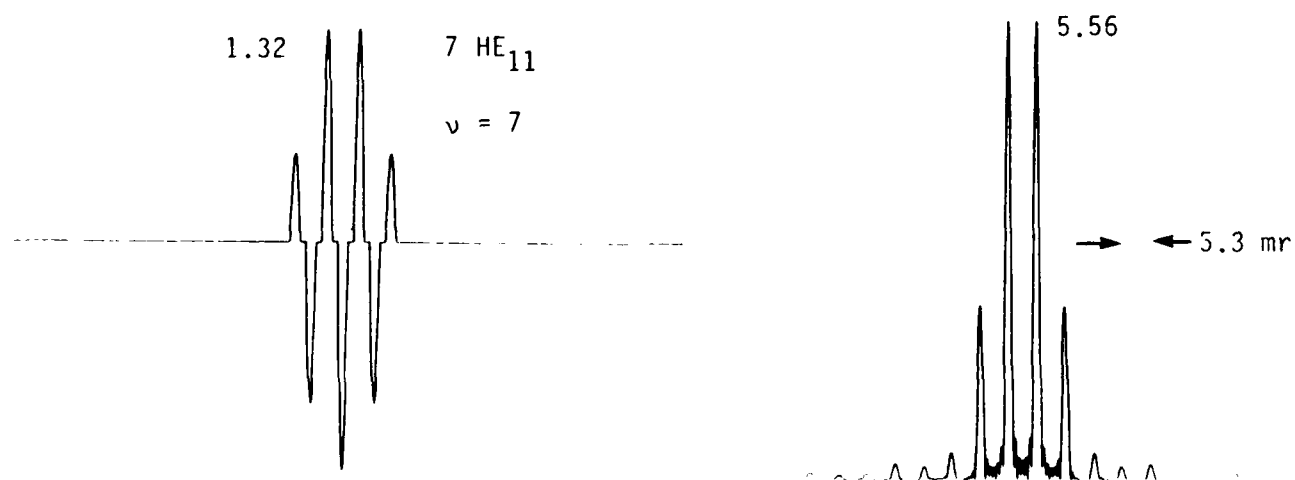
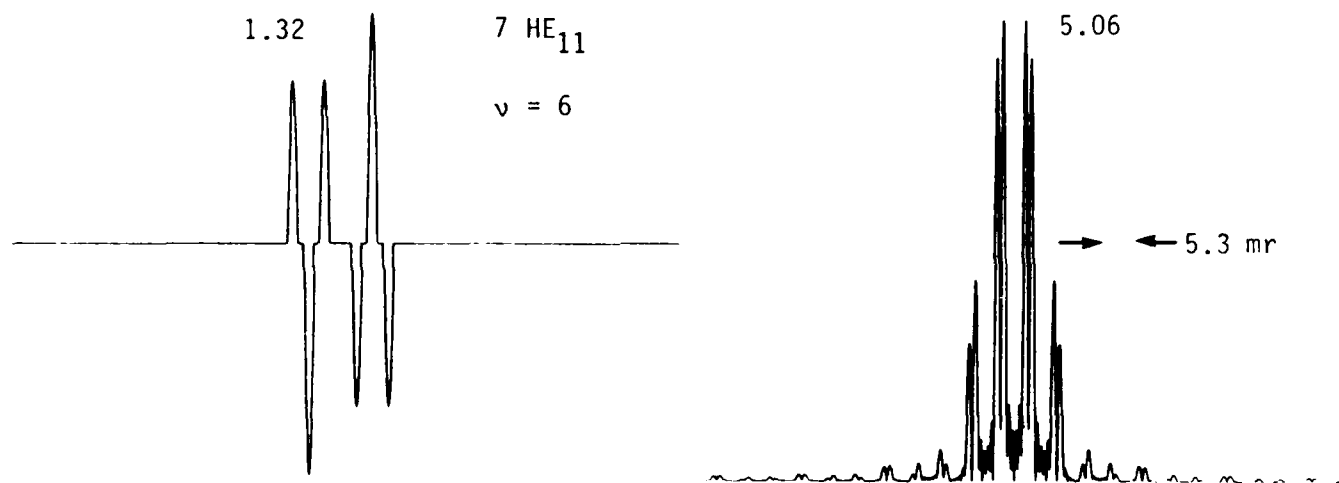
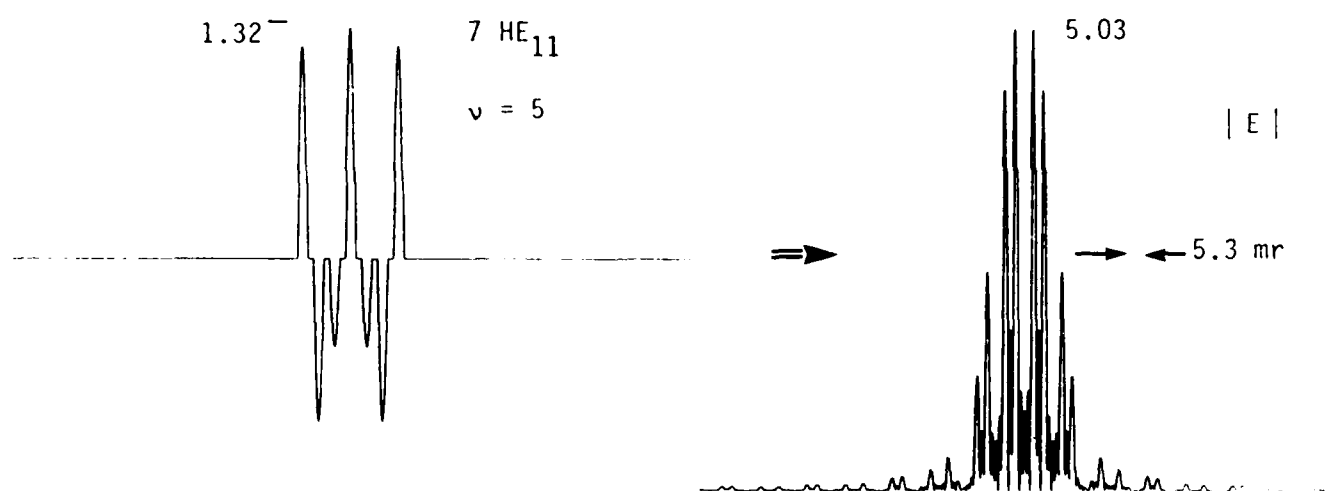


FIGURE 9. CONTINUED

laser or $(2.00 \times 6.66)^2 = 177$ increase in irradiance (W/cm^2). The peak in the far-field radiance is thus slightly less than $(mxn)^2$, 177 vs 196 for example. Similar analysis applies to other size rectangular arrays.

The best-fit Gaussian or TEM_{00} mode to a single waveguide HE_{11} mode was also studied using Fourier analysis. This allows a particularly simple analytical calibration of the far-field watts per square centimeter for the various array-modes. The best fit Gaussian has a beam waist ($1/e^2$ intensity radius) of $0.70a$, where a is the waveguide half-width, as given by equation 6. The plots are scaled for $a = 1$ mm.

The irradiance (W/cm^2) for a single TEM_{00} mode is given by

$$I(r) = \frac{2 P_{tot}}{\pi W^2} \exp(-2r^2/W^2) \quad (118)$$

$$\text{where } W^2(z) = W_0^2 + \left(\frac{\lambda}{\pi W_0}\right)^2 z^2 \quad (1/e^2 \text{ intensity radius}) \quad (119)$$

and z is the distance to the target and P_{tot} is the total power from one waveguide. For large z , equation (110) reduces to

$$I(r) = \frac{2\pi W_0^2}{\lambda^2 z^2} P_{tot} \exp\left(\frac{-2\pi^2 W_0^2}{\lambda^2} \theta_{1/2}^2\right) \quad (120)$$

where $\theta_{1/2} = \tan^{-1}(r/z) \cong r/z$. Thus we have a simple expression for the W/cm^2 of a single TEM_{00} mode for calibration of the FFT numerical analysis of array-modes.

Figure 10 shows the best fit TEM_{00} mode at the square waveguide output aperture. The FFT of this slightly truncated Gaussian is shown on the right side of Figure 10. The percentage of light passing through the $2a \times 2a$ aperture is 99.14%, thus the peak of the FFT is given by equation 120 and is assigned a value of 1.00 in this study. The horizontal axis calibration was obtained from the FFT of a slit aperture and sine aperture in Figure 7.

Figure 11 shows the far-field pattern of the fundamental ($v=1$) supermode for 1×2 through 1×7 arrays normalized to that of a single TEM_{00} waveguide laser. A two by seven array would thus have $(2.00 \times 6.74)^2 = 182$ times the peak irradiance of a single waveguide laser. The W/cm^2 are easily calculated from equation 120. It is seen that the peak irradiance due to TEM_{00} interference is one percent higher than the HE_{11} formed array-mode peak irradiance given in Figure 8. Otherwise the TEM_{00} and HE_{11} supermode patterns are nearly identical.

Two other FFT studies were made in this program. The far-field pattern for a uniform array (no supermodes) of phase-locked waveguide lasers each operating in an HE_{11} mode was analyzed. The results are shown in Figure 12. These results are to be compared with the far-field $v=1$ supermode of a 1×7 array of HE_{11} mode lasers shown in Figure 8. It can be seen that the peak irradiance is 4% higher with a uniform array due to the narrower central lobe.

The last FFT study involved moving the individual waveguides from 1mm apart to 0.5mm apart - - the ZnSe windows would be one-half as thick. The results are shown in Figure 13. The two secondary maxima are moved further from the central maximum and consequently reduced in amplitude. The peak amplitude is the same, however. The ideal supermode would have zero spacing between the waveguides for minimum secondary maxima amplitude.

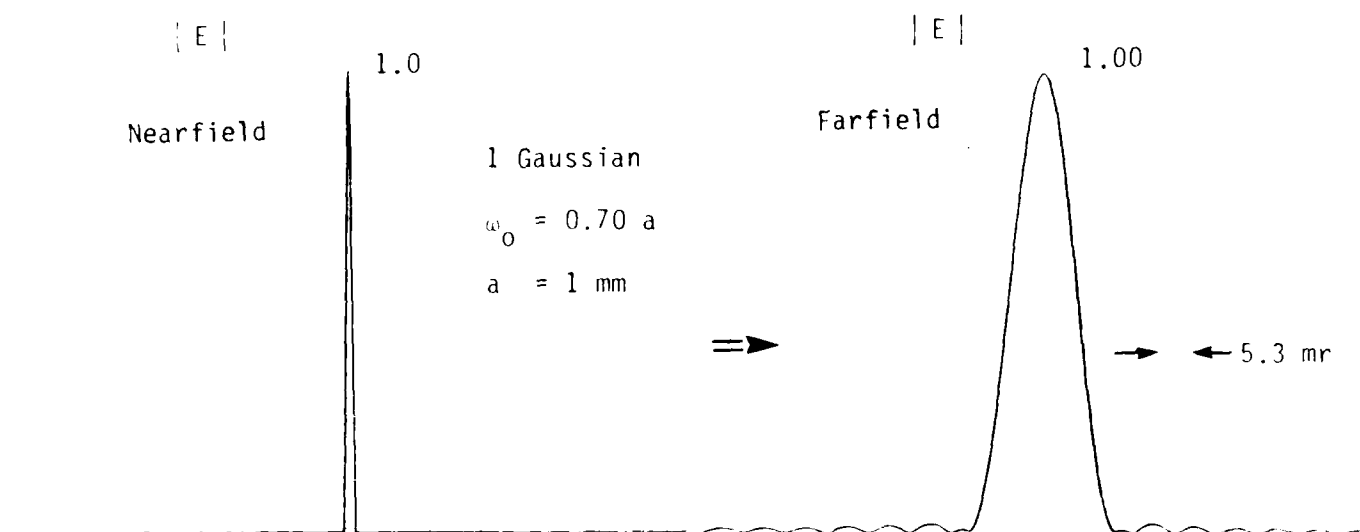


FIGURE 10. FAR FIELD PATTERN OF SLIGHTLY TRUNCATED BEST
FIT TEM_{00} GAUSSIAN MODE

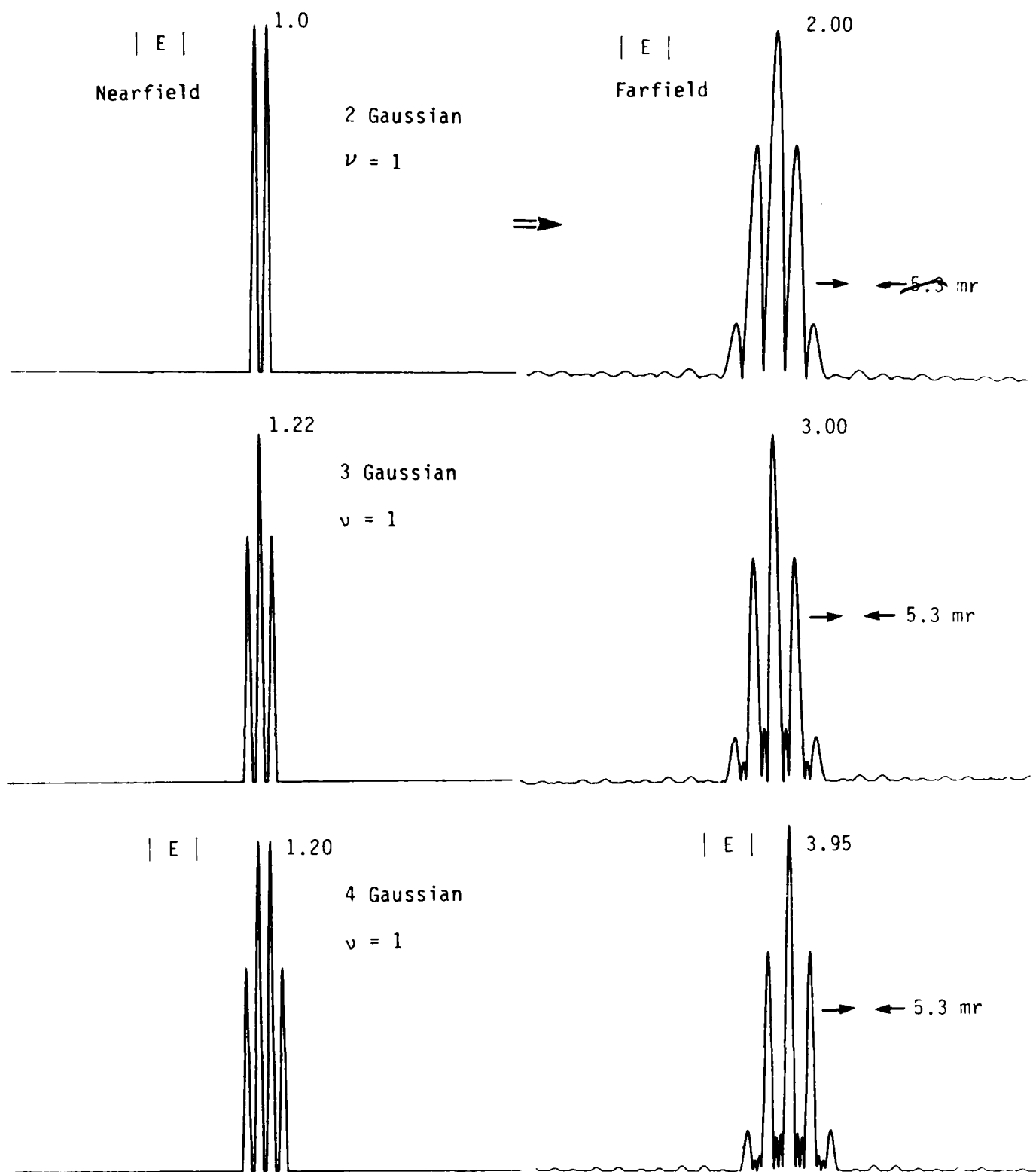


FIGURE 11. FAR-FIELDS OF FUNDAMENTAL ARRAY-MODES OF 1x2 THROUGH 1x7 LINEAR ARRAYS - TEM_{00} INDIVIDUAL MODES

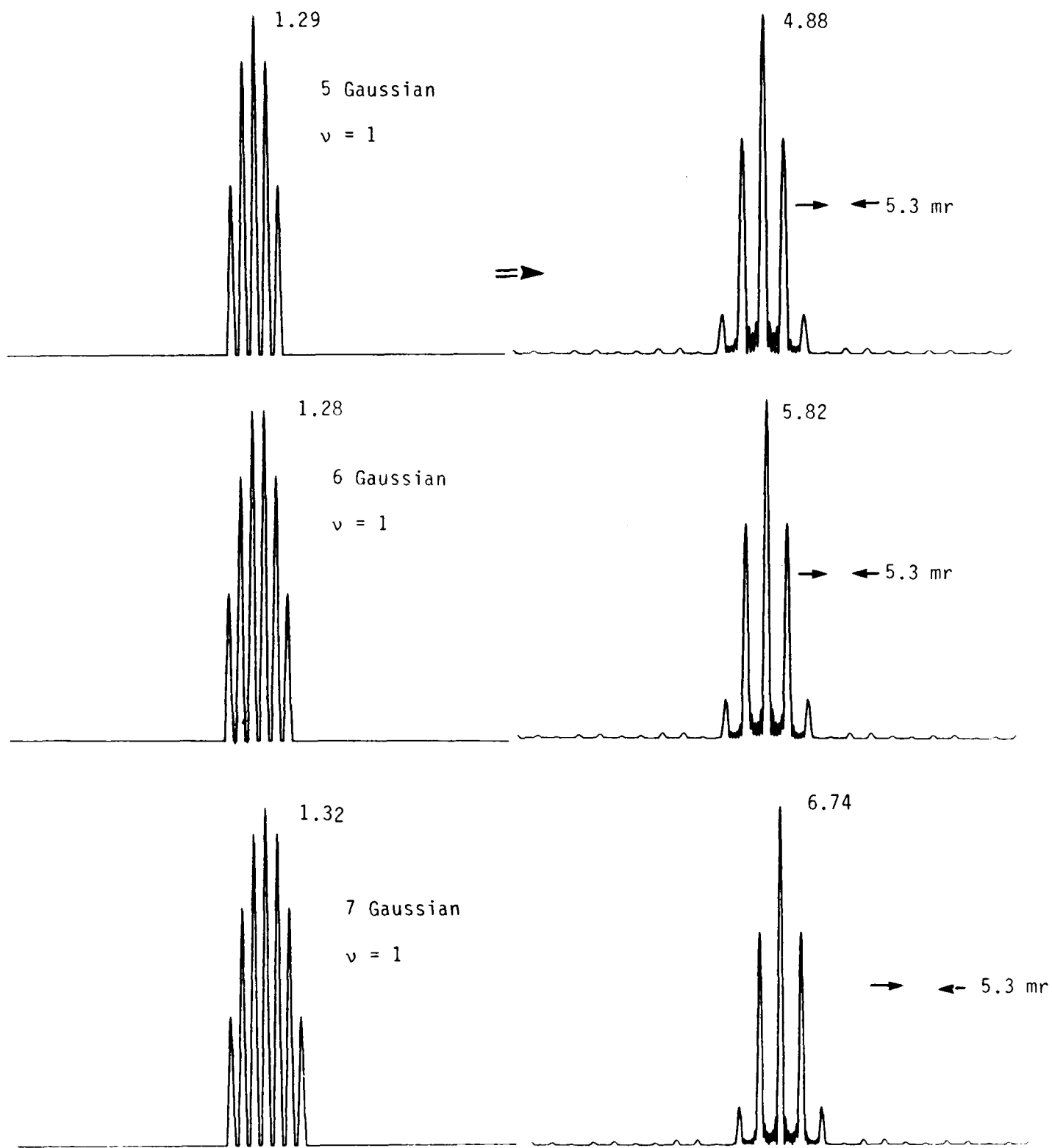


FIGURE 11. CONTINUED

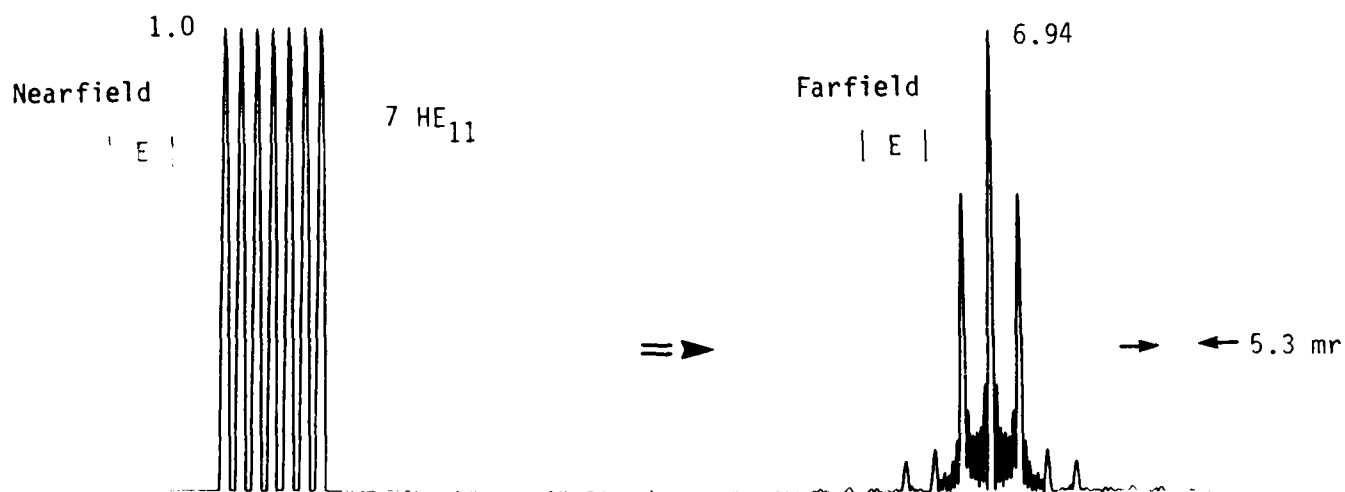


FIGURE 12. FAR-FIELD PATTERN OF UNIFORM (NO ARRAY-MODE) PHASE-LOCKED ARRAY OF SEVEN HE_{11} MODE LASERS

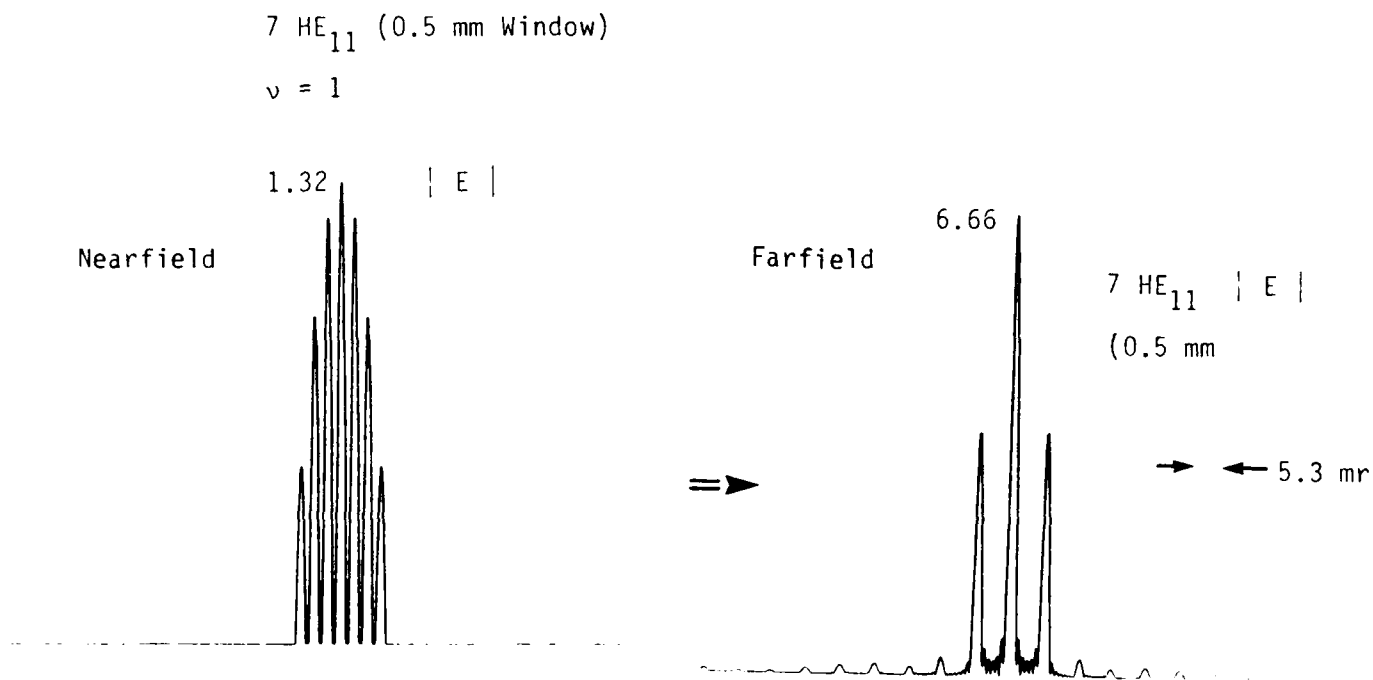


FIGURE 13. FAR-FIELD OF FUNDAMENTAL ARRAY-MODE OF SEVEN HE_{11} WAVEGUIDE LASERS SEPARATED BY 0.5 mm

6.0 EXPERIMENTAL RESULTS

Experimental work began in late July, 1984. The results are presented here in nearly chronological order.

Four "machinable" ceramics were ordered for machinability testing so that an optimum ceramic could be selected for in-house machining. Samples of Zircar fibrous Al_2O_3 , Macor glass/ceramic, boron-nitride, and Aremcolox 502-1100 were subsequently received and tested. Boron-nitride demonstrated the best machinability of the group. It also demonstrated good bonding with both copper tubing and other boron-nitride surfaces, using either Torr-seal or Ecobond 286 epoxies. Boron-nitride also has good thermal conductivity--about three times that of Al_2O_3 and equal to that of BeO . A thermal conductivity chart from the Carborundum Corp. is shown in Figure 14.

A single-channel waveguide, 2 mm x 2 mm x 20 cm, was cut into a boron-nitride plate for discharge and vacuum testing. Three 2-mm-diameter holes were drilled for gas inlet and outlet ports, and a central anode with one cathode at each end was formed from quarter-inch-diameter copper tubing surrounding the gas ports. The test channel is shown in Figure 15.

The voltage and current characteristics of a 3:1:1::He:N₂:CO₂ gas mixture were measured at pressures of 50, 90, 180, and 300 Torr. There were actually two discharges (a "split" discharge with a common central anode) and the discharge length was 10.5 cm, including the distances from the channel to the copper electrodes. The channel was covered with Pyrex slides and Eccobond 286 epoxy.

Figure 16 shows the raw current vs voltage data. It is evident that the discharge was operating in the negative resistance region, because the current increases as the anode-to-cathode voltage decreases. The differential resistance (slope⁻¹) is equal to a small negative number, and the discharge appears to be almost a constant

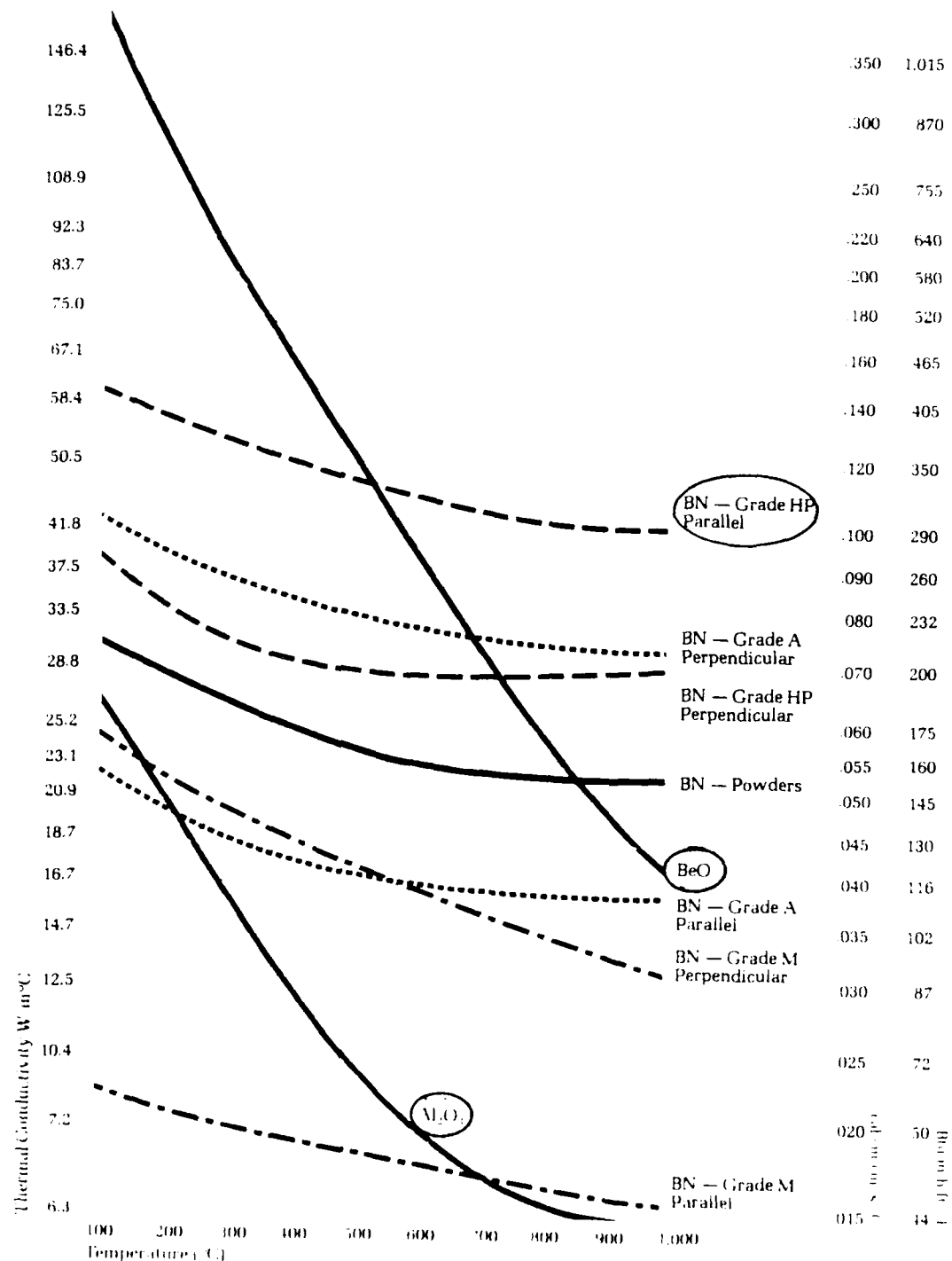


FIGURE 14. THERMAL CONDUCTIVITY OF COMBAT BORON NITRIDE

WAVEGUIDE DISCHARGE TEMPERATURE TEST

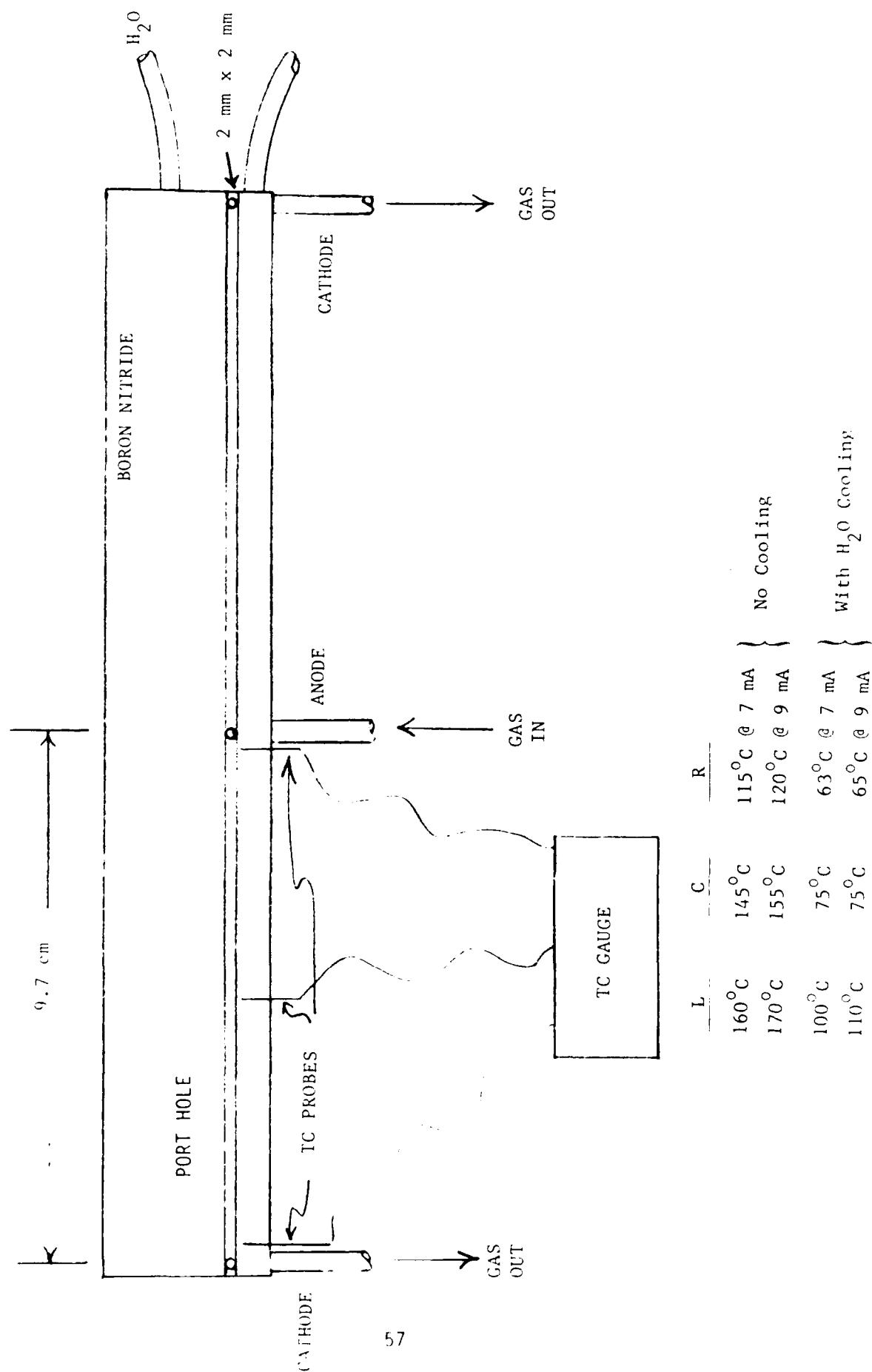


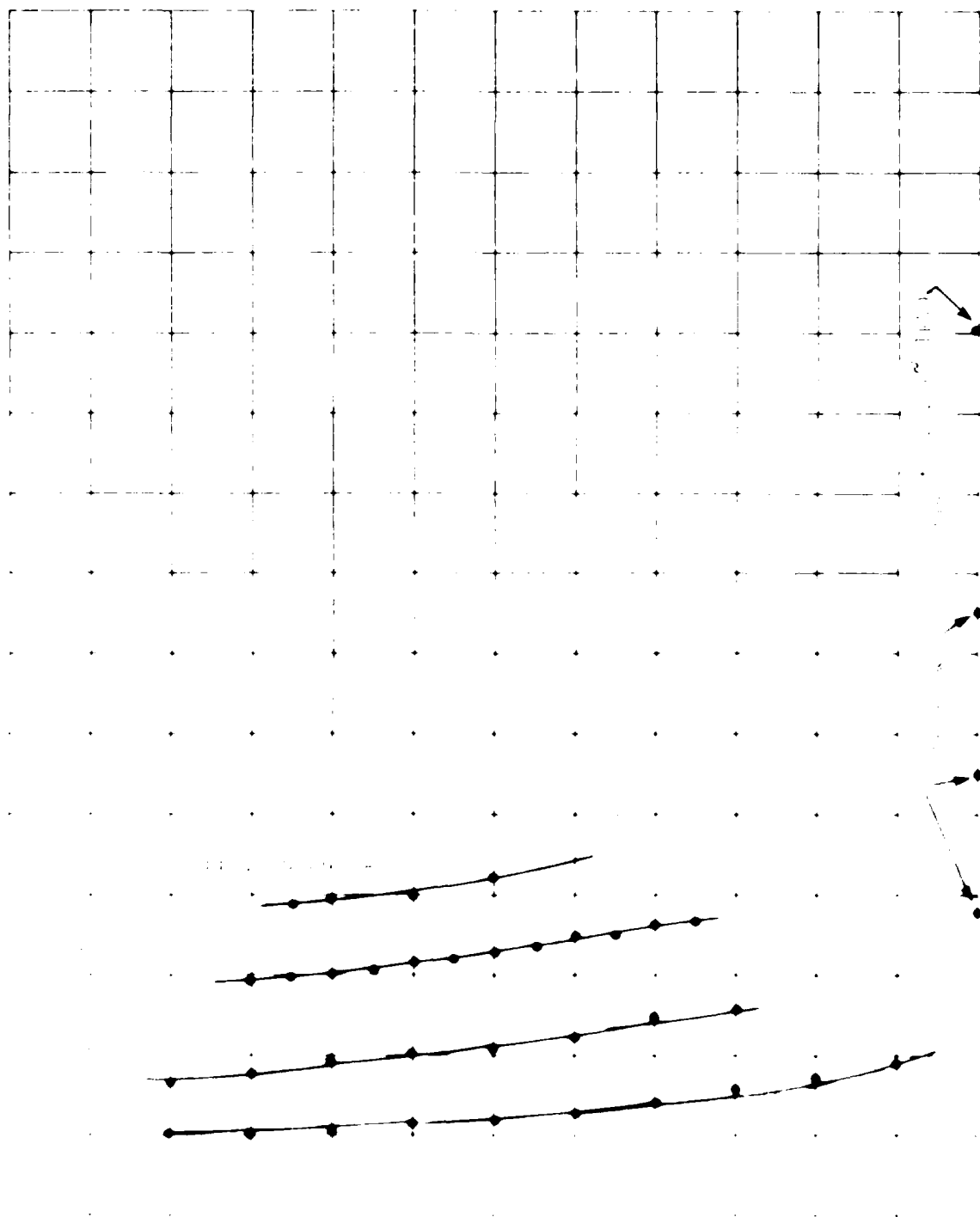
FIGURE 15. SINGLE CHANNEL TEST DEVICE

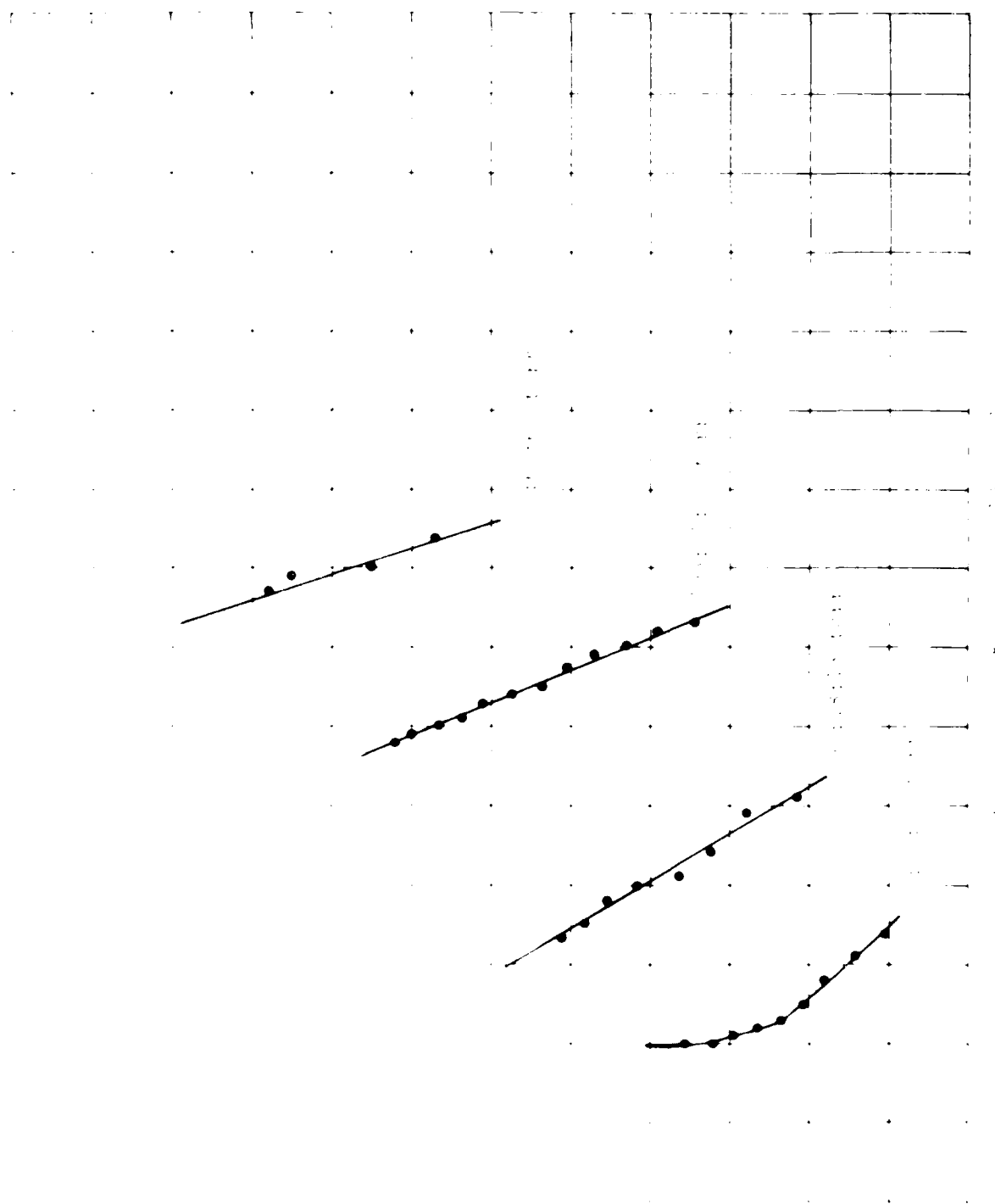
voltage drop for all currents. The 3:1:1 mixture at 175 Torr total pressure was found to be optimum for the previous 1 mm x 1 mm waveguide laser. From scaling theory we would expect the 53:18:18 Torr mixture to be optimum for a 2-mm x 2-mm waveguide although optimum gas ratios will differ somewhat, thus affecting the total pressure for maximum output.

Assuming a 1 kV cathode fall for the copper tube cathodes, the power loading, $\vec{J} \cdot \vec{E}$, is plotted as a function of V_{gas} and I_{gas} in Figures 17 and 18. The gas resistivity as a function of V_{gas} and I_{gas} is also plotted in Figures 19 and 20.

Based on the voltage/current data of Figure 16 and the observed satisfactory discharge uniformity with only 1 M Ω ballast resistance, six power supplies with variacs and resistor chains were ordered. A Hipotronics 30 kV @ 10 mA power pack module was the best price alternative, and this supply would have allowed us to use 2 M Ω ballast and go to 30 cm long waveguide devices if time and money had permitted. Because six power supplies were required, one for each of the 2x3 array waveguides, regulated power supplies would have been a significant fraction of the contract budget. The Hipotronic power packs were an order of magnitude less expensive, and it was felt that adequate filtering could be achieved using inductors and capacitors.

The cooling capability of the BN waveguide material was measured during discharge testing. A 1/8-inch copper tube (tracer) was epoxied to the BN plate as shown in Figure 15. Three small holes were drilled to 0.5 mm from the waveguide at the cathode (C), middle (M), and anode (A). With no water cooling the temperature exceeded 170°C at the cathode end causing fracture of the Pyrex top plates and oxidation of the Eccobond 286 epoxy. With tap water cooling, the temperature was kept at 110°C at 9 mA and 100°C at 7 mA as shown. Optimum gas temperature for P(20) lasing is approximately given by





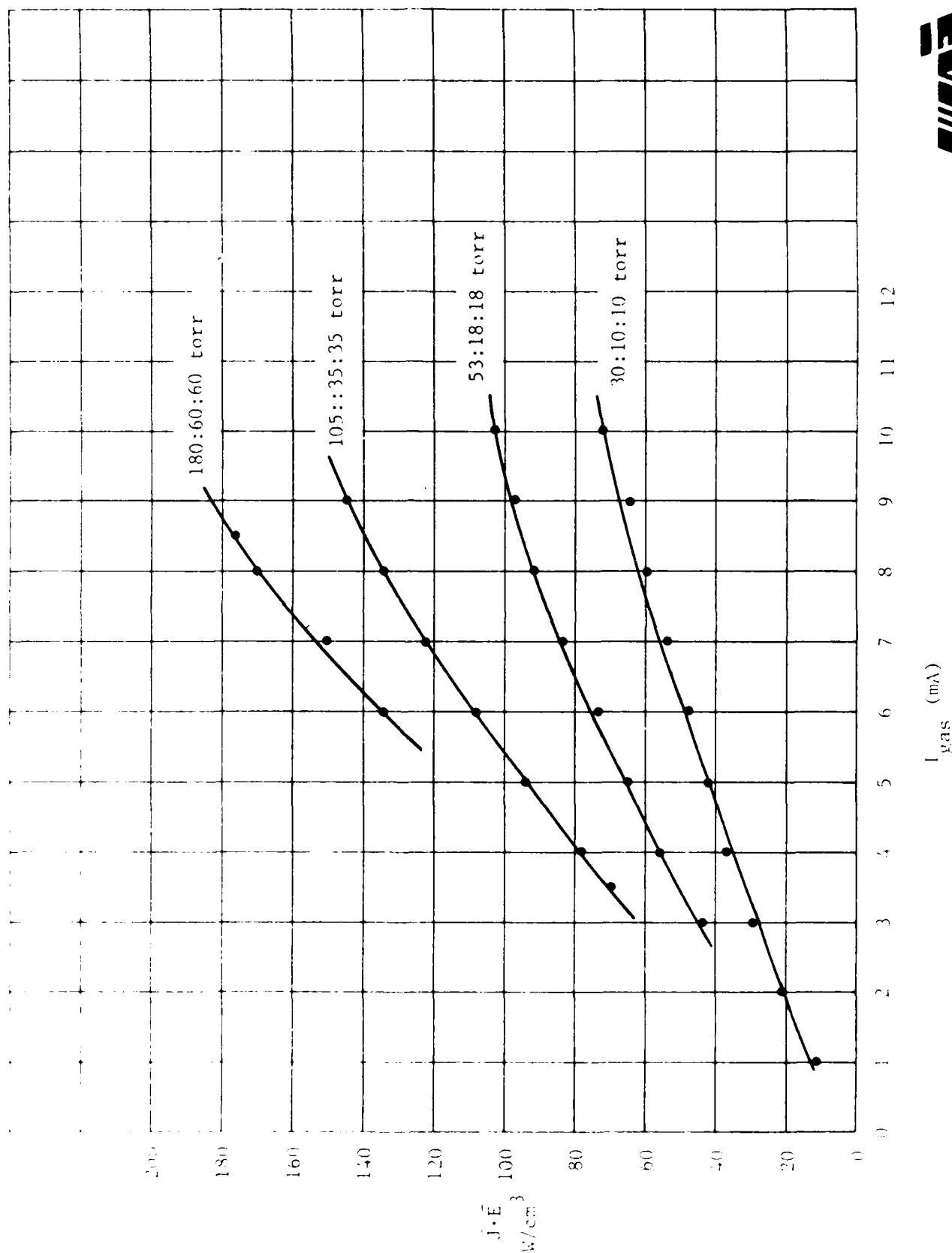


FIGURE 18. TEST CHANNEL POWER LOADING 2 mm x 2 mm x 20 cm GUIDE, 1 MC BALLAST



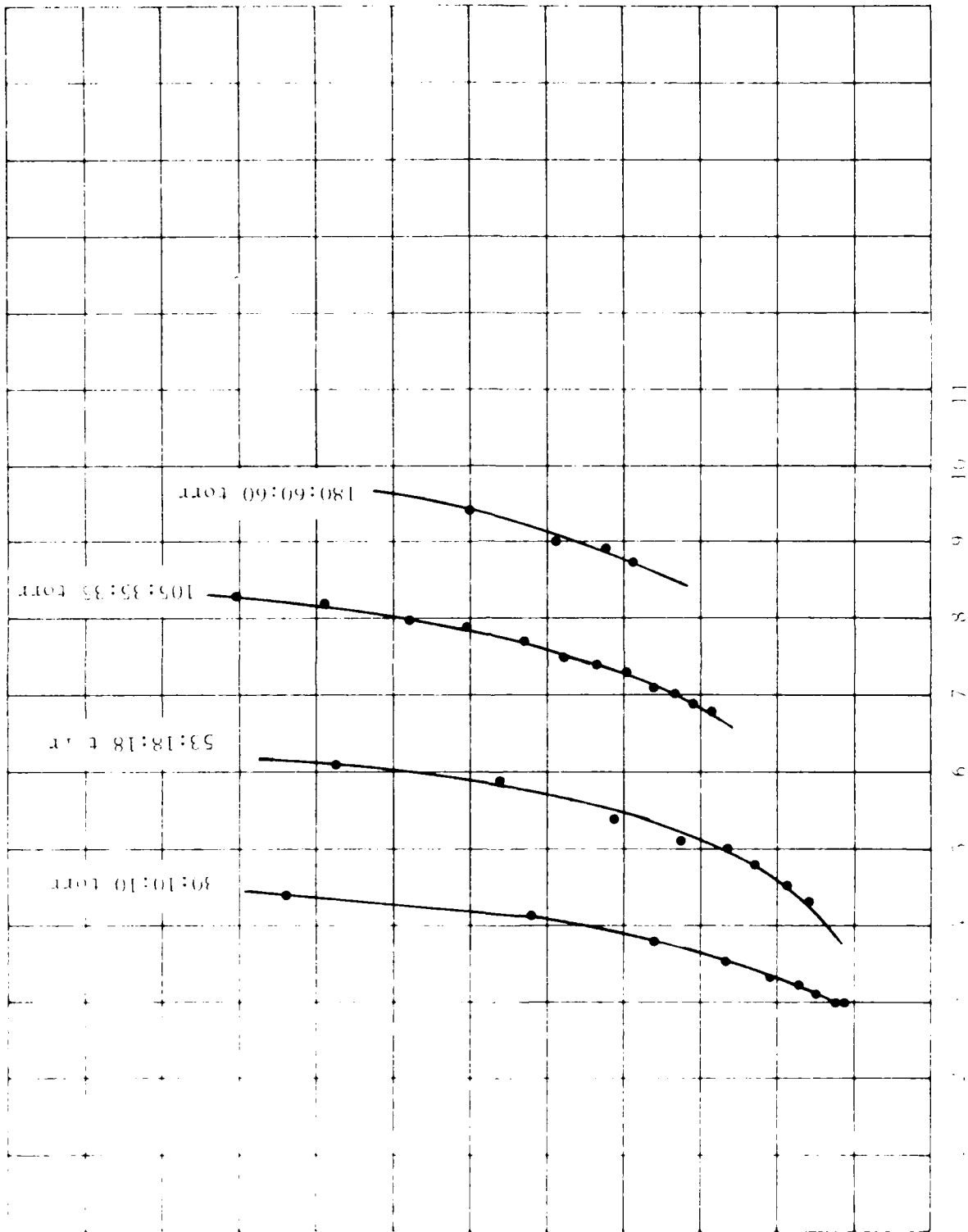
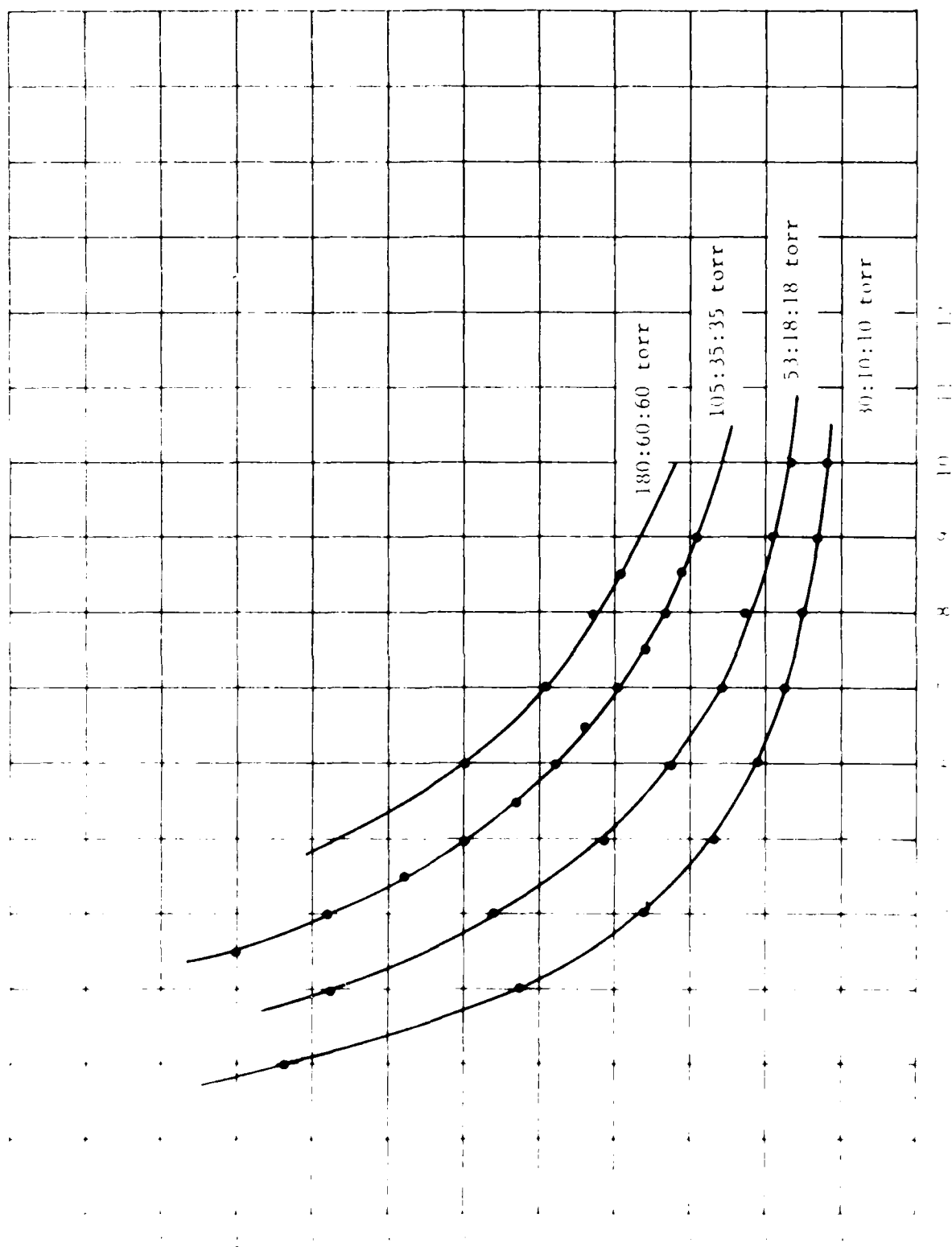


FIGURE 19. TEST CHAMBER RESISTIVITY 2 mm x 2 mm x 20 cm GUIDE, 1 MΩ BALLAST



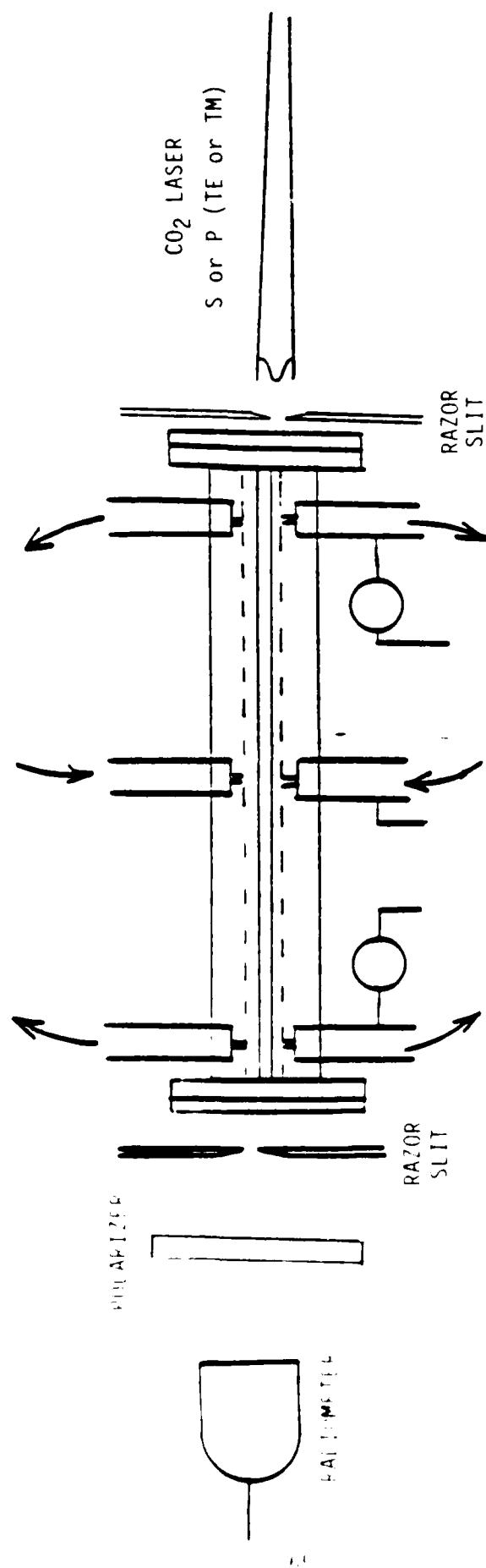
$$J_{\max} = \sqrt{\frac{kT}{2hcB}} - 1/2 = 19 \quad (121)$$

$$\therefore T_{\text{gas}} = 152^{\circ}\text{C}$$

where B is 0.38714 cm^{-1} .

The boron-nitride material appeared to be excellent for waveguide CO_2 laser fabrication using this "tracer" cooling technique where the water is flowed through copper tubing which is epoxied to the ceramic. Consequently a 1×7 array 20-cm-long laser was designed and constructed using boron-nitride. It was felt that this linear array would allow us to start where we left off (1×2 array) and give us familiarity with the reflection grating and water cooling problems before starting the 2×3 array final design. There were considerable water cooling "problem," with the 1×7 device as will be discussed. Seven waveguides were chosen because six power supplies were required for the 2×3 array, and there was one pair of lower voltage supplies left from the 1×2 array device shown in Figure 1. The pair were used in series for the seventh channel.

While the 1×7 array device and the six power supplies were being fabricated, the radiation coupling from one waveguide to the next was measured using the old $10 \text{ mm} \times 10 \text{ mm} \times 10 \text{ cm}$ waveguide as a single port from which the is shown in Figure 21. By propagating TE_{10} polarized light parallel to the central inner plate surface 1.26 cm from right edge of the waveguide, a part of it left leaked through to the other waveguide. The leakage rate of the leaked radiation was $1.2 \times 10^{-4} \text{ W/cm}^2$ when the 1×7 array was first fabricated. With one waveguide connected to the other, the leakage rate of the leaked radiation was $1.2 \times 10^{-4} \text{ W/cm}^2$ when the 1×7 array was first fabricated. When the 1×7 array was first fabricated, the leakage rate of the leaked radiation was $1.2 \times 10^{-4} \text{ W/cm}^2$ when the 1×7 array was first fabricated.



COUPLING $\approx 8 \times 10^{-4}$ S POLARIZATION, 8:1::S:P
 ≈ 0.13 P POLARIZATION, >100:1::P:S

FIGURE 21. WAVEGUIDE ARRAY EXPERIMENT (16 Aug. '84)

The incident laser beam was nearly a plane wave or "top hat" distribution, thus propagation losses and coupling were considerably higher than for a propagating HE_{11} mode passing through the channel once. Nevertheless, we can compare the theory of Section 3 to these data and get a rough idea of their agreement. For unit power in, the output power from the transmission channel would be

$$P_{out} = e^{-\alpha_{TE}x} \quad (122)$$

neglecting power coupling back into the transmission channel, and the coupled power would be

$$P_{coupled} = (1 - e^{-\alpha_{TE}x}) T_{TE}'^2 \quad (123)$$

neglecting scattering and absorption losses in the ZnSe. The ratio is then given by

$$\frac{P_{coupled}}{P_{out}} = \frac{(\alpha_{TE}x) T_{TE}'^2}{1 - e^{-\alpha_{TE}x}} \approx 8 \times 10^{-4} \quad (124)$$

where the exponentials have been expanded. Similarly for the TM polarization

$$\frac{P_{coupled}}{P_{out}} = \frac{(\alpha_{TM}x) T_{TM}'^2}{1 - e^{-\alpha_{TM}x}} \approx 0.13 \quad (125)$$

Taking the ratio of equations 124 and 125

$$\frac{(\alpha_{TM}x) T_{TM}'^2}{(\alpha_{TE}x) T_{TE}'^2} = \frac{0.13}{8 \times 10^{-4}} = n^2(n^4) \quad (126)$$

from equations 87 and 92. Solving 126 for n we find

$$n = 1.9 [\cong 2.4 \text{ for ZnSe}] \quad (127)$$

which is not too far from the refractive index of ZnSe.

The reflection grating selected for the 7×1 array and the 2×3 array was the PTR Corp. ML-303. The grating has a line spacing of 150 lines/mm as shown in Figure 22. The Littrow condition is met at an angle of incidence of 52.66:

Thus the waveguide subtends

$$(2\text{mm}/\sin 37.34^\circ) \times 150 \text{ \AA/mm} \quad (128)$$

$$= 495 \text{ lines} \quad (129)$$

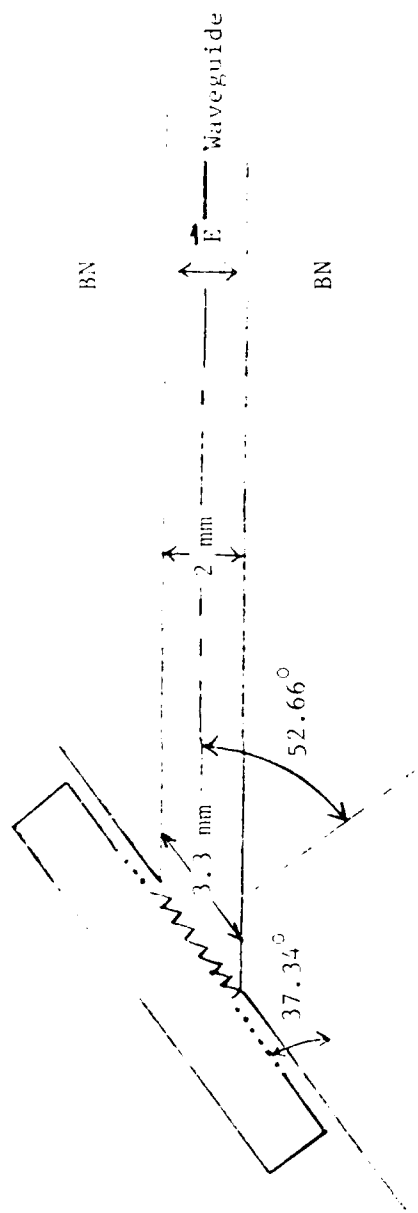
The resolution using the Rayleigh criterion of having the diffraction maximum of λ at the same angle as the diffraction minimum of $\lambda + \Delta\lambda$ is

$$\Delta\lambda = \lambda/495 = 10.6 \text{ \AA}/495 \quad (130)$$

$$= 0.021 \text{ \AA} \quad (131)$$

The difference in wavelength between the P(20) and P(18) lines, the smallest $\Delta\lambda$ we expected to work with, is 0.020 μm . Thus, it appears that the ML-303 marginally had the required resolution to select the various CO_2 lasing transitions.

Reflection efficiency of the ML-303 grating is shown in the insert of Figure 22. Note that the blaze angle is designed to achieve maximum reflection of the E-field perpendicular to the grating grooves and not for maximizing the reflection of unpolarized light. The E-field direc-



Littrow Condition: $\sin \theta = \frac{\lambda}{2D}$

$$D = \frac{1\text{mm}}{150} = 6.67\mu\text{m line spacing}$$

$$\theta = \sin^{-1} \left(\frac{10.6\mu\text{m}}{2(6.67\mu\text{m})} \right) = 52.66^\circ$$

Resolution:

$$N = \frac{2\text{mm}}{\sin 37.34^\circ} \times 150\text{L/mm} = 495$$

$$\Delta\lambda = \lambda/495 = 0.021\mu\text{m Rayleigh Criterion}$$

$$P(20) - P(18) = 0.020\mu\text{m}$$

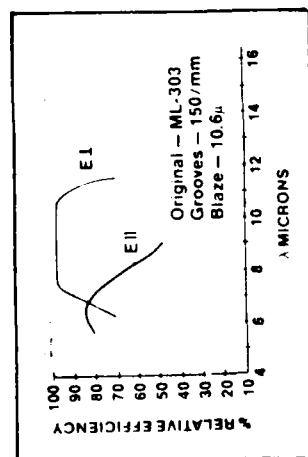


FIGURE 22. IR GRATING SELECTION

tion will be parallel to the ZnSe intercavity windows which was the preferred lasing mode polarization of the previous 1 x 2 array device.

The interwaveguide windows were fabricated by Janos Optics, Inc. The windows were made of optical quality ZnSe and KCl, and the polished windows consisted of:

1. 160 ZnSe: 1 mm x 4 mm x 20 mm (+0, -0.2)
2. 160 KCl: 1 mm x 4 mm x 20 mm (+0, -0.2)
3. 32 ZnSe: 1 mm x 18 mm x 25 mm (+0, -0.2)
4. 32 KCl: 1 mm x 18 mm x 25 mm (+0, -0.2)

All windows were 60/40 surface finish, $\lambda/20$ at 10 μ m flatness, and less than 3 arcminutes of wedge angle. The 1-mm x 4-mm x 20-mm plates separated the 1 x 7 waveguides and the two 1 x 3 waveguide halves of the 2 x 3 device. The larger 1-mm x 18-mm x 25-mm plates were used to separate the two halves of the 2 x 3 device. The lengths of the plates were as long as could easily be polished and handled by Janos Optics.

Windows were fabricated of two materials to offer the use of two different refractive indices (2.4 and 1.5) between the waveguides. At the time it was felt that this alternative might prove useful in achieving phase-locking. In Section 3 it was shown that TE polarization coupling is only a weak function of the refractive index. These windows were long lead items and were ordered early in the program. Consequently, the final details of the 1 x 7 device and 2 x 3 device were designed around the dimensions of these windows.

The vacuum and gas flow system is shown in Figure 23. Precision gas flow meters from MG Scientific Gases measure the flow rates of the CO₂, N₂, and He laser gases. A fourth flowmeter for a small xenon flow was also added. Pressure upstream of the flowmeters was maintained at the specified 15 PSIG by the regulators on each gas tank. Total pressure upstream of the waveguides at the central anode gas inlet was measured by a precision Wallace-Tiernen pressure gauge. The

gas exhaust ports at each cathode fed out through a valve to a roughing pump. Closing down this valve allowed control of the total gas pressure inside the waveguides. It was always found, however, that maximum flow rate always produced maximum laser power, and the valve was always left open. Initially an 0.7 CFM roughing pump from the 1 x 2 device program was used to provide the vacuum. This was replaced early in the program by a 7.0 CFM to provide greater flow for the 1 x 7 and 2 x 3 devices.

Some difficulty was encountered using the flowmeters. They were designed to measure the flow from a 15-PSIG source out to an atmospheric pressure (15 PSIA) vessel for chemical reaction applications. Consequently, flowing from 15 PSIG to near vacuum invalidated the flow rate curves supplied for each tube size and each gas. In addition "backstreaming" caused the indicated flow to change when another gas flow rate was increased or decreased. After much experimentation the needle valves supplied at the entrance of each flow tube were opened all the way and thus taken out of the flow path. A new needle valve was installed at the outlet of each flow tube to choke the flow at that point. Now, since the gas inside the flow tube was at 15 PSIA instead of at atmospheric pressure, the calibrated flow curves could be calibrated by \sqrt{P} as given by other calibration curves for different tube materials. In addition backstreaming was eliminated.

Two separate power supplies as shown in Figure 4 were used to energize the 1 x 3 array of waveguides. The one operating at 100 kHz was connected to the strip line 300 power pack shown in Figure 5. The second power supply at 400 kHz operated at 100 W and was connected to the strip line 300 power pack. The current to each part of the strip line was controlled by two potentiometers. The strip line was energized by two power packs, one operating at 100 W and the other at 100 W. The two power packs were connected to the strip line by two separate cables.

The power supply for the 1 x 7 array was a 100 W power pack connected to the strip line 300 power pack. The power supply for the 2 x 3 array was a 100 W power pack connected to the strip line 300 power pack.

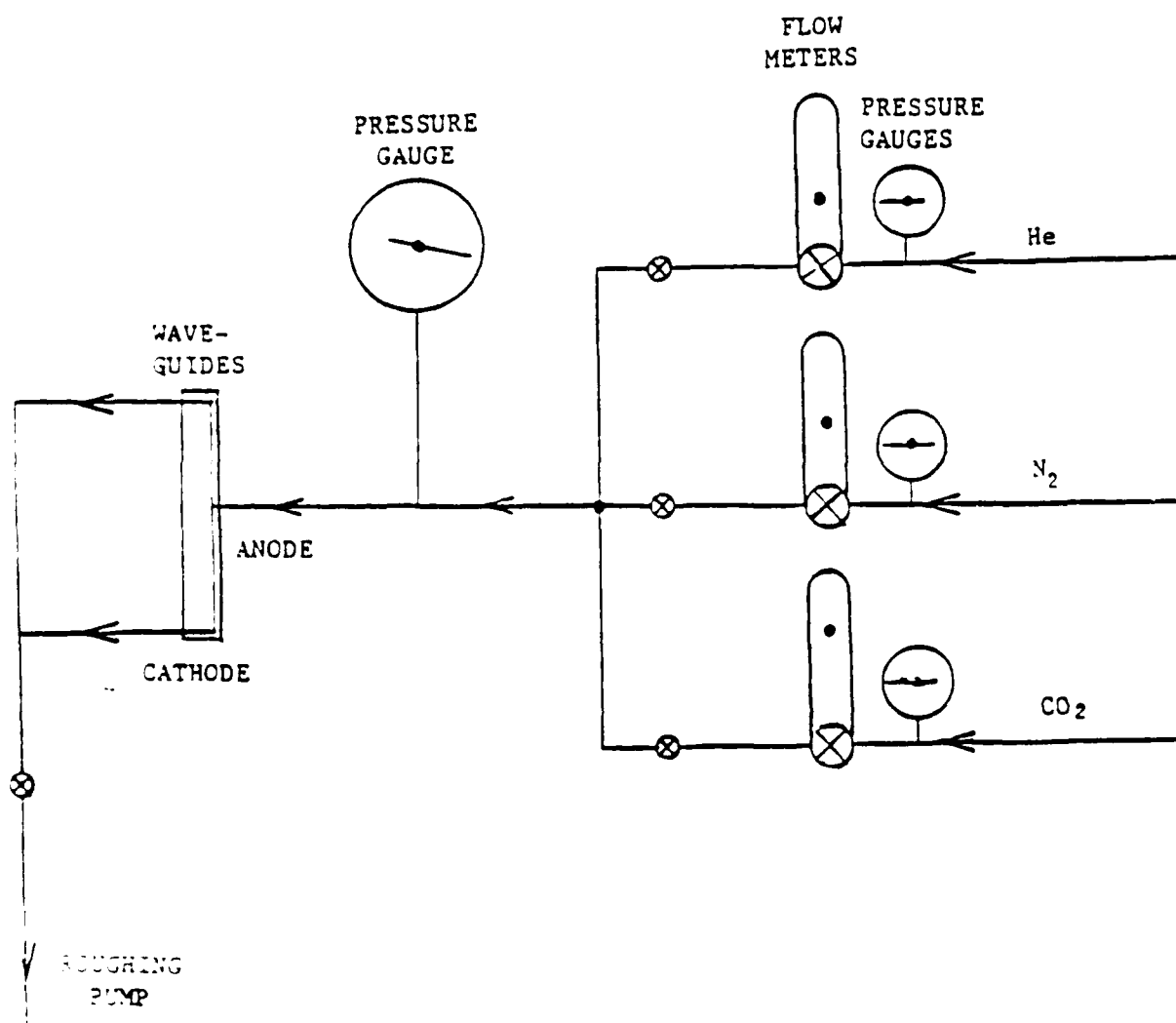


FIGURE 2. WAVEGUIDE SPRAY GAS FLOW SYSTEM

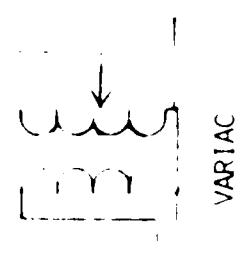
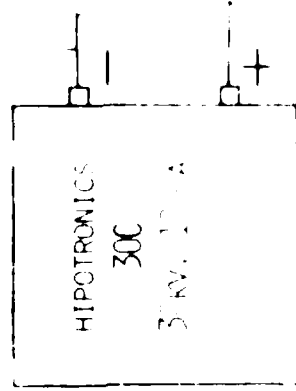
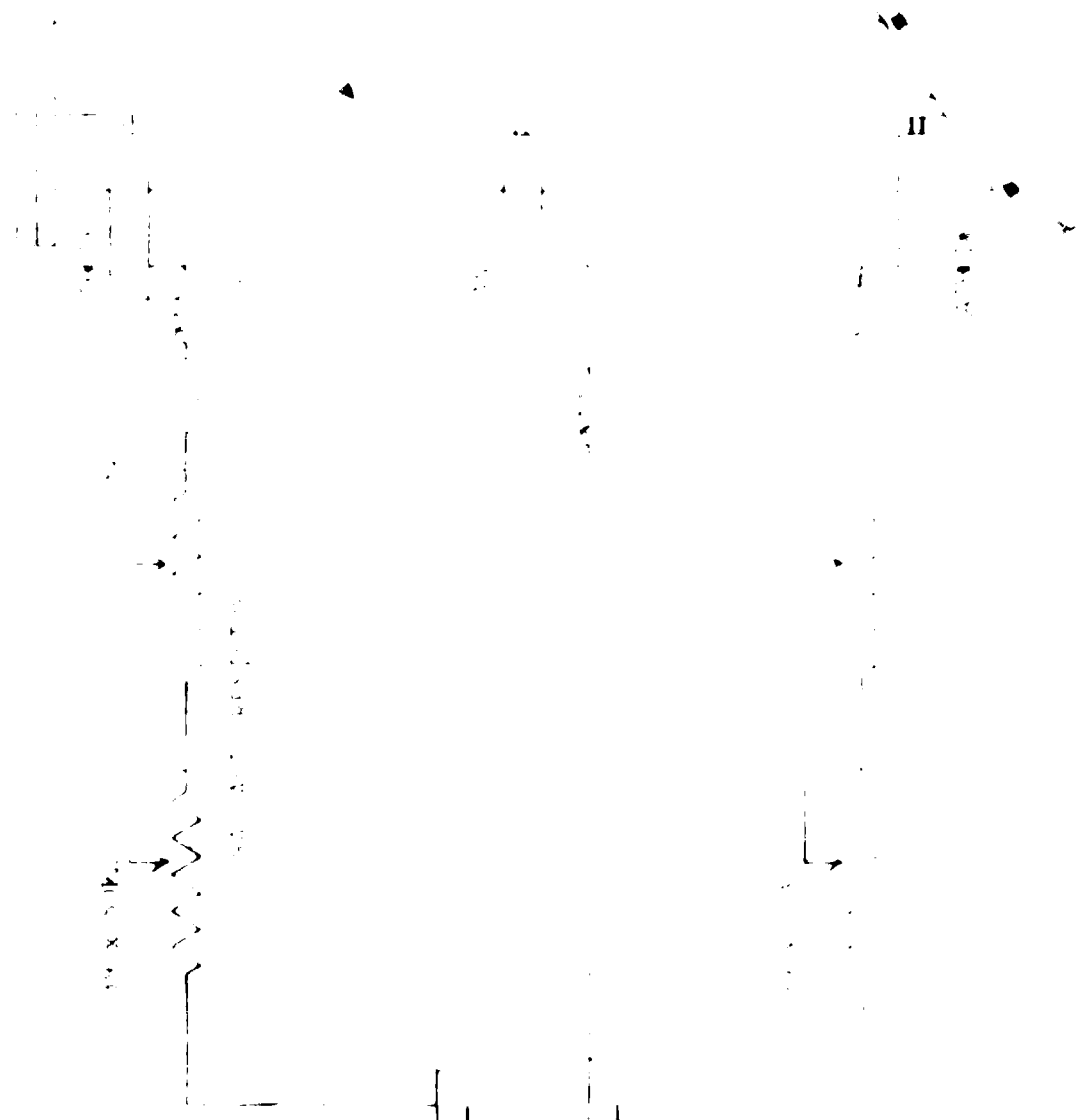
fluctuations. During operation of both the 1x7 and the 2x3 devices, plasma oscillations and discharge jumping were a problem. These will be discussed in more detail in the next two sections. The inductor did, however, reduce the current fluctuations by about a factor of two.

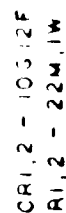
6.1 One by Seven Array Device

Fabrication of the 1x7 array was completed about six months after the start of the program. A side view of the device is shown in Figure 26, and an end view is shown in Figure 27. Gas inlet and exhaust is through three manifolds opposite the central anode and two cathodes, respectively. The electrodes are made of 1/16" stainless steel rod, and the body is constructed from blocks of boron nitride epoxied together with Emerson and Cummings 286 epoxy.

Photographs at various stages of construction are shown in Figure 23-a through 28-f. Figure 23-a shows the lower BN plate underside revealing the water cooling chambers. Figure 23-b shows the waveguide side of this lower plate. The smaller grooves each 1-mm wide hold the interwaveguide 4-mm x 20-mm x 1-mm replaceable windows. The upper BN plates are seen in Figure 28-c and 28-d. The upper cooling chambers and the waveguide channels are shown. Also visible are the seven stainless steel electrode rods for the split discharge in each waveguide. The endcaps to hold the output coupler and reflection grating are in the foreground. Note that the inner end-cap piece is designed to be a waveguide "extension" bringing the waveguide as close as possible to the reflectors and going beyond the discharge volume. This minimized the coupling losses into and out of the waveguide.

Figure 23-e shows the device with the yellow colored interwaveguide windows loaded into their channels. The last plates on both the left and right side are made of BN to fill the channels completely to prevent optical coupling at the waveguide ends. Figure 28-f shows the device with the upper plates in position. The water cooling





5

100

1

CA 11

1 2 3 4 5 6 7 8 9 10 11 12 13 14 15 16 17 18 19 20 21 22 23 24 25 26 27 28 29 30 31 32 33 34 35 36 37 38 39 40 41 42 43 44 45 46 47 48 49 50 51 52 53 54 55 56 57 58 59 60 61 62 63 64 65 66 67 68 69 70 71 72 73 74 75 76 77 78 79 80 81 82 83 84 85 86 87 88 89 90 91 92 93 94 95 96 97 98 99 100 101 102 103 104 105 106 107 108 109 110 111 112 113 114 115 116 117 118 119 120 121 122 123 124 125 126 127 128 129 130 131 132 133 134 135 136 137 138 139 140 141 142 143 144 145 146 147 148 149 150 151 152 153 154 155 156 157 158 159 160 161 162 163 164 165 166 167 168 169 170 171 172 173 174 175 176 177 178 179 180 181 182 183 184 185 186 187 188 189 190 191 192 193 194 195 196 197 198 199 200 201 202 203 204 205 206 207 208 209 210 211 212 213 214 215 216 217 218 219 220 221 222 223 224 225 226 227 228 229 230 231 232 233 234 235 236 237 238 239 240 241 242 243 244 245 246 247 248 249 250 251 252 253 254 255 256 257 258 259 260 261 262 263 264 265 266 267 268 269 270 271 272 273 274 275 276 277 278 279 280 281 282 283 284 285 286 287 288 289 290 291 292 293 294 295 296 297 298 299 300 301 302 303 304 305 306 307 308 309 310 311 312 313 314 315 316 317 318 319 320 321 322 323 324 325 326 327 328 329 330 331 332 333 334 335 336 337 338 339 340 341 342 343 344 345 346 347 348 349 350 351 352 353 354 355 356 357 358 359 360 361 362 363 364 365 366 367 368 369 370 371 372 373 374 375 376 377 378 379 380 381 382 383 384 385 386 387 388 389 390 391 392 393 394 395 396 397 398 399 400 401 402 403 404 405 406 407 408 409 410 411 412 413 414 415 416 417 418 419 420 421 422 423 424 425 426 427 428 429 430 431 432 433 434 435 436 437 438 439 440 441 442 443 444 445 446 447 448 449 450 451 452 453 454 455 456 457 458 459 460 461 462 463 464 465 466 467 468 469 470 471 472 473 474 475 476 477 478 479 480 481 482 483 484 485 486 487 488 489 490 491 492 493 494 495 496 497 498 499 500 501 502 503 504 505 506 507 508 509 510 511 512 513 514 515 516 517 518 519 520 521 522 523 524 525 526 527 528 529 530 531 532 533 534 535 536 537 538 539 540 541 542 543 544 545 546 547 548 549 550 551 552 553 554 555 556 557 558 559 560 561 562 563 564 565 566 567 568 569 570 571 572 573 574 575 576 577 578 579 580 581 582 583 584 585 586 587 588 589 590 591 592 593 594 595 596 597 598 599 600 601 602 603 604 605 606 607 608 609 610 611 612 613 614 615 616 617 618 619 620 621 622 623 624 625 626 627 628 629 630 631 632 633 634 635 636 637 638 639 640 641 642 643 644 645 646 647 648 649 650 651 652 653 654 655 656 657 658 659 660 661 662 663 664 665 666 667 668 669 670 671 672 673 674 675 676 677 678 679 680 681 682 683 684 685 686 687 688 689 690 691 692 693 694 695 696 697 698 699 700 701 702 703 704 705 706 707 708 709 710 711 712 713 714 715 716 717 718 719 720 721 722 723 724 725 726 727 728 729 730 731 732 733 734 735 736 737 738 739 740 741 742 743 744 745 746 747 748 749 750 751 752 753 754 755 756 757 758 759 760 761 762 763 764 765 766 767 768 769 770 771 772 773 774 775 776 777 778 779 780 781 782 783 784 785 786 787 788 789 790 791 792 793 794 795 796 797 798 799 800 801 802 803 804 805 806 807 808 809 810 811 812 813 814 815 816 817 818 819 820 821 822 823 824 825 826 827 828 829 830 831 832 833 834 835 836 837 838 839 840 841 842 843 844 845 846 847 848 849 850 851 852 853 854 855 856 857 858 859 860 861 862 863 864 865 866 867 868 869 870 871 872 873 874 875 876 877 878 879 880 881 882 883 884 885 886 887 888 889 890 891 892 893 894 895 896 897 898 899 900 901 902 903 904 905 906 907 908 909 910 911 912 913 914 915 916 917 918 919 920 921 922 923 924 925 926 927 928 929 930 931 932 933 934 935 936 937 938 939 940 941 942 943 944 945 946 947 948 949 950 951 952 953 954 955 956 957 958 959 960 961 962 963 964 965 966 967 968 969 970 971 972 973 974 975 976 977 978 979 980 981 982 983 984 985 986 987 988 989 990 991 992 993 994 995 996 997 998 999 1000 1001 1002 1003 1004 1005 1006 1007 1008 1009 1010 1011 1012 1013 1014 1015 1016 1017 1018 1019 1020 1021 1022 1023 1024 1025 1026 1027 1028 1029 1030 1031 1032 1033 1034 1035 1036 1037 1038 1039 1040 1

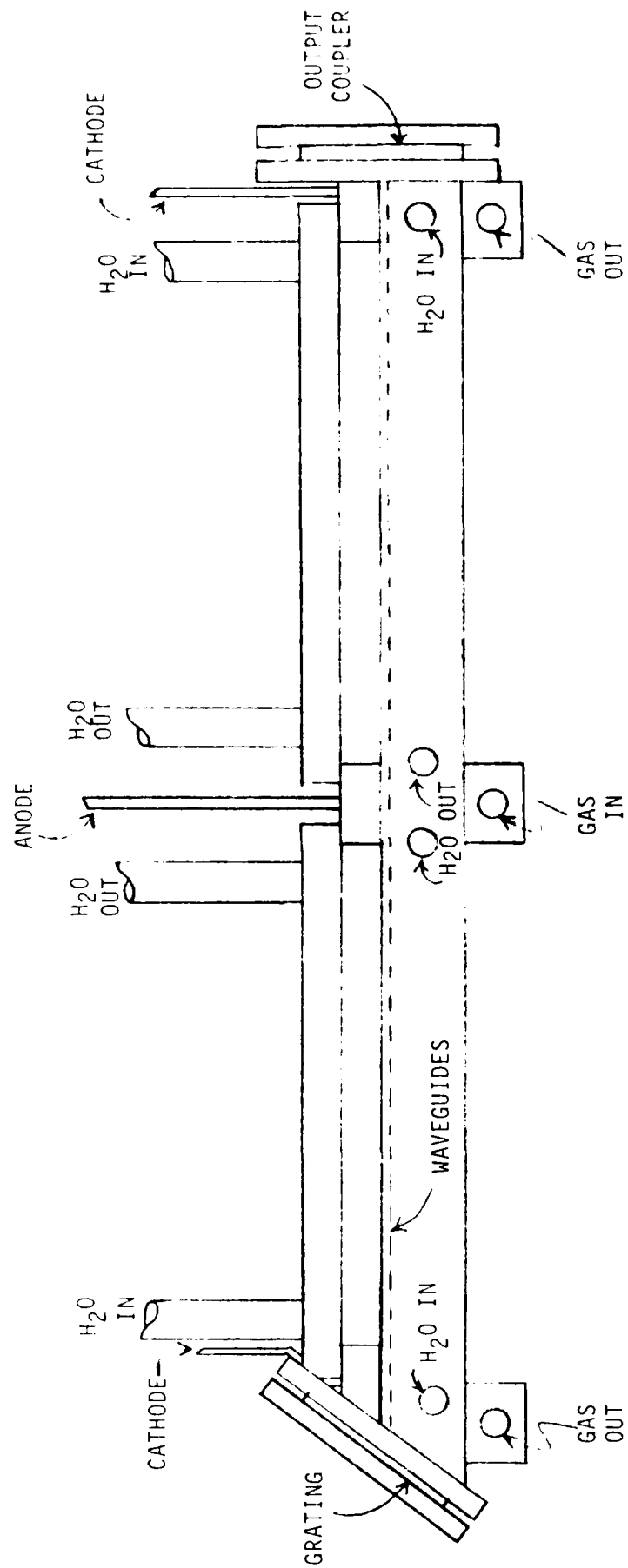


FIGURE 26. WAVEGUIDE ARRAY (7x1) EXTERNAL STRUCTURE

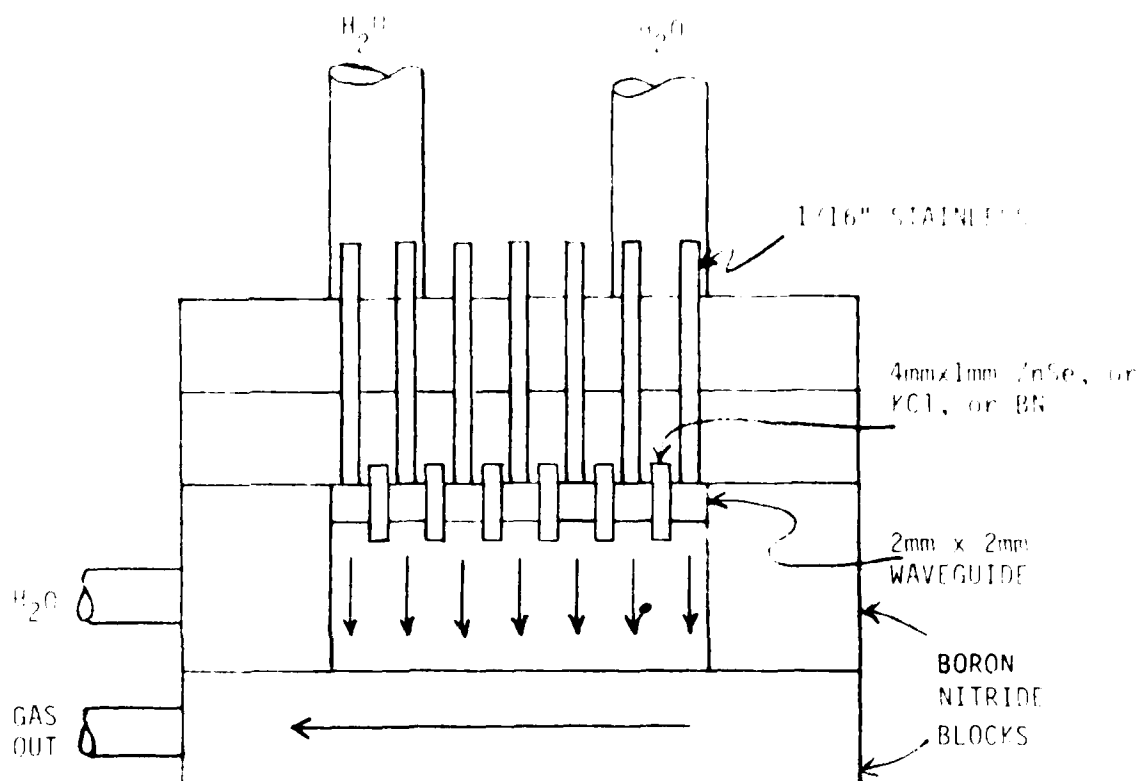
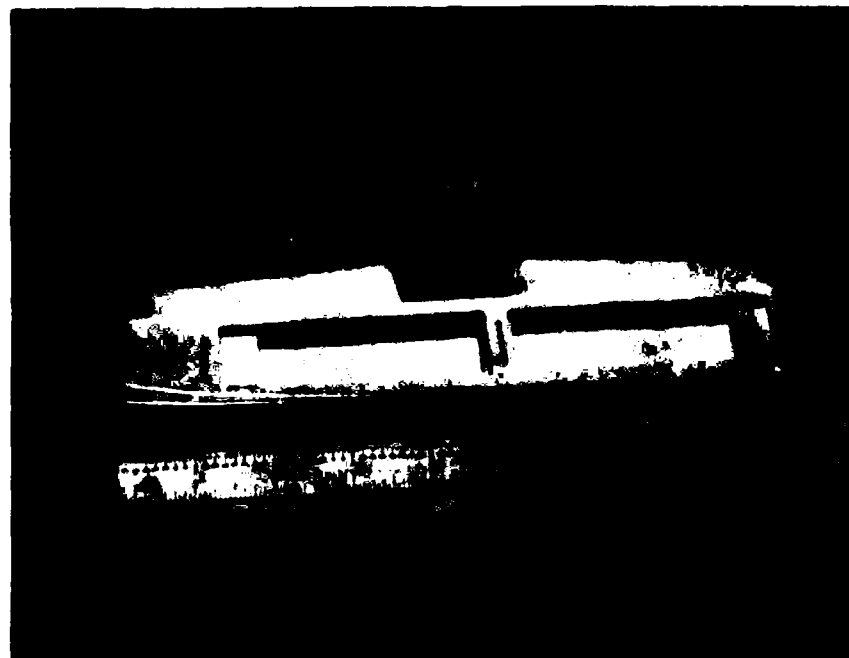
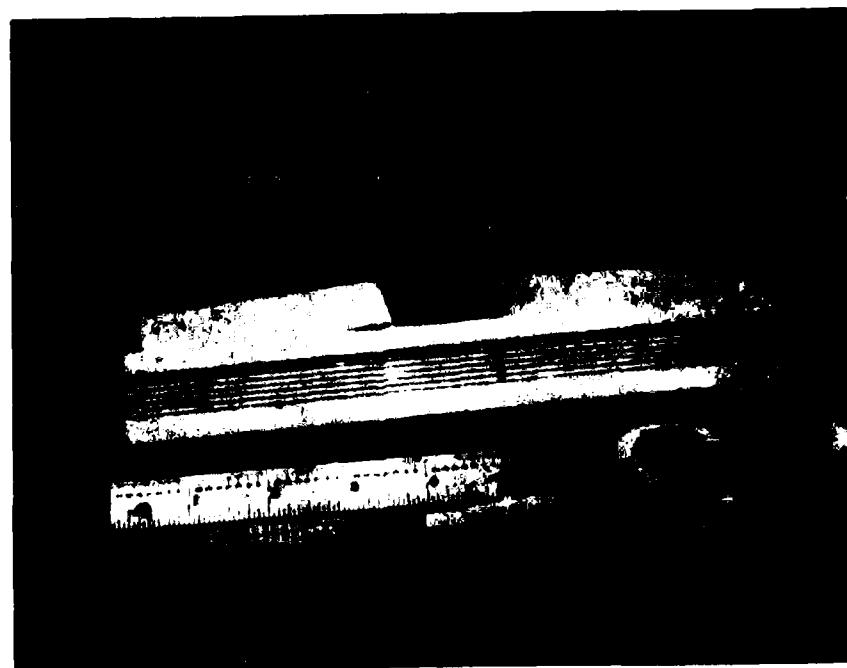


FIGURE 27. 7 x 1 WAVEGUIDE ARRAY END VIEW



a) 1 x 7 Array Device Structure



b) 1 x 7 Array Device Structure

FIGURE 28. 1 x 7 ARRAY DEVICE STRUCTURES



Figure 1

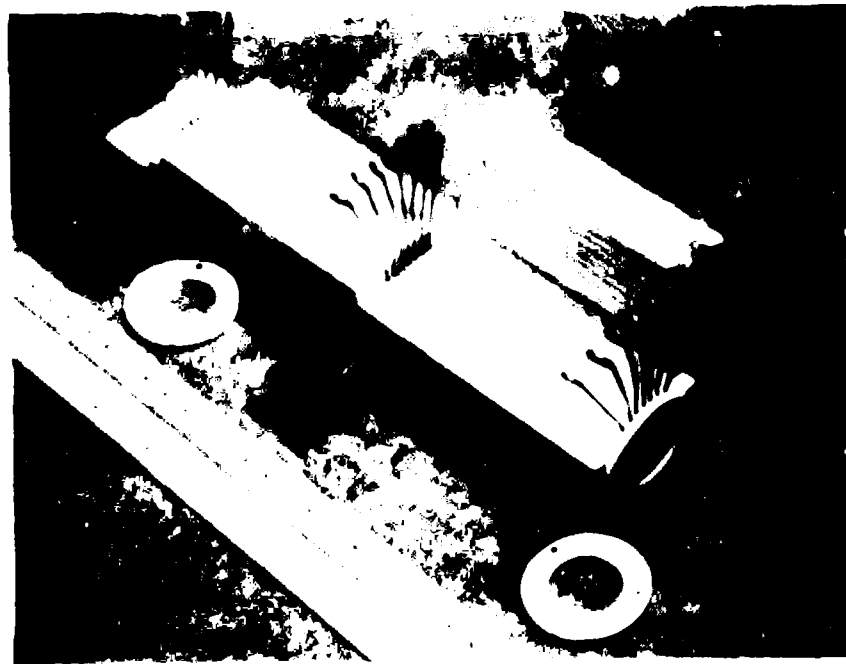
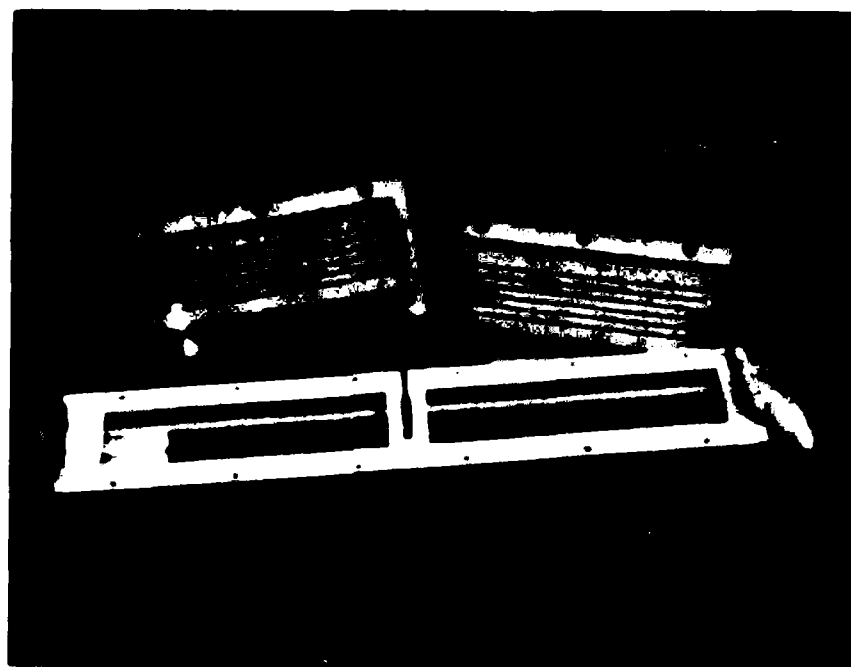
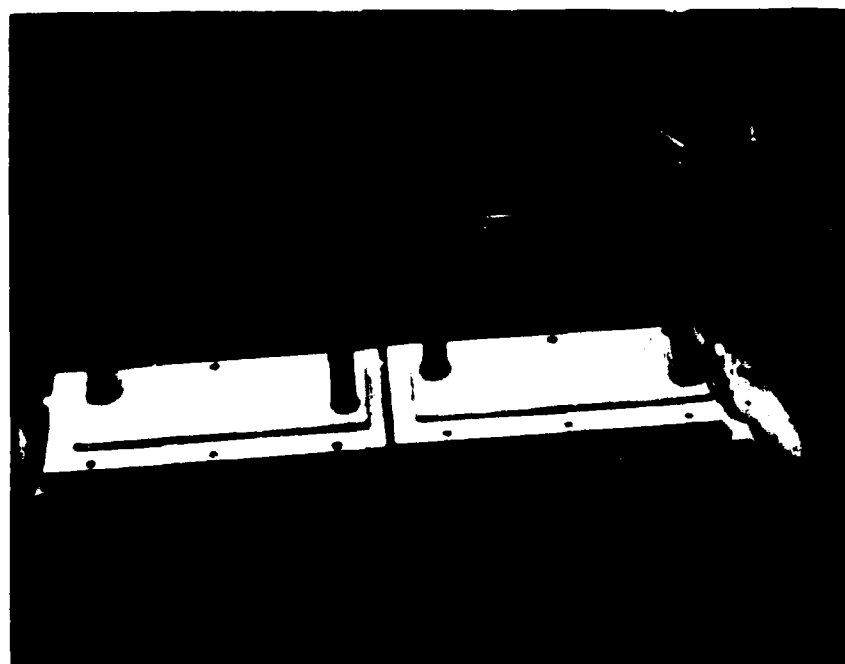


Figure 2

(continued)



e) 1 x 7 Device Structure



f) 1 x 7 Device Structure

FIGURE 2. 1 x 7 ARRAY DEVICE STRUCTURES (Continued)

chambers are covered by a fiberglass plate. There is one water cooling inlet and outlet tube in each upper plate. The waveguide end cap and extension on the right side holds the reflection grating for lasing line selection. The end cap and waveguide extension on the left side holds the output coupler.

The 1x7 device connected to its gas flow system, vacuum pump system, power supplies, and water cooling system is shown in Figure 29. an expanded view showing the gas flow meters, pressure gauges, and gas supply tank is shown in Figure 30. this photograph was taken before needle valves were installed after the flow meters and the valves supplied with the gauge below the flow meter were opened all the way.

Discharges were next run in the seven waveguide channels using 6:1:1 and 7:1:1 ($\text{He:N}_2:\text{CO}_2$) gas flow ratios at 75 Torr and 150 Torr inlet pressures. Plots of discharge current versus discharge voltage were made (not shown here). It was noted that the voltage drops were lower than that of the test channel shown in Figure 15. This was felt to be due to the fact that the discharges no longer made the two 90° turns into and out of the waveguide channel. The electrodes were now flush with the waveguide surfaces as seen in Figure 27. It was also noted that the current versus voltage curves were shaped differently from that of the test channel. The curves showed primarily positive resistance. At the time, this was attributed to the flush cathode and anode geometry. It was later found to be due to the porosity of the boron nitride blocks and the cooling water as described below.

Also during the discharges considerable arcing was observed between one central anode and the adjacent central anodes around the large interwaveguide windows. Improved grounding of the power supplies and the addition of inductive filters in the anode power lines greatly improved discharge uniformity. Fourteen more inductors were then ordered for the cathode power lines for additional filtering as shown in Figure 24.

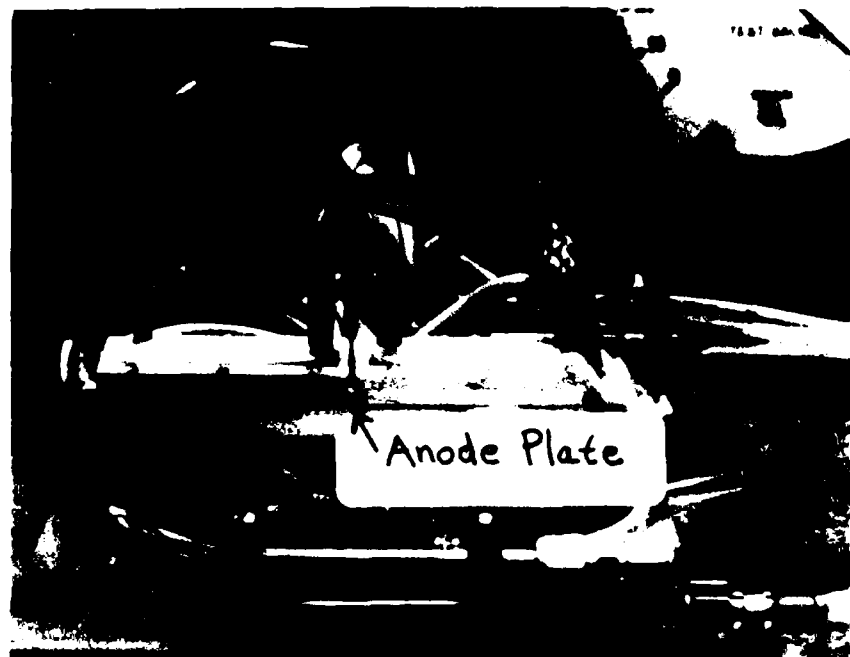


FIGURE 29. 1 x 7 DEVICE WITH GAS FLOW, VACUUM,
WATER AND ELECTRICAL CONNECTIONS

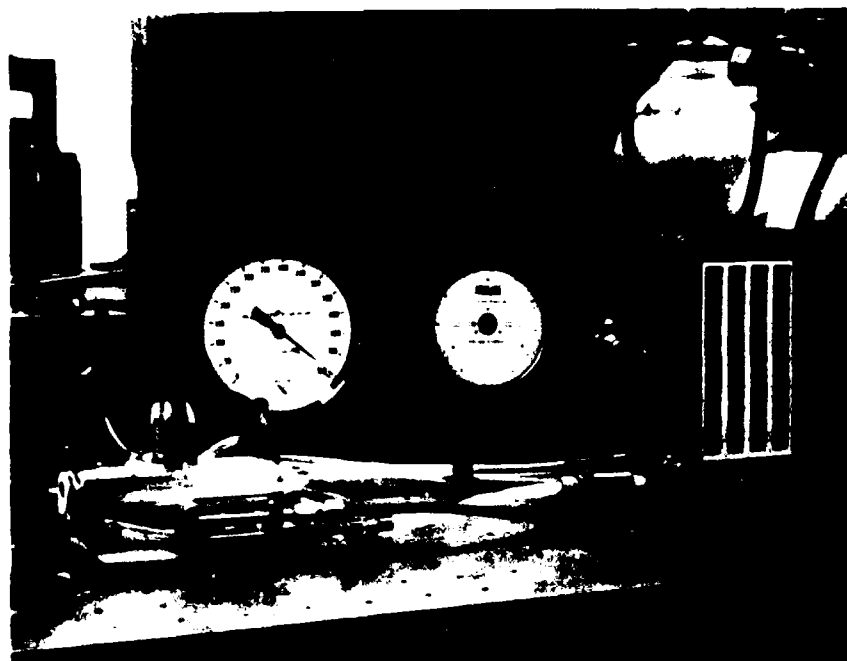


FIGURE 30. 1 x 7 DEVICE WITH GAS FLOW CONTROLS,
GAS TANKS, AND PRESSURE GAUGES

After several hours of discharge running, a deterioration of the BN around the central anodes was observed as a fine BN dust deposit below the central anodes. The dust initially coated the reflection grating (Figure 22) causing the destruction of many grooves. Two new gratings were subsequently ordered. It was initially believed that the BN deterioration was due either to electron bombardment of the BN next to the anode or thermal expansion of the stainless steel anode causing fracturing of the BN. If deterioration became too severe, the plate holding the seven anodes (center of Figure 26) would be removed and replaced by an identical Macor glass ceramic plate.

A 99% reflectivity output coupler and the reflection grating were next installed on the 1x7 waveguide array. The output coupler was aligned using a HeNe laser, but it was not possible to optically align the grating using a 10.6- μ m laser beam at this time. By running discharges at various currents, gas pressures and mixtures, and rotating the grating, it was not possible to achieve lasing. It was believed that the grating misalignment was the culprit.

In view of the BN deterioration at the central anodes, however, it was decided not to continue "tweaking" but to replace the grating with a 2-mm x 20-mm high reflectivity flat mirror and align both optics with the HeNe laser. Seven such mirrors using a silicon substrate with enhanced silver coating were then ordered from Janos Optics. Original delivery of the enhanced silver coated silicon mirrors was promised in two to three weeks, however, delivery time was subsequently slipped to five weeks by the vendor. Consequently, it was decided to disassemble the 1x7 array device in order to examine the BN deterioration which was thought to cause the discharge nonuniformity and cross channel arcing.

Upon disassembly a white soft powder was found coating the insides of the waveguides near the central anodes, yet no deterioration of the BN was observed. The white coating did not plug the gas inlet ports below the central anodes, but it did pile up about one to two centimeters downstream of the anode on both sides and coat the tips of

the stainless steel anodes. It also coated the inside of the waveguides causing fusing of some ZnSe windows and the BN plates to the BN body. Based on this localized build up of the powder 1 to 2 cm downstream of the anodes, it was felt that a chemical reaction must be taking place between the BN and the monoatomic or diatomic oxygen, or CO being produced in the He, N₂, CO₂ gas discharge. Because no such problems were observed in the test discharge waveguide it was also felt that the stainless steel electrodes must be acting as a catalyst since copper electrodes were previously used.

In conversations with Carborundum Corporation personnel, they thought that H₃BO₃, or other BO₃ and BO₂ compounds were being formed in the discharge atmosphere confirming our suppositions. The BO₃ comes from B₂O₃N and B₂O₃ impurities in the BN material. The molecules come out interstitially thus no BN deterioration would be observed just as we found. Also BO₃ and BO₂ compounds are water soluble which the white powder was found to be. Carborundum Corporation personnel suggested using high purity He, N₂, and CO₂ gases and backfilling the device with one atmosphere N₂ when not in use instead of pumping on it. This prevents formation of H₃BO₃ and H₂BO₃ due to small vacuum leaks.

After obtaining this information it was decided to replace the central BN block and its seven stainless steel electrodes with a Machin SiO₂ glass/ceramic block and seven copper anodes. This would reveal if the stainless steel were acting like a catalyst and also prevent the anodes from being covered by the BN impurity compounds. The replaced BN plate is shown in the center of Figures 26 and 27a-c.

The Machin glass/ceramic central anode plate with seven copper anode pins was fabricated and installed in the 1x7 array device. After running some discharges and then pumping on the device overnight, it was found that the chemical buildup was somewhat reduced. Small pin head-size growths could be seen growing from the intersection of the ZnSe interwaveguide windows and the BN body. When the device was

laser with 100 Torr, however, the laser did not lase with a 100 Torr gas mixture.

For the purpose of the various current was measured after at the 100 Torr, the new current density curves after showed a probably a higher current density that was again attributed to the different geometry of the 1x1 device with respect to the test channel.

Experiments with the 1x1 mirrors with enhanced Ag coating were later conducted with a 4:1.25:1::He:N₂:CO₂ gas mixture was made for them, and one was installed on the 1x1 array device. Lasing was attempted with a 100 Torr, however, gas pressures of 100 Torr, 75 Torr, and 50 Torr were tried with a 4:1.25:1::He:N₂:CO₂ gas mixture. Lasing was not observed at 100 Torr upstream pressure in either channel 5 or channel 6, but lasing was observed. Greater than 100 mW was measured in the test channel, but power began to drop off. The power drop off was attributed to heating or irradiance damage of the Si 2mm x 20 mm mirror. A 4:1.25:1::He:N₂:CO₂ at about 60 Torr, the pressure was determined.

A 2 x 20-mm mirror was installed, and only channel #5 was used. The current ranged from 6.2 mA to 7.2 mA for the single waveguide. The current density was the same, and the maximum of 300 mW was observed. Installing a 9% output coupling partial reflector on the 2 x 20-mm mirror lasing was obtained when the 99% reflectivity mirror was installed due to a second damaged 2 x 20-mm mirror.

After the second 2 x 20-mm mirror, lasing was observed in the test channel spontaneously when observed on a phosphor screen. The maximum power from one waveguide was 300 mW. The device was decided to set up the Spicon pyro-lytic coating on the test channel. When the device was tested, it was found that the reflective coating had peeled away from the test channel. The device was then placed in a laser optics believed

that this was the result of a small leak in their coating chambers which they had recently discovered. Consequently, all damaged 2 x 20 mm mirrors were recoated at no charge. [The damage of all of these optical elements was determined soon after as being due to the corrosive compounds produced by water diffusing through the BN plates from the water cooling channels.]

Next, in an effort to obtain simultaneous lasing in more channels of the 1x7 device, Xenon gas handling capability was added to the He, N₂, CO₂ gas delivery system. A 5% flow of Xe was added to the 4:1.25:1 gas mixture at 65 Torr upstream pressure. [The addition of 5% Xe has been reported²⁸ to yield about 25% more laser power attributable to a redistribution of electron energies downward toward the N₂ excitation energy region.] Unfortunately, lasing was not achieved with the 1x7 device using this conceptually straightforward addition.

The background pressure (vacuum leaks) in the seven channels had risen to about 2.8 Torr (upstream) by this time. It had been thought that the Wallace and Tiernan pressure gauge indicated about 2 Torr higher than the actual pressure. However, when the gauge was recalibrated, it was found to be reading correctly. The leaks were therefore much more serious than thought. Typically less than 1 Torr background pressure is allowable for lasing with a flowing gas medium.

Consequently, leak detection and sealing on the 1x7 system was begun next. Unfortunately, the WJSA Helium leak detector was damaged previously and was not operational. Repair of the system took three weeks.

During the time period that the leak detection was being done, the gas flow system was modified. A restriction was placed on each of the four flowmeters (as described in the previous section) at the flowmeter inlets with the purpose of eliminating gas backstreaming into the flowmeters. This was accomplished by welding a 1/8 inch diameter tube to the inlet of each flowmeter, which was then sealed with a 1/8 inch diameter plug.

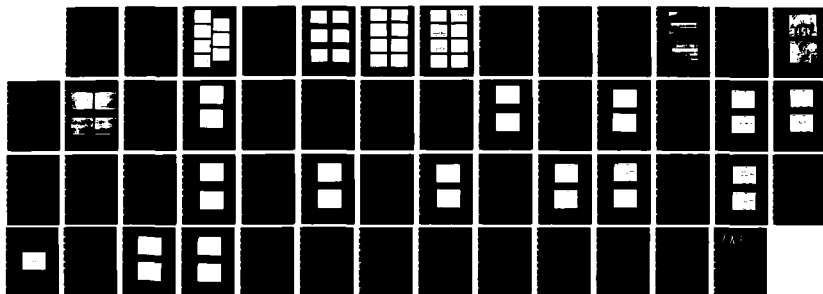
AD-A177 448

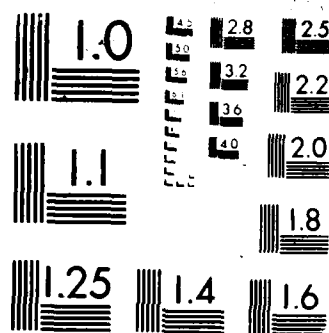
MULTIPLE COUPLED WAVEGUIDE LASER ARRAY(U) SCHAFER (W J) 2/2
ASSOCIATES INC CHELMSFORD MA D G VOUMANS 85 NOV 86
WJSA-FR-86-014 AFWAL-TR-86-2053 F33615-84-C-2445

UNCLASSIFIED

F/G 20/5

NL





MICROCOPY RESOLUTION TEST CHART

1963-A

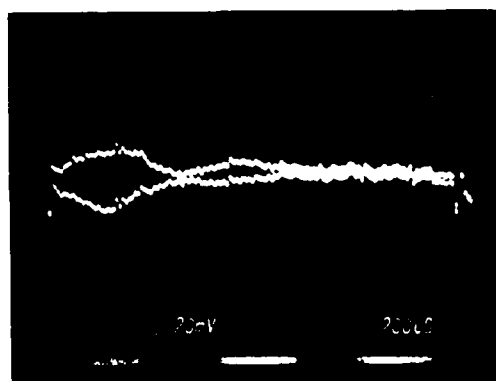
It also allowed more accurate measurement of the laser gas flow rates because the flowmeter calibration curves could be multiplied by $\sqrt{2}$ for operation at 15 PSIG instead of the correction factor for operation at low pressures. Optimum gas flow rates were remeasured when 1x7 device was resealed after leak checking.

Leak detection and sealing of the 1x7 array waveguide CO₂ laser device was achieved by coating the entire outside of the device with Torr seal and Kinney vacuum seal reducing the background pressure to about 1 Torr. The water cooling channels were cleared and dried and then filled with Kinney vacuum seal. Background pressures dropped to 0.2 Torr proving that diffusion through the porous BN plates caused a substantial vacuum leak. Fortunately when water was then flowed again through the cooling channels, background pressure remained at 0.6 Torr--a considerable improvement over the previous 2.8 Torr background pressure. Because of the porosity of BN, this material cannot be used in the outer walls of waveguide lasers, or any hard vacuum wall, and certainly not for cooling chamber walls. Considerable time and funding was lost trouble shooting this material.

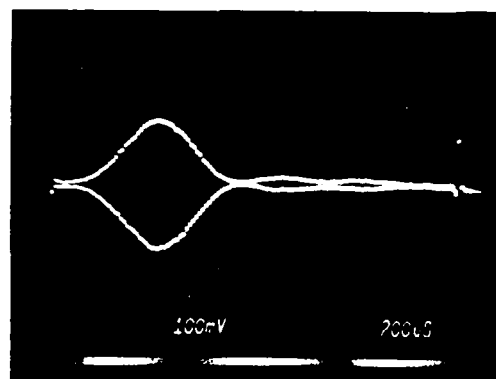
A 2 mm x 20 mm enhanced-Ag coated Si flat mirror and a 99% reflectivity ZnSe output coupler were then reinstalled on the 1x7 device. Lasing was achieved on all seven channels separately and on as many as channels 2, 3, 4, 5, 6, and 7, simultaneously. Typical output power for a single waveguide was 400 mW with only the 1% output coupling. Figure 31 shows the intensity distribution of each waveguide (sequentially) using the Spiricon pyroelectric array detector at a distance of 76 cm from the waveguide lasers' exit apertures. The distance between the intensity peaks corresponds to the 3 mm waveguide separation. The center to center spacing of the pyroelectric array elements is 0.2 mm.

It was found that when the central waveguide (#4) was aligned for maximum output, waveguides #1 and #7 were misaligned. Aligning the #1 channel would prevent the #7 channel from lasing. Thus, there is a

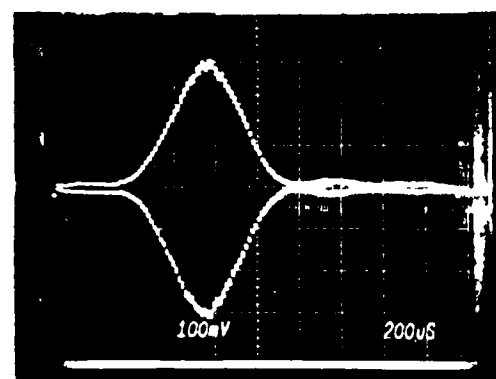
#1



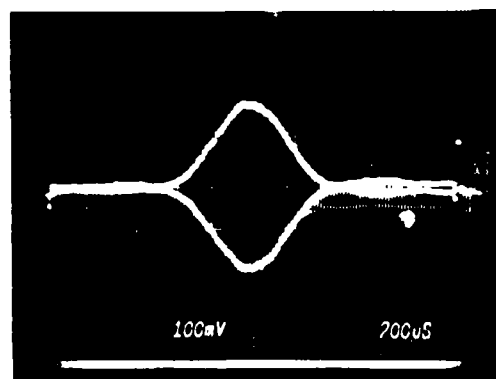
#2



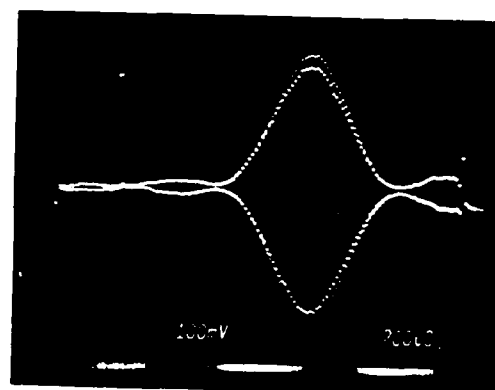
#3



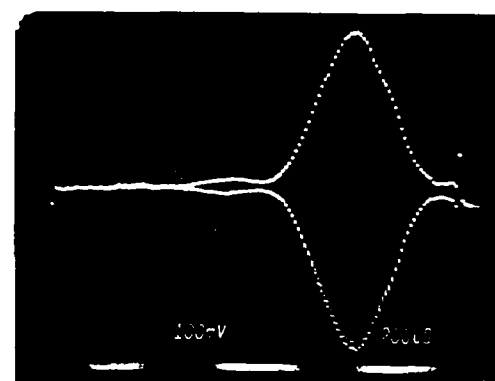
#4



#5



#6



#7

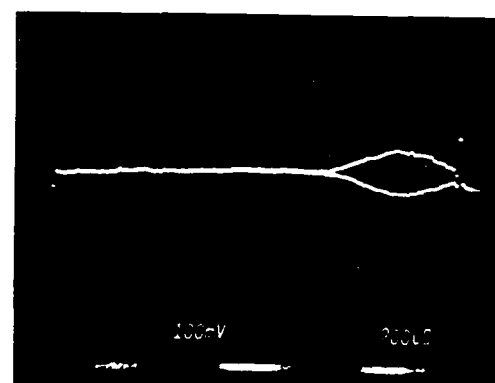


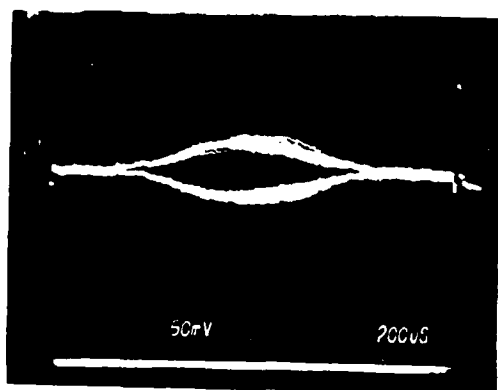
FIGURE 31. INTENSITY DISTRIBUTION OF CHANNELS 1 TO 7
AT A DISTANCE OF 76 cm

small "wedge angle" between waveguides. Also, the intensity distribution is more Gaussian and the secondary maxima are further from the center than predicted by the FFT of an HE_{11} mode in rectangular coordinates as reported in Section 5.

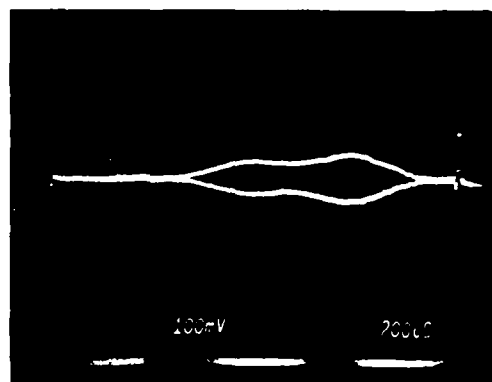
When several channels were run simultaneously, output power per channel decreased because small discharges around the ends of the interwaveguide windows between channels were started. This changed the channel discharge conditions resulting in suboptimal operation as well as producing hot gas at the channel ends which absorbed some $10.6\text{ }\mu\text{m}$ radiation. Figure 32 shows the far-field patterns of several waveguides lasing simultaneously. No interference fringes were observed indicating that the waveguides were operating on different transitions or that there was insufficient coupling to phase-lock the lasers.

In Figure 33 the pyroelectric array was moved as close as possible to the laser at a distance of 10 cm. The laser modes irradiated only about 10 pixels at this location, and mode overlap was very small. Moving the detector array only 4 cm further away to 14 cm, Figure 34 shows that at this distance the secondary maxima have diffracted outward and lie roughly on the maxima of the adjacent laser modes. When several waveguides are running, these fringes could falsely be confused with phase-locking. Interference fringes must be detected in the far-field, whereas Figure 34 is at about one Rayleigh range, $Z_R = \pi W_0^2 / \lambda = \pi (0.7\text{ (1 mm)})^2 / 10.6\text{ }\mu\text{m} = 14.5\text{ cm}$, for the equivalent TEM_{00} mode. Also, it appeared that at 14 cm the secondary maxima are larger relative to the central maximum than closer in (Figure 33) or further away (Figures 31 and 32).

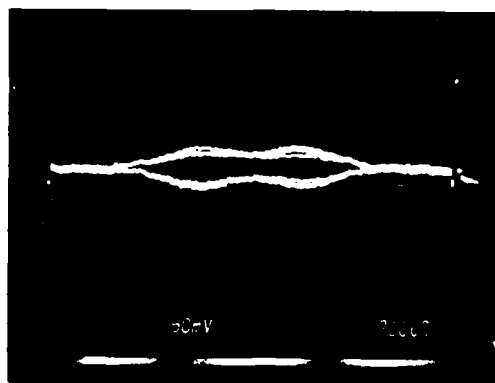
The optimum gas ratio was found to be 5.3:1.3:1::He:N₂:CO₂ at a total upstream pressure of 35 to 45 Torr. The gas flow rates at these optimum conditions were measured to be:



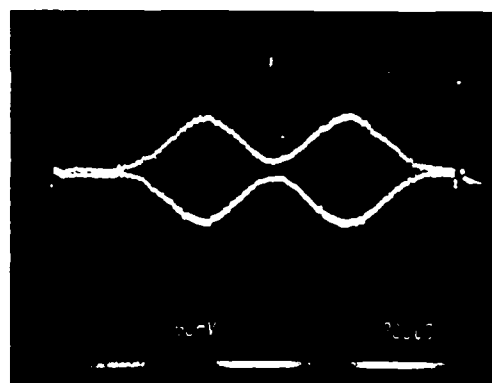
#3,4,5



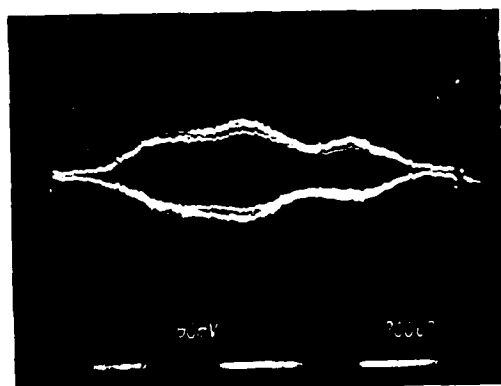
#4,6



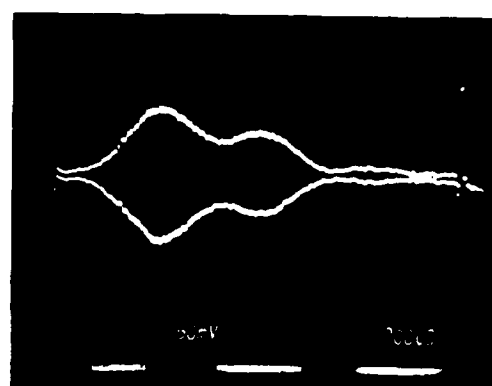
#3,5



#3,6

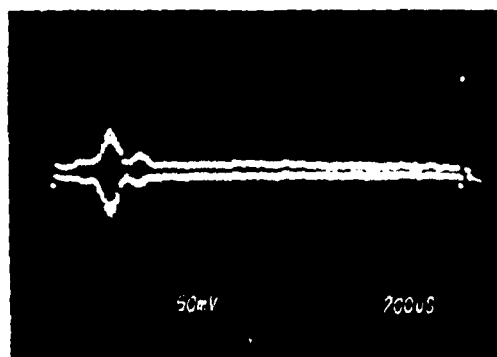


#2,4,6

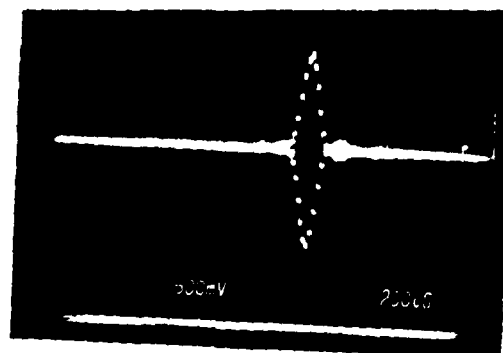


#2,4

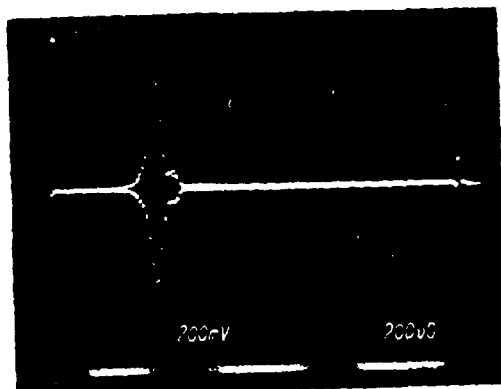
FIGURE 32. MULTICHANNEL LASING OUTPUT DISTRIBUTION AT
A DISTANCE OF 76 cm



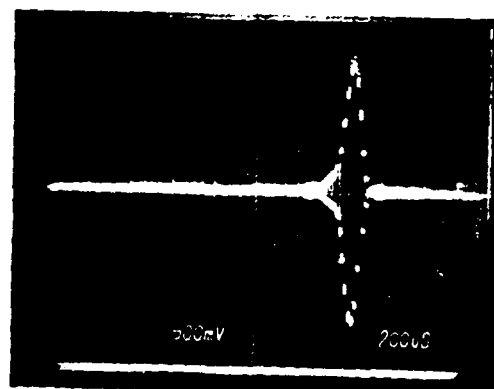
#1



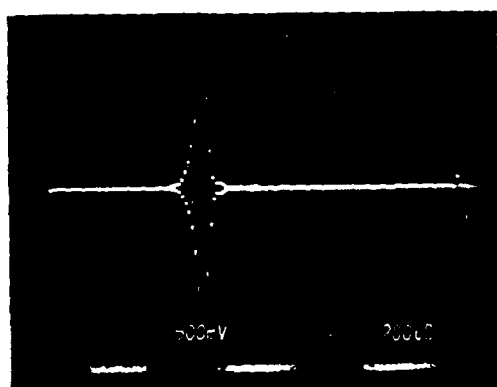
#5



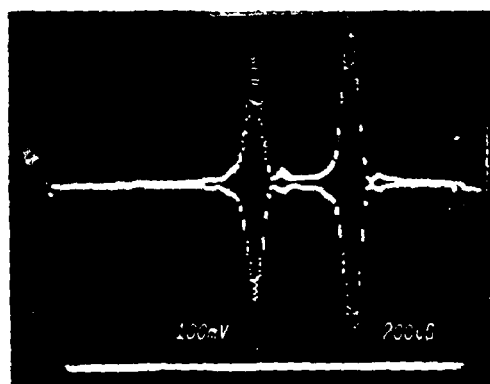
#2



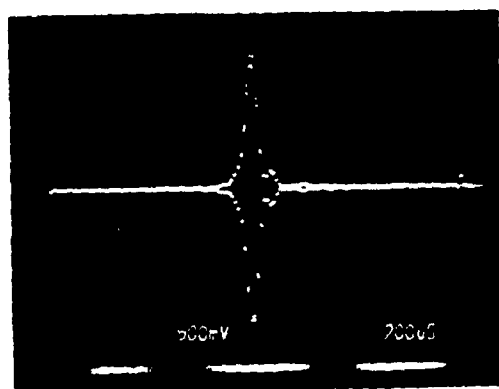
#6



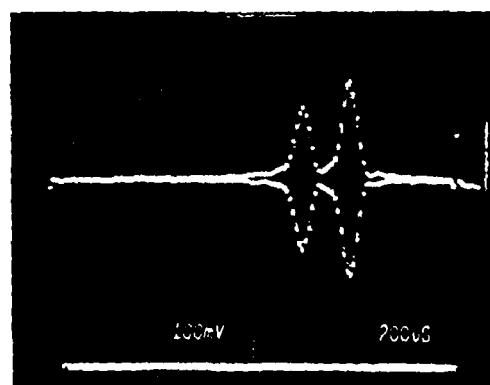
#3



#4,6

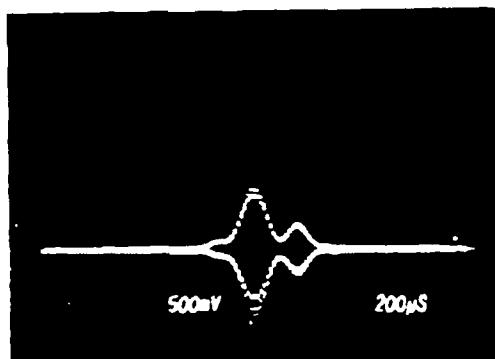


#7

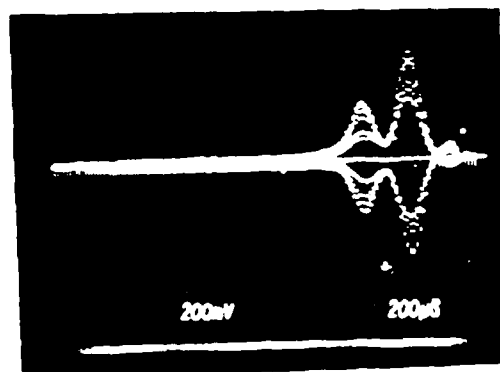


#5,6

FIGURE 13. REPRESENTATIVE MODE SHAPES AT 10 cm DISTANCE



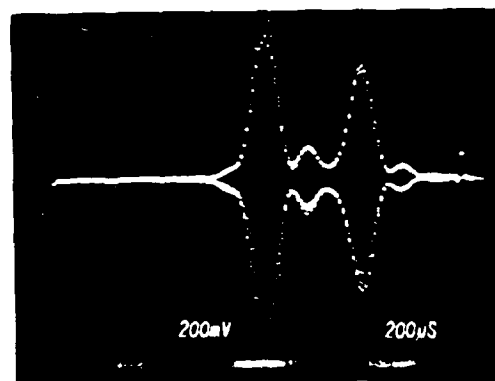
#4



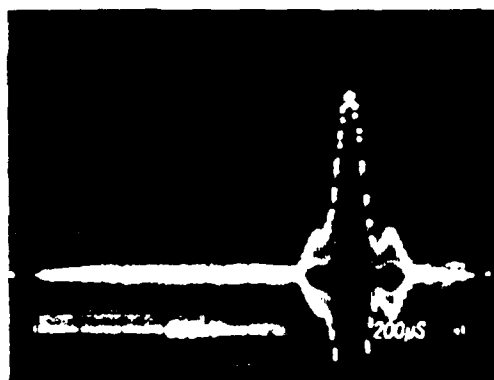
#6,7



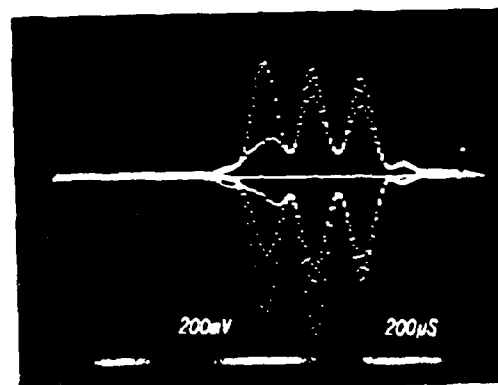
#5



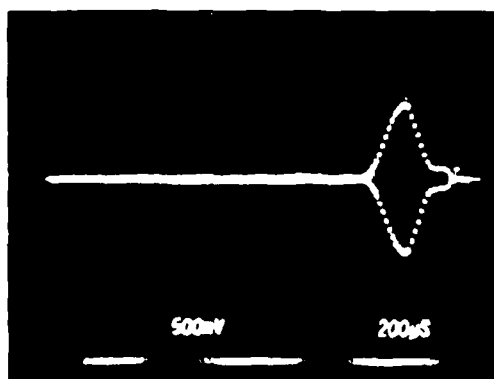
#4,6



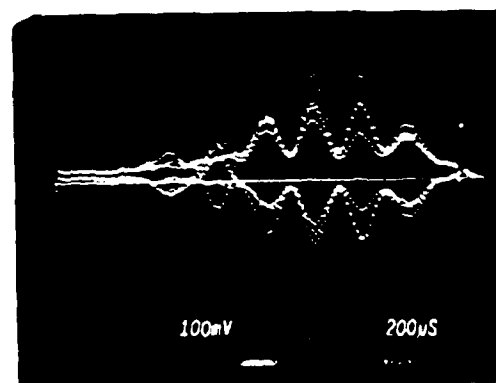
#6



#4,5,6



#7



#4,5,6,7

FIGURE 21. REPRESENTATIVE MODE SHAPES AT 14 M DISTANCE

He - 1.13 μ /min
N₂ - 0.28 μ /min
CO₂ - 0.21 μ /min or 4.8 fills/sec

1.6 μ /min or 4.8 fills/sec

Velocity = 95 cm/sec (= Mach 0.002)

When Xe was introduced, an additional 10% laser power was obtained at an optimum gas mixture of about 4:1:1:1::He:N₂:CO₂:Xe at an upstream pressure of 60 Torr. With this surprisingly large amount of Xe, plasma oscillations were more prevalent than without Xe. Gas flow rates were measured to be:

He - 1.13 μ /min
N₂ - 0.31 μ /min
CO₂ - 0.28 μ /min
Xe - 0.41 μ /min

2.1 μ /min or 6.3 fills/sec

Velocity = 125 cm/sec (= Mach 0.003)

Discharge current versus anode to cathode voltage (V_{gas} + cathode fall + anode rise) was measured and is plotted in Figure 35. The negative resistance regime is again evidenced as in the test channel. This was not seen when the gas was contaminated. Optimum discharge current was found to be 5 mA to 7 mA per waveguide. Most of the data were taken at 4 mA to avoid overheating and mirror damage.

The laser mode polarization was measured and again found to be at least 200:1 parallel to the ZnSe interwaveguide windows as was found in the previous²⁹ 1x2 device.

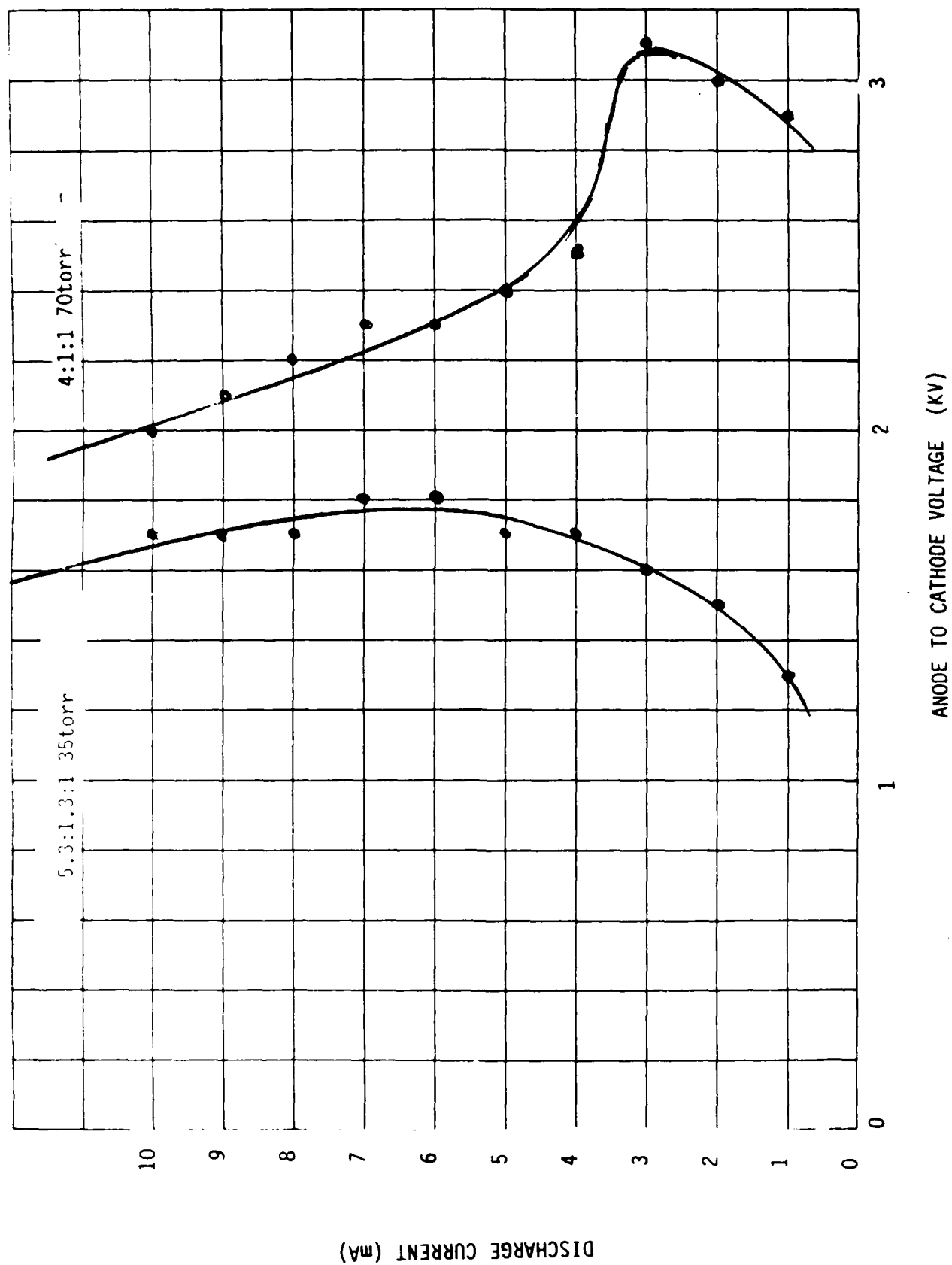


FIGURE 35 DISCHARGE CURRENT VS VOLTAGE

The 1x7 array waveguide CO₂ laser device was retested using the infrared reflection grating as the total reflector. First, the array was aligned using a 1% output coupler and the 2 mm x 20 mm enhanced silver-coated-silicon total reflector. About 400 mW per waveguide (separately) was measured as reported above. The grating was then installed in place of the 2 x 20-mm total reflector, everything else remaining the same. Unfortunately, lasing could not be achieved using the grating. It appeared that the grating was misaligned by approximately 2° about an axis perpendicular to the plane of the seven waveguides. Compression of the O-ring against the grating did not allow enough rotation to compensate for this machining error.

The next series of tests would have been to replace the grating with an anti-reflection (AR)-coated window and mount the grating externally using a mirror mount for correct alignment. Also, a lens in front of the grating or simply an external spherical copper mirror could have been tried. Due to time and funding constraints, however, the 1x7 array was put away for future testing at the end of the program if time allowed, and attention was given to the 2x3 device.

6.2 Two-by-Three Array Device

While the 1x7 array device was undergoing testing, the 2x3 array device was being fabricated. Each half of the 2x3 device was machined from a solid block of Macor as shown in Figure 36a. On the inner surface is an O-ring groove, a notch for the large ZnSe windows, and two grooves in the waveguide channel floor for the small ZnSe windows. Copper electrode pins enter the waveguides through three small holes at each end (cathodes) and the middle (anodes). Gas flow ports are cross-drilled through the body, and the electrode holes are enlarged so that gas flows around each cathode and anode. The laser gas mixture flows in around the central anodes and out around the cathodes at each end. The channels of the 2x3 device were made 1.6 mm square to help confine the discharge compared to the 2 mm square channels of the 1x7 device. The 2x3 device is also 20 cm long.



FIGURE 36a. ONE HALF OF MACOR 2 x 3 WAVEGUIDE DEVICE

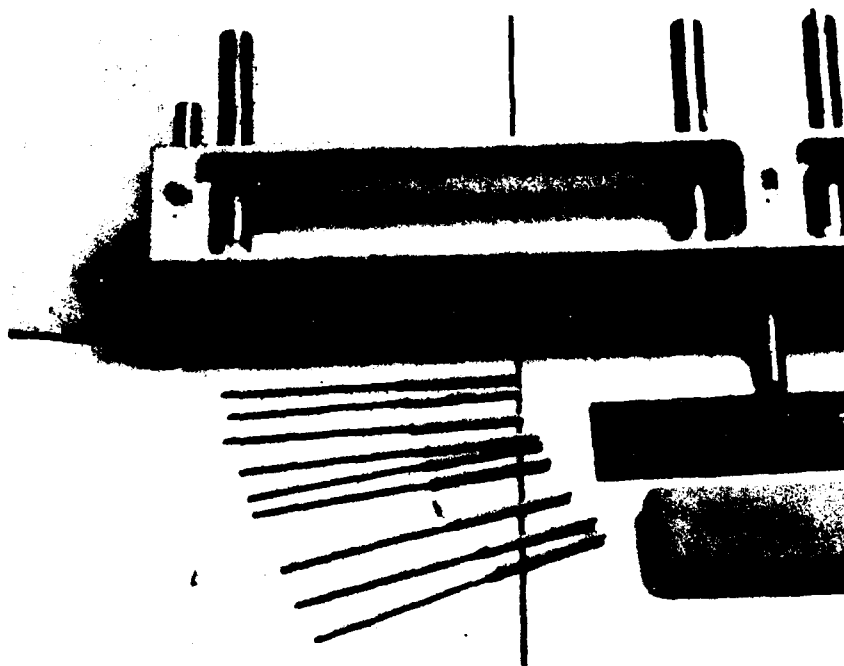


FIGURE 36b. CLOSEUP OF COOLING CHANNELS, ELECTRODE INSERTION HOLES, AND ELECTRODE PINS

Water cooling channels in the outside of the Macor block are shown in Figure 36b. The electrode pins are covered by Al_2O_3 sleeves and slide into the electrode insertion holes so that they are flush with the waveguide channel wall for a minimum scattering loss. The electrodes, gas flow chambers, and water cooling channel covers are sealed with E&C 286 epoxy far from the heat of the discharge.

Milling of each half took about 40 man-hours, and, since the ceramic was very brittle, several body halves cracked during milling. Many hours were spent determining feed rates, cutting depth, and milling tool rotation rates for properly machining this Macor ceramic.

A set of Al_2O_3 plates (4x25x1 mm and 10x25x1 mm) was ordered from Wakefield Precision Optics to initially replace the ZnSe interwaveguide windows in the 2x3 device. It was felt that characterizing the laser using standard Al_2O_3 surfaces and SiO_2 (Macor) surfaces would provide a reference point to compare with the mode shapes and powers measured when the ZnSe plates were installed.

The 2x3 array Macor device vacuum and gas flow manifolds were completed and leak checked individually. The empty Macor body was then sealed and found to be leak free down to the 30 mTorr roughing pump vacuum. The polished Al_2O_3 interwaveguide plates were installed, but, when the array was pumped down, a hair-line crack developed between the waveguides and one water cooling channel. Fortunately, the leak was sealed using Kinney vacuum seal inside the water channel on the second attempt.

The 2x3 device was then transported to the optical table and the 1x7 device was removed for storage. The vacuum lines, gas flow system, and power supply lines were then connected. Figure 37 shows a side view and an end view of the system after installation.

A flat ZnSe total reflector and 5% output coupler were next installed on the array. A maximum output power of 3 W was measured



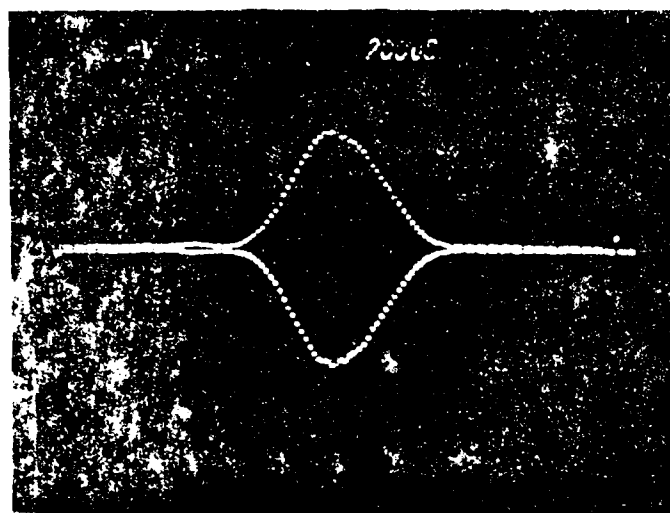
FIGURE 1. SIDE VIEW AND END VIEW OF 2 X 4 ARRAY DEVICE
INSTALLED WITH VACUUM, GAS FLOW, AND POWER
SUPPLY LINES.

from one waveguide with slightly lower powers on the other channels. A 10% output coupler was tried next and a maximum of 8 W was measured on one channel. Three other channels showed powers of 6 to 7 W, and two channels were obscured by blackening of the output coupler and a small chip of Macor. The 8 W output power measurement corresponds to 0.4 W/cm of discharge length. This is very good efficiency for dc discharge excited waveguide CO₂ lasers. Next a 15% output coupling was used, and a maximum of 2 W was measured on four channels, one channel at 1 W, and one not lasing.

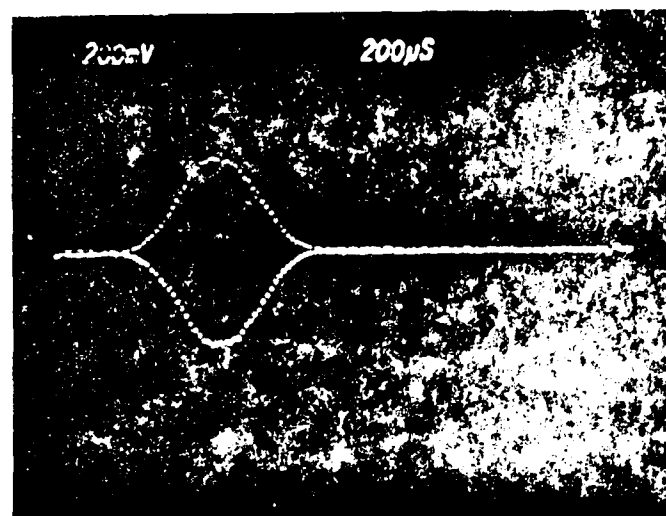
Some representative mode shapes using the Spiricon pyroelectric array detector are shown in Figure 38. Nearly Gaussian far-field patterns are shown. The linear pyroelectric detector array can be oriented either vertically or horizontally as indicated below the photographs. The numbering of the channels is shown in Figure 39 for defining the waveguide channel location in the following tests.

Next, simultaneous lasing of different waveguide channels was achieved resulting in the mode shapes shown in Figure 40. Since Al₂O₃ plates and not ZnSe plates separated the waveguides, no phase-locking was expected or observed. (It had been suggested previously, however, that phase-locking could occur due to the cross coupling at the mirror surfaces. Figure 40 demonstrates that this is not the case.) Plasma oscillations due to discharge crosstalk cause the intensity variations shown in the photographs.

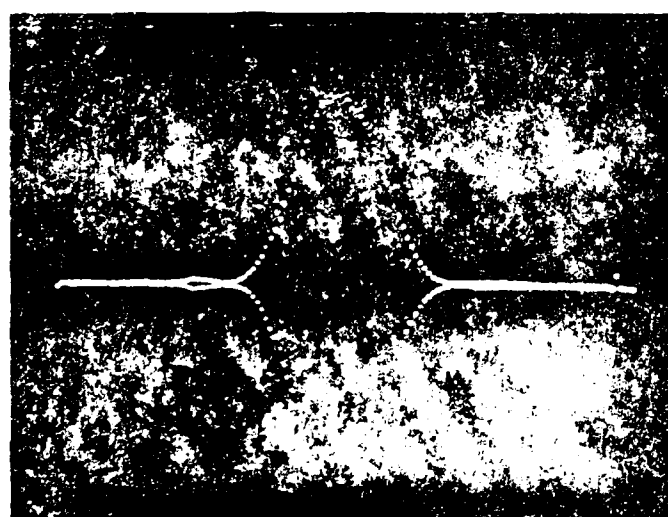
The optimum gas ratio was found to be about 10:1:1::He:N₂:CO₂ at 30 Torr total pressure although there was little variation down to a 6:2:1 mixture at 52 Torr upstream pressure. The corresponding gas flows were measured to be:



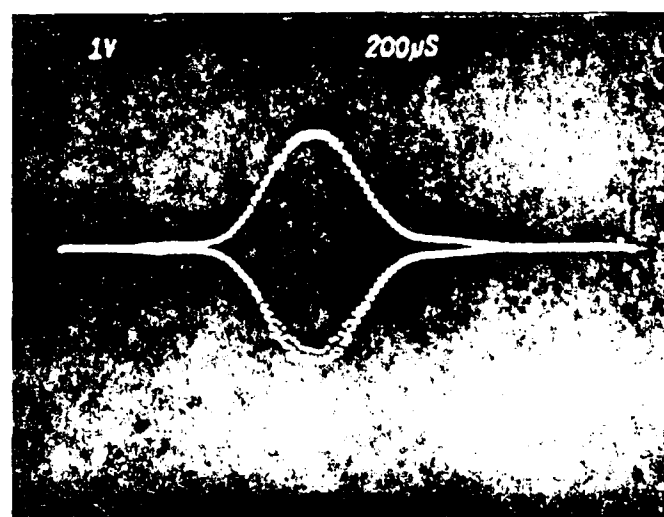
Channel 4, 5% O.C.
 $z = 57$ cm
 Vertical Detector



Channel 6, 5% O.C.
 $z = 57$ cm
 Vertical Detector



Channel 4, 5% O.C.
 $z = 57$ cm
 Vertical Detector



Channel 6, 5% O.C.
 $z = 57$ cm
 Vertical Detector

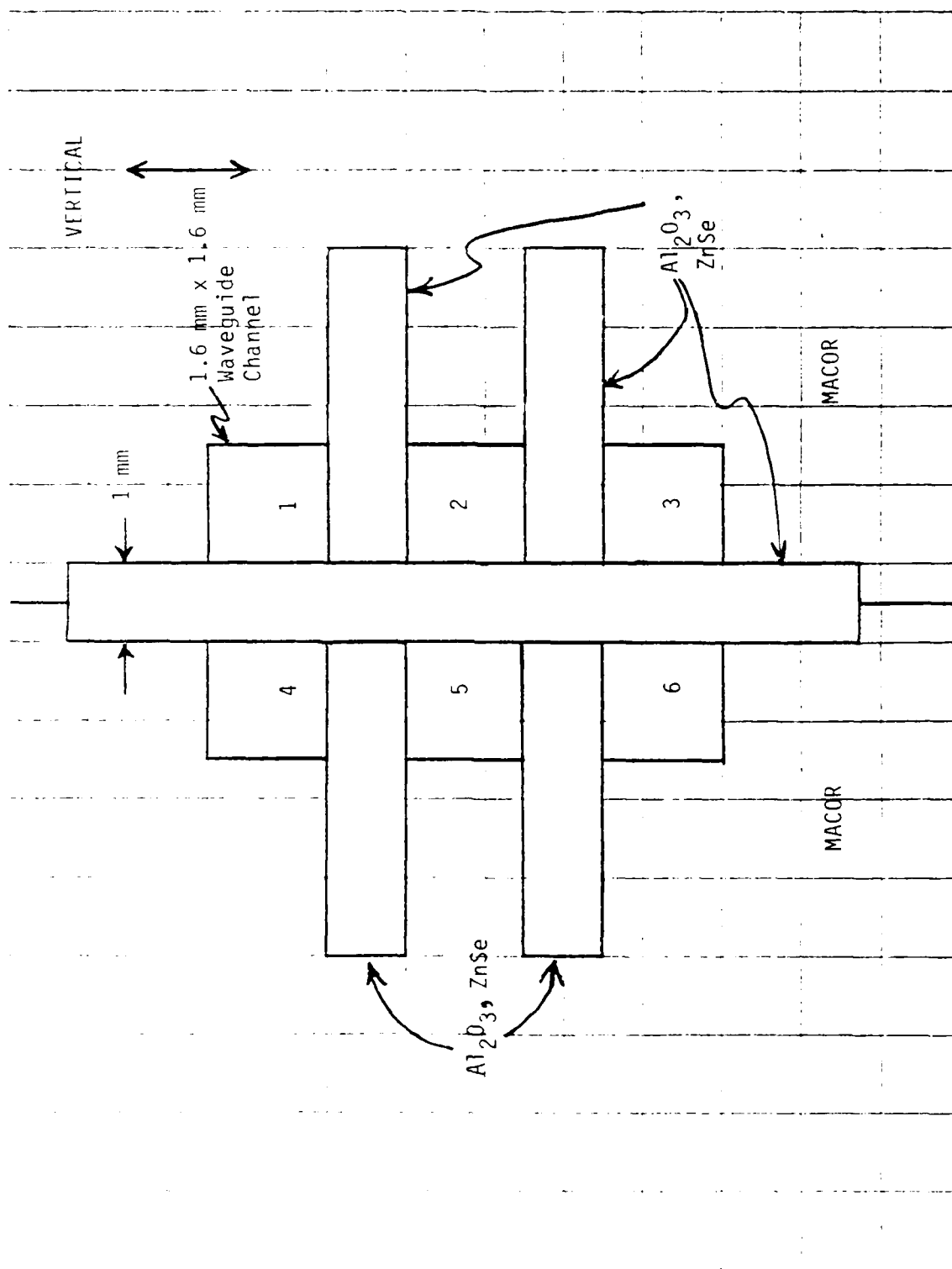
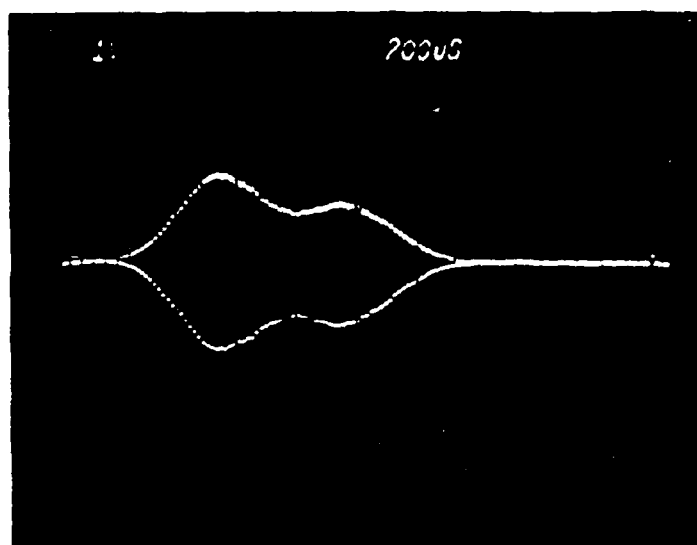
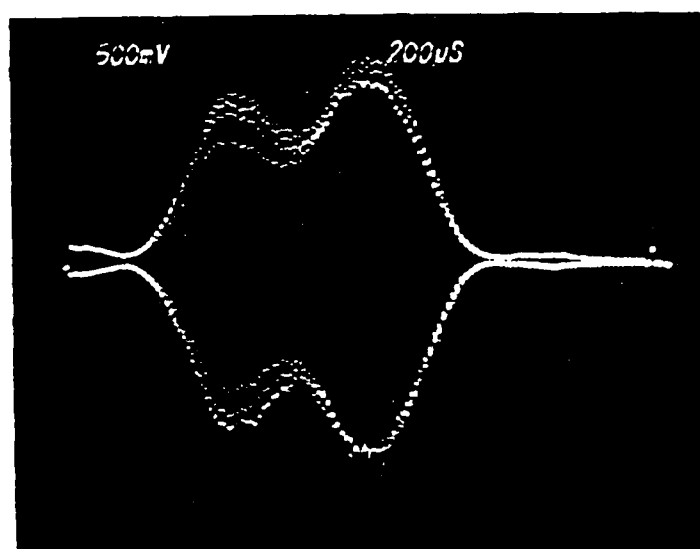


FIGURE 39. 2 x 3 DEVICE CHANNEL NUMBERING, OUTPUT END



Channels 4, 5, 6 - 10% O.C., $z = 67$ cm, Vertical Detector



Channels 4 and 6 - 15% O.C., $z = 67$ cm, Vertical Detector

FIGURE 40. FAR-FIELD PATTERNS DUE TO SIMULTANEOUS CHANNEL LASING, Al_2O_3 SEPARATED 2×3 DEVICE

He - 2.8 μ /min

N₂ - 0.28 μ /min

CO₂ - 0.28 μ /min

3.4 μ /min or 19 fills/sec

Velocity = 369 cm/sec (= Mach 0.009)

A plot of discharge current versus voltage at the 10:1:1 80 Torr mixture is shown in Figure 41. The negative resistance region is again evidenced. Optimum discharge current was measured to be about 4 mA per channel in good agreement with waveguide laser theory.

Using the 8 W output power at 10% output coupling data point, a first order Rigrod analysis can be applied. The output power from a homogeneously broadened laser is approximately given by equation 9.

$$P_{out} = \frac{I_s}{2} A t \left[\frac{2g_0 l}{t + L} - 1 \right] \quad (132)$$

where

I_s = 3,000 w/cm² (80 Torr) saturation intensity

A = 2a mm x 2a mm area x $\pi/4$ (~ mode area) a = 1.59 mm/2

t = transmission of output coupler

g_0 = small signal gain

l = discharge length

L = round trip losses other than output transmission

$\cong 2 \times$ (waveguide loss) + (reflector loss) + $2 \times$ (coupling loss)

The optimum output coupling determined by differentiating equation (132) is given by

$$t_{opt} = (2g_0 l L)^{1/2} - L \quad (133)$$

once g_0 and round trip loss, L , are known.

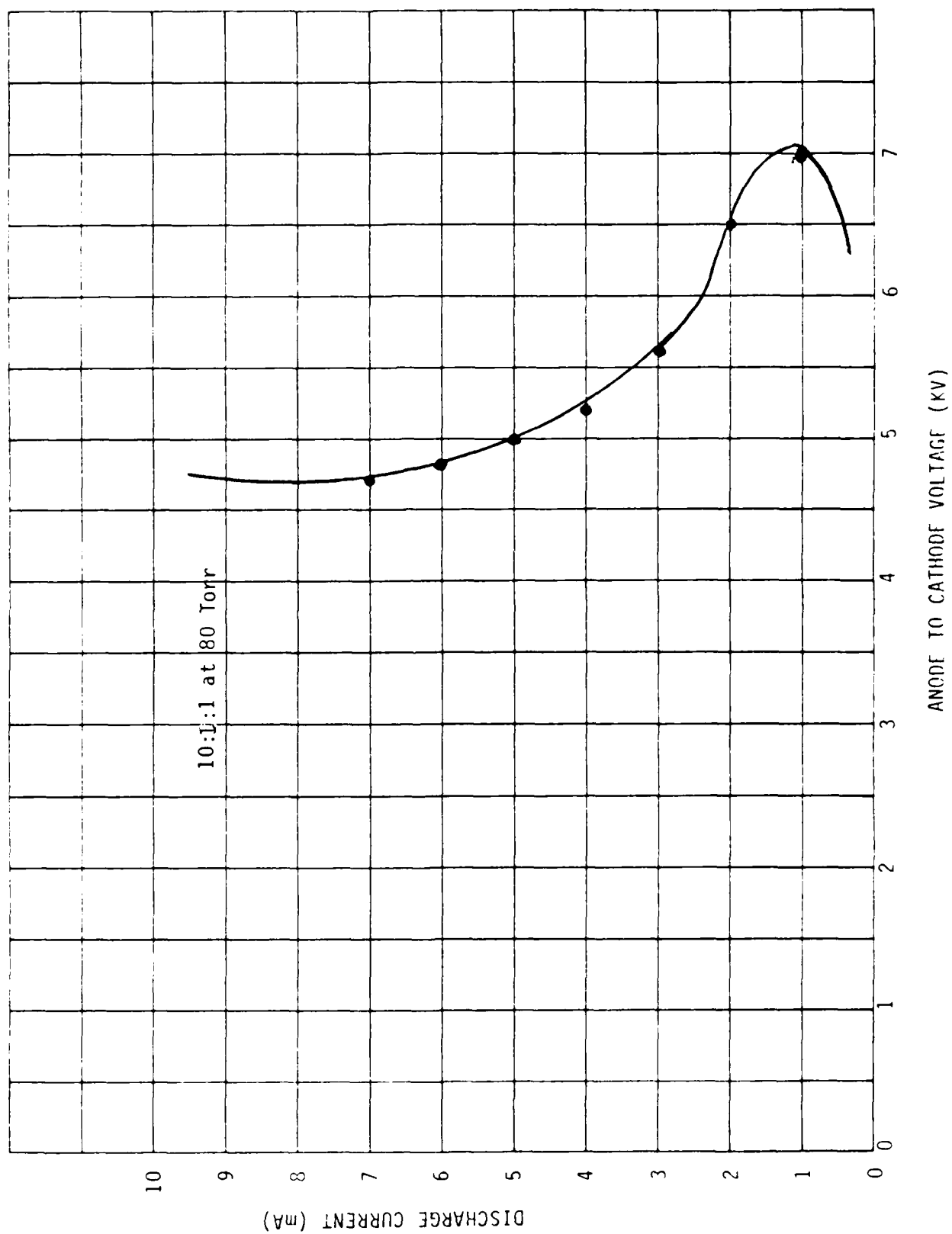


FIGURE 41. DISCHARGE CURRENT VS VOLTAGE 2 x 3 DEVICE

The locus of points of all values of L and q_0 giving 8 W of output power (single waveguide) is drawn in Figure 42. Similarly, all values of L and q_0 having an optimum output coupler transmission of 10% are plotted. The two curves intersect at $q_0 = 1.15\%/cm$ and round trip loss of 3.8%. This is in good agreement with expected values.

The ZnSe flat total reflector was removed next and replaced with a flat AR/AR coated ZnSe window. A one-inch-diameter, 9-inch radius-of-curvature concave copper mirror was then placed 9 inches from the waveguide apertures forming a class two resonator as described in Section 2.2. By translating the mirror vertex to the optical axis of each waveguide sequentially, output powers of 4 through 6 W were measured on all the six waveguides. Figure 43 shows representative mode shapes for horizontal and vertical pyroelectric array orientation. The polarization of all six waveguides was found to be in the vertical direction as defined by Figure 39. Because of the wall symmetry in waveguides 1, 3, 4, and 6 resulting in no preferred polarization, it was thought that scattering off of the flush electrodes and gas flow holes produced the TE polarized modes (E-field parallel to the electrode surfaces) in the vertical direction.

The copper mirror was then translated to half-way between adjacent waveguide channels. Folded resonator modes were observed at the output coupler: the light propagates down one waveguide, reflects off the spherical copper mirror at a small angle and then propagates back through the adjacent waveguide. The folded resonator has an output coupler at each end. The geometry of folded resonator modes is shown in Figure 44. Far-field intensity distributions are presented in Figure 45. In Figure 45a) is the output from channels 2 and 5 with the detector horizontal. The interference fringes are clearly visible. By translating the copper mirror in or out, the maxima can be changed to minima and visaversa. This is, of course, due to the half-integer wavelength separation between the output mirrors at the Fabry-Perot resonance condition. Data on this phenomena will be shown shortly.

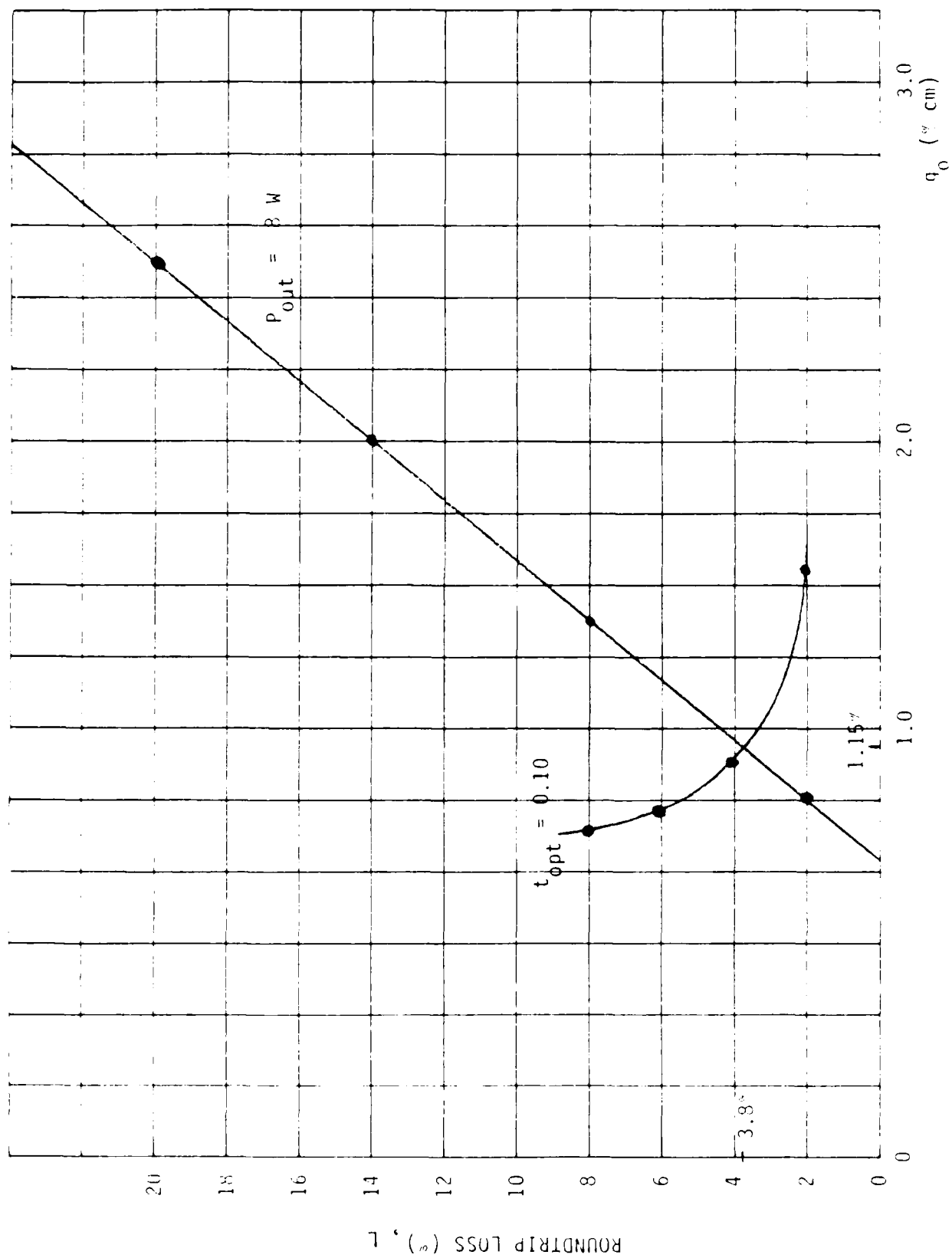
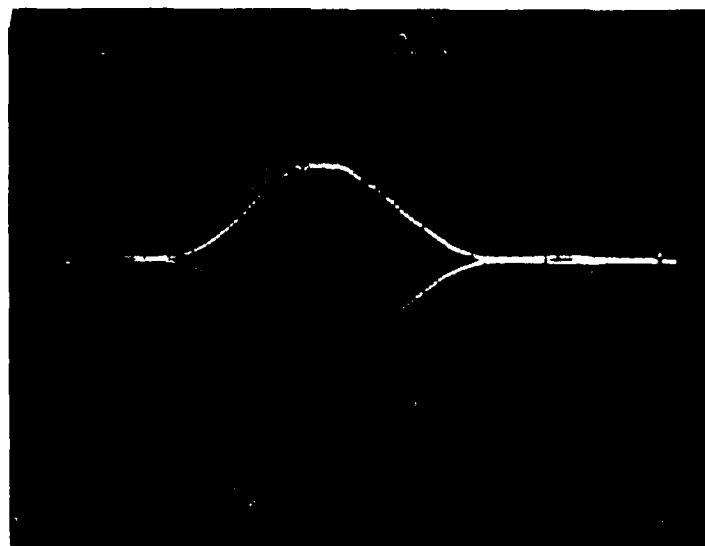
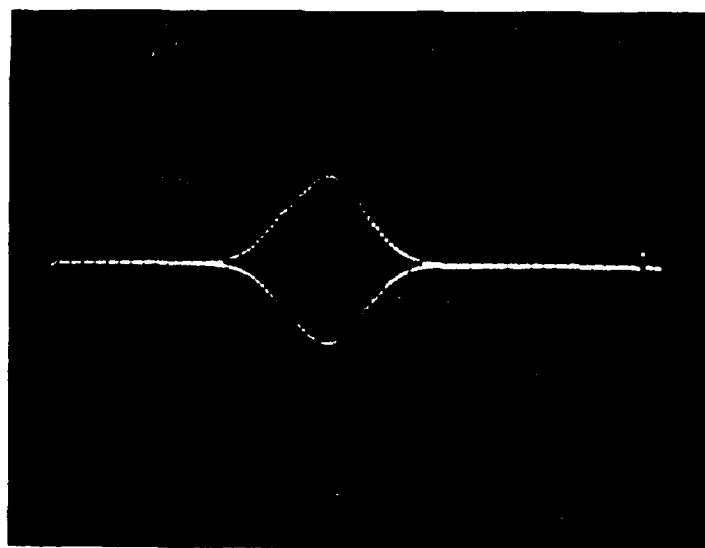


FIGURE 42. RIGROD ANALYSIS 2 x 3 DEVICE, Al_2O_3 PLATES



a) Channel #5 Vertical Detector, $z = 77$ cm



b) Channel #5 Horizontal Detector, $z = 42$ cm

FIGURE 43. MODE SHAPES WITH SPHERICAL COPPER MIRROR/90% REFLECTOR,
INDIVIDUAL WAVEGUIDES SEPARATED BY Al_2O_3 PLATES

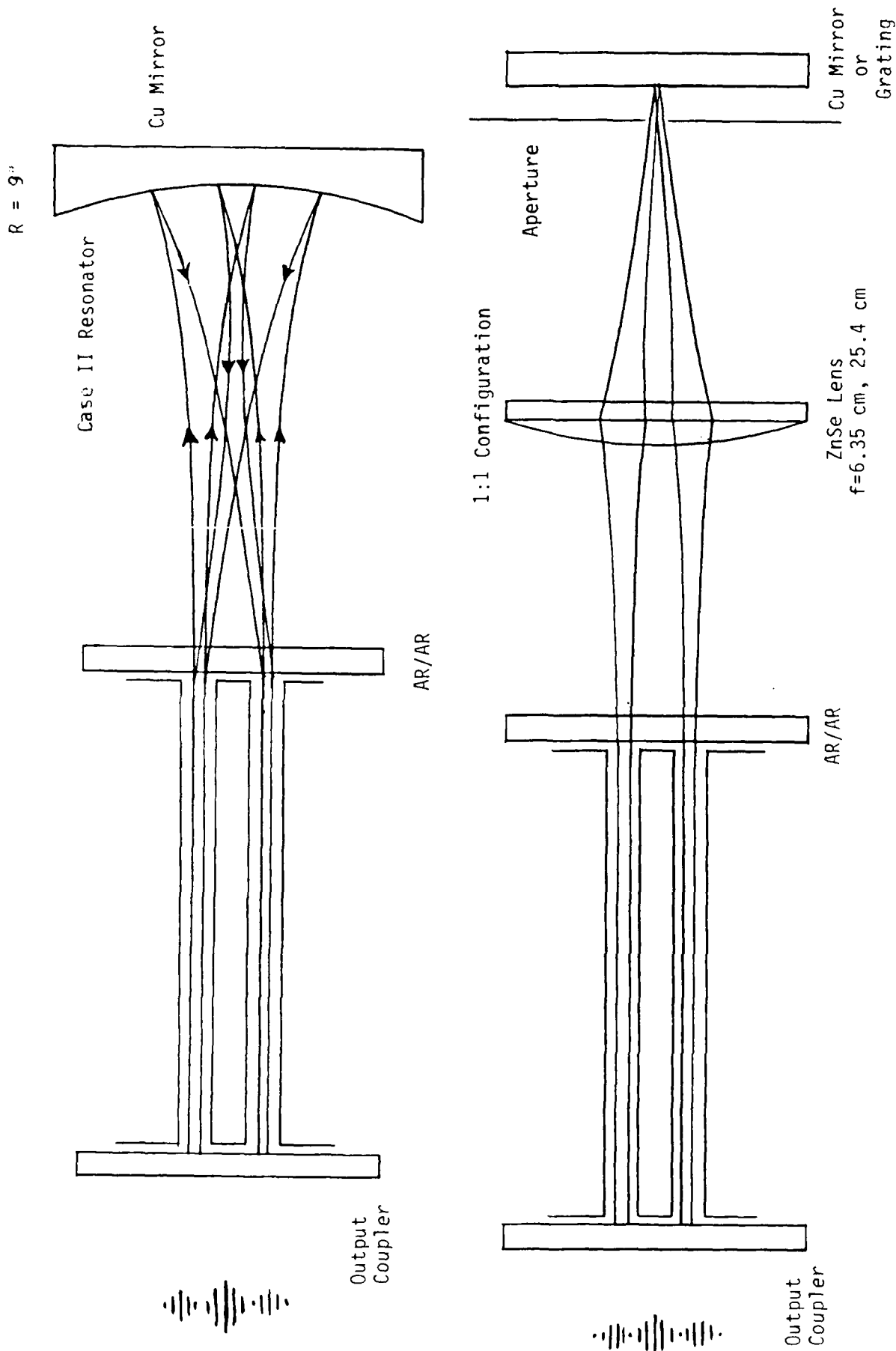
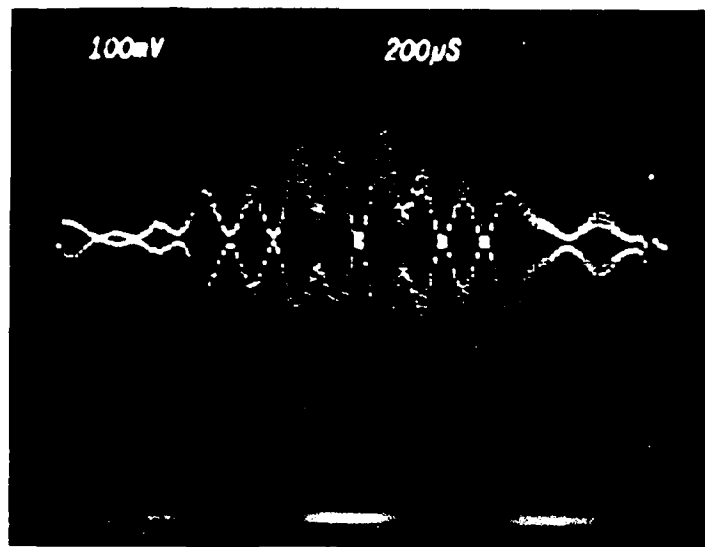
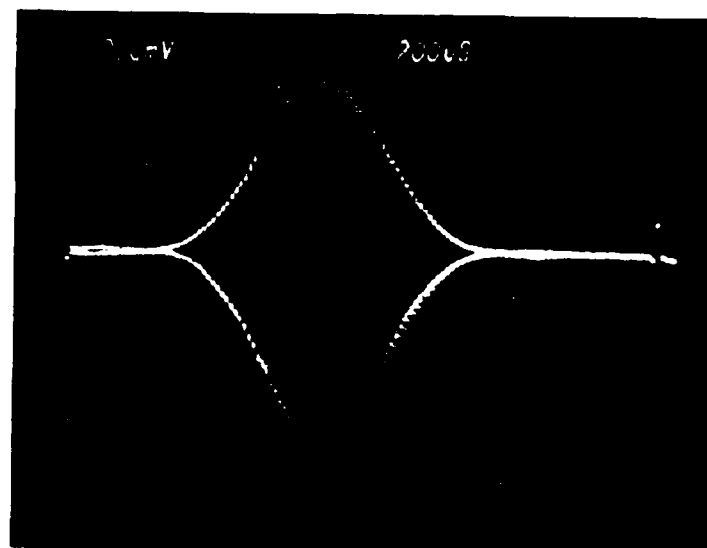


FIGURE 44. FOLDED CAVITY RESONATOR MODE GEOMETRIES



a) Detector Array Horizontal, $z = 56$ cm



b) Detector Array Vertical, $z = 77$ cm

FIGURE 45. FOLDED RESONATOR MODE OF CHANNELS #2 AND #5
SEPARATED BY Al_2O_3 PLATES, 9" R.C. COPPER MIRROR

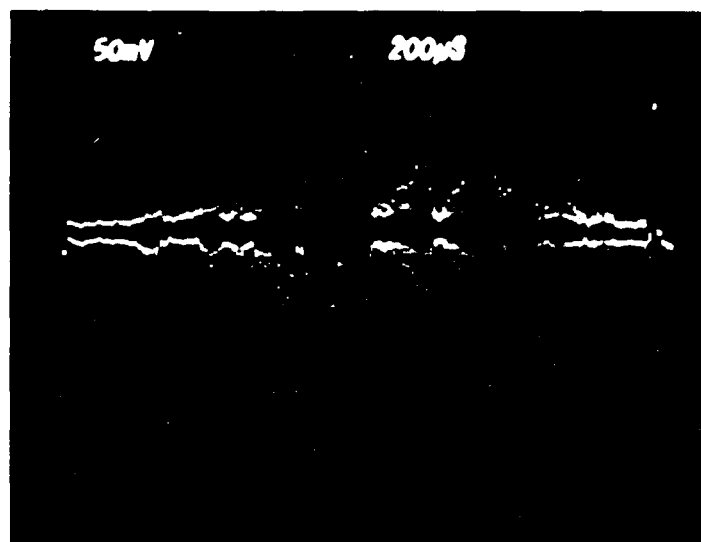
Figure 45b) has the detector array vertical showing the Gaussian mode distribution without interference fringes.

Diagonal-folded resonator modes were observed when the spherical mirror was placed half-way between diagonally separated waveguides. That is, that waveguides #1 and #5 could form a single resonator. Because of the high coupling losses, output powers were down to about 200 mW. Interference fringes were observed in both the horizontal and vertical directions. Figure 46 shows a diagonal folded mode energy distribution in both axes. When two diagonal folded resonators were lasing, Channels 1 + 5 and 2 + 4 for example, similar interference patterns were observed. Increased plasma oscillations because of the operation of four channels further reduced the power.

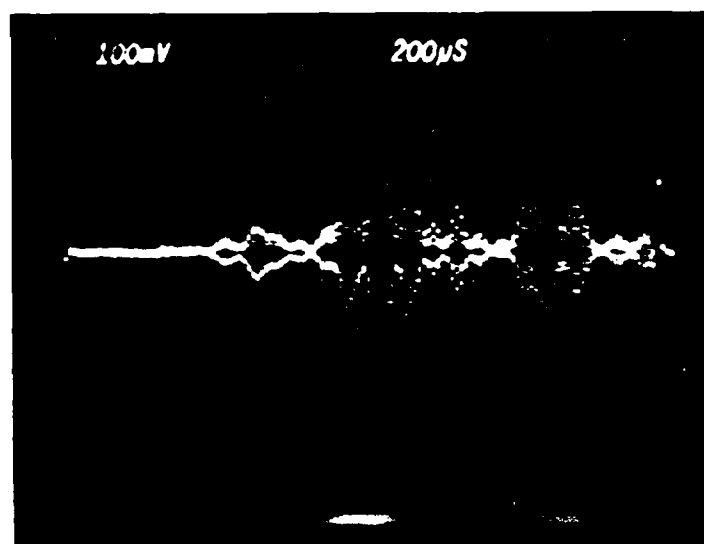
The spherical copper mirror was then aligned to a single waveguide, and the Gaussian mode was focussed into a Laser Engineering CO₂ spectrum analyzer. As the copper mirror was translated along the optical axis, the 10 μ m lines of P12, 14, 16, 18, 20, and 22 were observed to lase. The P20 line was the strongest, as expected.

Next the reflection grating was placed as closely as possible to the AR coated window. The distance from the center of the array to the grating was 4.1 cm at this point. The output powers from channels #1 and #4 closest to the grating were measured to be 1.5 W each. Channels #2 and #5 produced about 1.4 W each, and channels #3 and #6 furthest from the grating produced 600 mW each. Lasing was achieved with the grating as far as 11.4 cm from the exit apertures. Figure 47 shows some typical mode patterns for this resonator configuration.

Next a 6.35 cm focal length ZnSe lens was placed between the waveguide exit aperture and the grating. Initially the lens was used in the 2:2 position (as for geometrical optics) as this was easier to implement. No lasing was observed. The lens and the grating were then placed in the 1:1 location as for Gaussian mode applications. Lasing was achieved with about 1 W of power measured on each waveguide

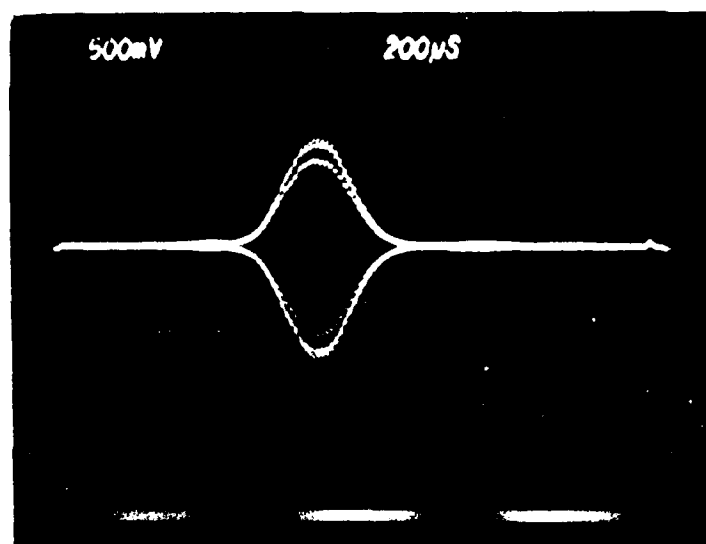


a) Detector Array Horizontal, $z = 36$ cm

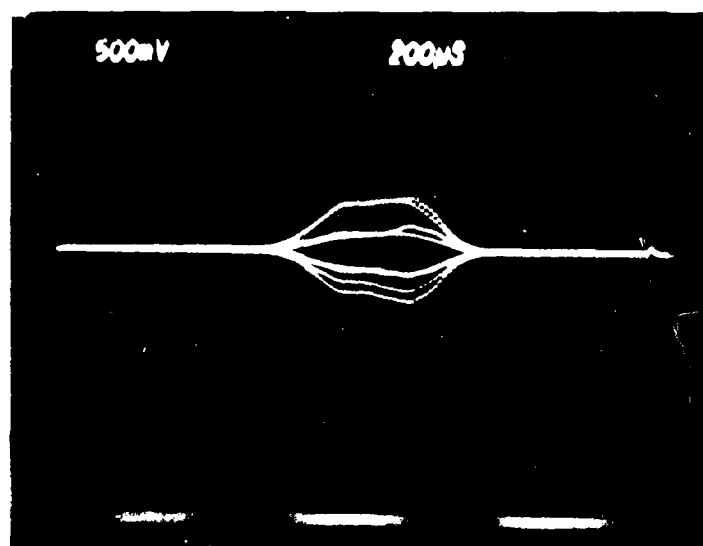


b) Detector Array Vertical, $z = 36$ cm

FIGURE 46. DIAGONAL-FOLDED RESONATOR MODE OF CHANNELS #1 AND #5
SEPARATED BY Al_2O_3 PLATES, 9" P.C. COPPER MIRROR



a) Channel #6 Vertical Detector, $z = 51$ cm



b) Channels #2 and #4 Detector Horizontal, $z = 46$ cm

FIGURE 47. REFLECTION GRATING MODE STRUCTURES, GRATING AT 4.1 cm.
CHANNELS SEPARATED BY Al_2O_3

separately. Gaussian modes were observed when the lens and grating were aligned for one waveguide, and folded cavity modes were found when the lens and grating were aligned half-way between channels.

In the focussing of Gaussian modes, it is well documented that they do not obey geometrical optics but have their own set of equivalent equations³⁰. The magnification is given by

$$m = \frac{W'_0}{W_0} = \frac{1}{((1-S/f)^2 + (Z_R/f)^2)^{1/2}} \quad (133)$$

where S is the distance of beam waist W_0 from the lens. Magnification is a maximum at

$$\frac{dm}{ds} = 0 \Rightarrow S = f \quad (1:1 \text{ position}) \quad (134)$$

and at this point

$$m = f/Z_R \quad (135)$$

where $Z_R = \pi w_0^2/\lambda$. The magnification for the 6.35-cm focal length lens is thus 6.25 cm/9.29 cm or 0.68. At the lens focal plane there is a beam waist, W'_0 , or plane wave, and the light reflects back to the lens exactly along the path of the incident mode. Other conjugate positions are, of course, possible with reduced magnification.

By slowly rotating the grating and observing the output of a single channel on a CO_2 spectrum analyzer, lasing occurred on the following transitions:

9.20 μm R(34) > 9.28 μm R(18)

9.54 μm P(18) > 9.66 μm P(32)

10.17 μm R(32) > 10.26 μm R(18)

10.57 μm P(18) > 10.63 μm P(24)

At this point it was felt that enough had been learned about mode shapes without interwaveguide coupling so that a difference would be detectable in the mode shapes with interwaveguide coupling. Consequently, the ZnSe interwaveguide windows were installed.

The 2x3 array device was disassembled and the Al_2O_3 interwaveguide plates were removed. The plates were found to have a brown coloration that was believed to be from the copper of the electrode pins. The tan discoloration was not dissolvable in acetone and was infused into the Al_2O_3 material.

The ZnSe plates were installed into their slots, and the device was reassembled and leak-checked. A vacuum leak developed again inside one of the water cooling channels and was sealed with Kinney vacuum seal for the second time. The following morning it was found that this hairline crack had opened up, and channels #4 and #5 were plugged with Kinney vacuum seal. Consequently, the Macor body had to be opened up once more.

Kinney vacuum seal was peeled out of channels #4 and #5, and a dark hairline crack was visible at the bottom of the ZnSe plate groove. It is believed that the brittleness of the Macor ceramic that caused the crack to develop when the body was assembled and then reassembled. The only possible way to seal the vacuum leak was to pump on the water-cooling channel on the other side of the crack. Thus, one of the four water cooling channels became inoperational and care would have to be taken to avoid overheating this part of the structure.

The 2x3 device was reassembled, and a 95% reflectivity output coupler and the AR/AR window were installed. The 9 inch radius of curvature copper mirror was placed 9 inches from the six waveguide apertures forming a case II resonator for the first series of tests. The concave mirror was aligned to channels #4 and #1 and about 300 mW from either channel (separately) was measured. This is a considerable drop from the six watts with 10% outcoupling and three watts with 5% outcoupling that was measured with the Al_2O_3 plates installed. The reduced output power can only be due to the increased distributed loss produced by the ZnSe walls and the leaked radiation compared to the Al_2O_3 walls.

The polarization of each waveguide was sequentially measured and found to be:

#4 horizontal	#1 vertical
#5 50/50	#2 horizontal
#6 horizontal	#3 90% horizontal

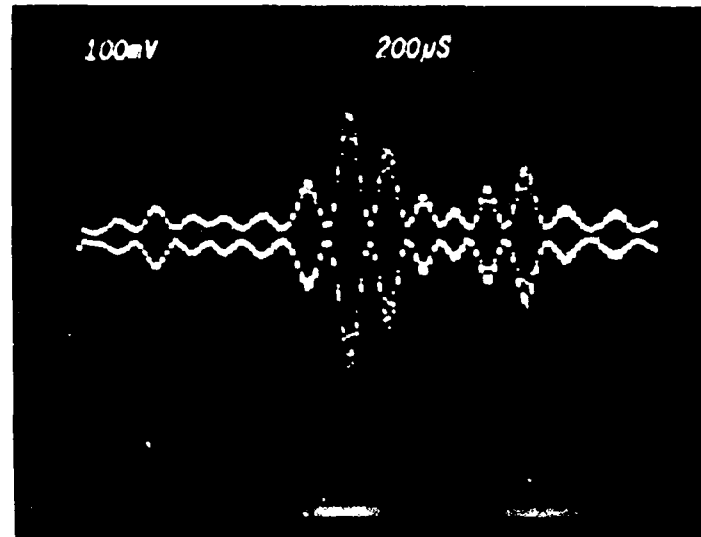
as defined in Figure 39. This indicated that there was not a strong polarization preference, hence, the losses due to the ZnSe and Macor SiO_2 glass/ceramic materials were nearly equal.

The copper mirror was then translated half-way between waveguides. Again folded cavity modes were observed. Figure 48 shows the folded cavity mode from channels #2 and #5. In 48a) there is a maximum at the center of the oscilloscope trace. By translating the concave mirror $\lambda/4$ in or out, the maxima and minima change places as shown in Figure 48b). No array-mode formation was found, as might be expected with the polarizations measured above.

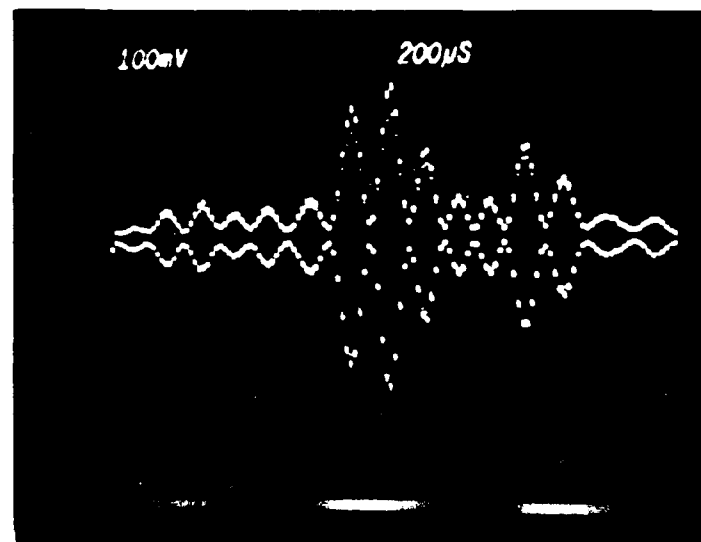
The polarizations of some folded cavity modes were found to be:

#2 and #5 vertical
#3 and #6 vertical
#2 and #3 horizontal

The TE polarization with respect to the plane-of-incidence at the spherical mirror is seen to have lower coupling loss than the TM polarization.



a) Detector Horizontal, $z = 52$ cm



b) Same with Small Displacement of Spherical Total Reflector

FIGURE 48. FOLDED CAVITY MODE, #2 AND #5, ZnSe WALLS,
9-INCH R.C. COPPER MIRROR

Placing the spherical mirror at the center of four waveguides (2, 3, 5, and 6) did not result in lasing. The diagonal coupling losses in conjunction with ZnSe wall losses were too large in this resonator configuration.

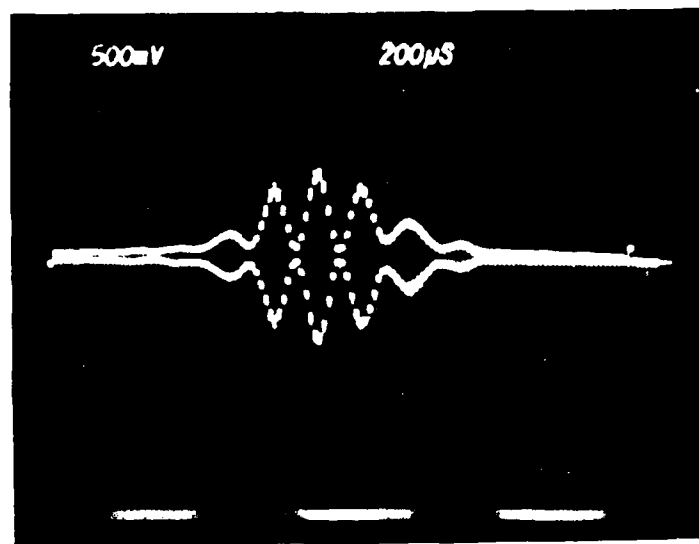
Next a ZnSe lens with 6.35 cm focal length and flat copper mirror were placed in the 1:1 position as before (See Figure 44). This resonator configuration had been demonstrated by Yaeli et. al³¹ to produce array-modes when used with AlGaAs semiconductor laser diode arrays. The experiment showed that the output from an array of phase-locked waveguide lasers can be viewed as a single array mode propagating outward symmetrically about the center of the array. Thus, an array-mode can be reflected using mirrors, gratings, lenses, or combinations thereof just as for a single HE_{11} mode. Thus, we had high hopes for this resonator configuration.

When the ZnSe lens was aligned sequentially with the individual waveguides (the flat mirror was aligned for all six), the following polarizations were observed:

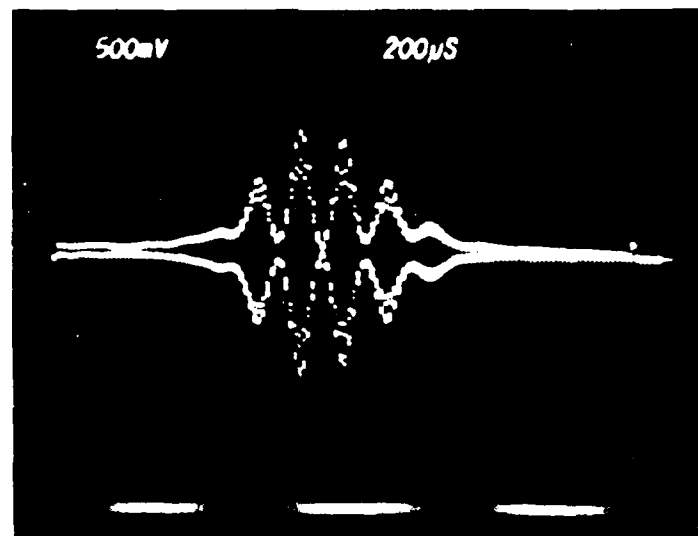
#4 vertical	#1 50/50
#5 horizontal	#2 horizontal
#6 horizontal	#3 50/50

Again no strong preferential polarization direction was exhibited. Also, near Gaussian mode patterns were observed for each waveguide.

When the lens was aligned between adjacent pairs of waveguides, folded cavity modes were again observed. Figure 49a) shows the folded cavity mode of channels #2 and #3. In 49b) the mirror is displaced $\lambda/4$ producing a $\lambda/2$ optical path length change, and the maxima switch to maxima and vice versa. These folded cavity modes were observed for all mirror positions as the flat reflector was translated toward or away from the waveguides over a range of about ± 12.5 mm. The polarizations of some of these adjacent folded cavity modes were found to be:



a) Detector Vertical, $z = 54$ cm



b) Same with Small Displacement of Flat Mirror

FIGURE 49. FOLDED CAVITY MODE, #2 AND #3, ZnSe WALLS,
LENS WITH FLAT COPPER MIRROR

#1 and #4 vertical
#3 and #6 vertical
#2 and #3 horizontal

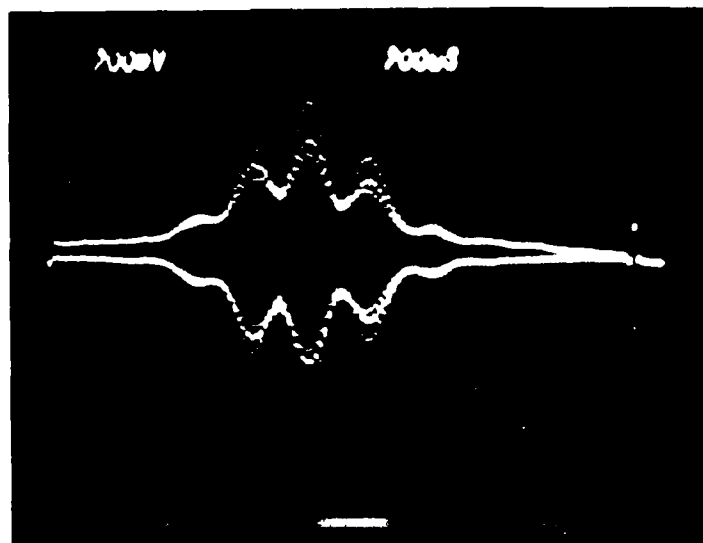
The ZnSe lens was then aligned between diagonally separated waveguides. Again folded cavity modes were found to dominate any array-mode formation. The polarization of some diagonal-folded cavity modes were:

#3 and #5 horizontal
#2 and #6 horizontal
#1 and #5 horizontal
#2 and #4 horizontal

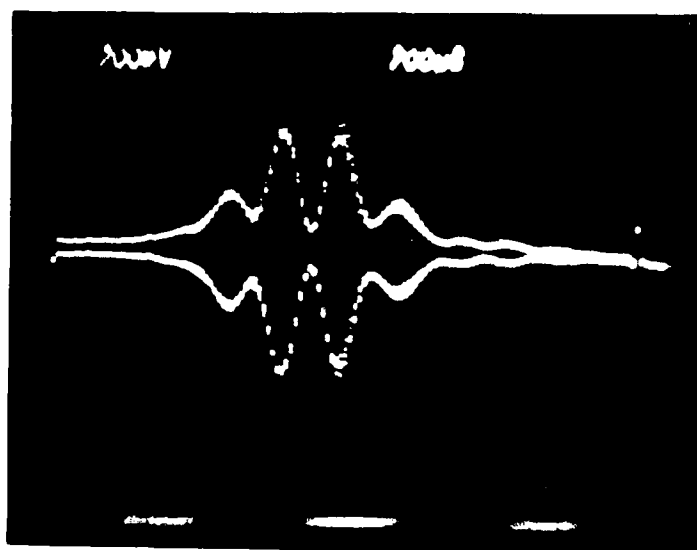
The horizontal polarization of all four diagonal-folded cavity modes showed that phase-locking could not have been prevented due to operation of the channels with orthogonal polarizations. It was possible, however, to achieve vertical polarization by small misalignments of the ZnSe lens.

Diagonal-folded cavity modes #2 and #6 and also #3 and #5 were then operated simultaneously. Two diagonal interference patterns were produced. These two sets of fringes did not phase-lock together and no array-mode was formed. Figure 50 shows a typical fringe pattern between #2/#6 and #3/#5. The nonzero interference minima is due to the fact that the two folded cavity modes did not phase-lock. This is in spite of the fact that the interaction length was $2 \times 20 \text{ cm} = 40 \text{ cm}$ along both the vertical and horizontal axes. No phase-locking was observed for any mirror separation distance.

A variable stop was then placed as close to the flat copper mirror as possible, about 1 cm away. The pupil was stopped as small as it would go (about 1 mm) to encourage array-mode formation by clipping the higher transverse mode components as was done in Reference 31. Phase-locking between the two diagonally folded cavity modes and array mode formation still did not occur for any mirror distance. Uncoupled folded cavity modes always dominated.



a) Detector Vertical, $z = 67$ cm



b) Same with Small Displacement of Flat Mirror

FIGURE 50. TWO DIAGONAL-FOLDED CAVITY MODES, #2/#6 AND #3/#5, ZnSe WALLS, LENS WITH FLAT MIRROR

Next the ZnSe lens was translated to the exact center of the array, and the pupil realigned. Longer diagonal-folded cavity modes, #1 and #6 as well as #3 and #4, were aligned for equal power. They were then operated simultaneously to observe the output mode patterns. Figure 51a) shows the two diagonal interference patterns with the pyroelectric array horizontal and near the center of the array. In Figure 51b) the upper two outputs, channels #1 and #4, are blocked by a razorblade, and the detector array was lowered to the centers of channels #3 and #6. No interference fringes between #3 and #6 were observed again indicating two diagonal folded cavity modes not phase-locked, hence, no array mode formation. The polarizations of these two modes were found to be:

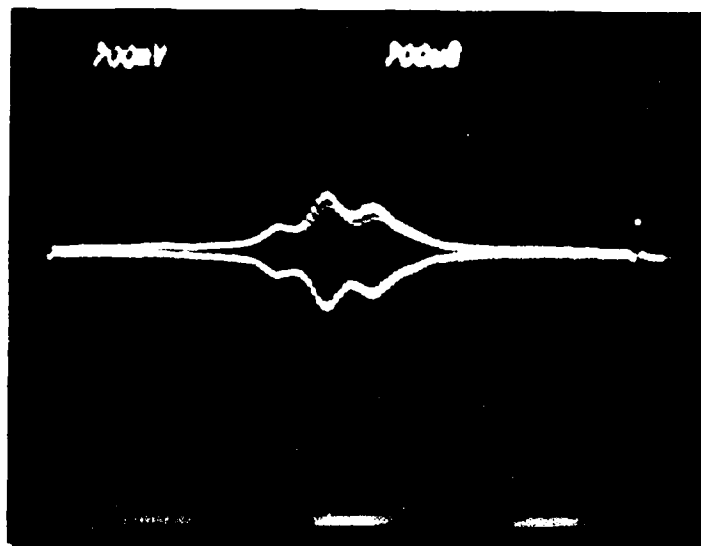
#1 and #6 vertical

#3 and #4 80% horizontal

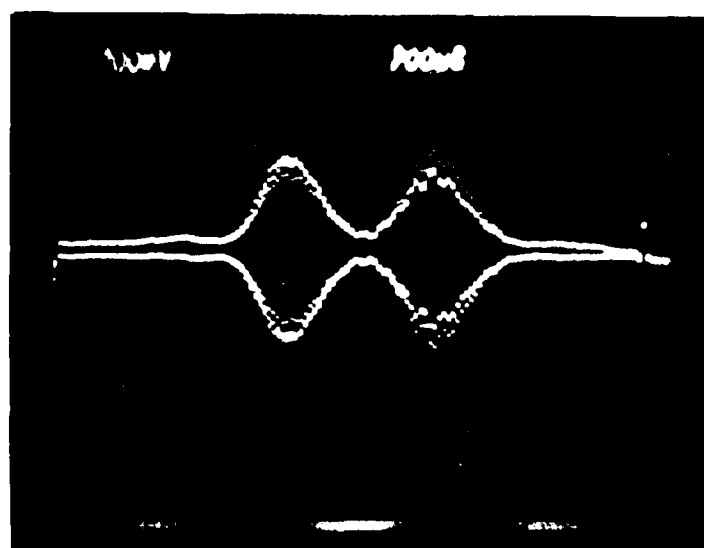
and the two polarizations were not optimum for phase-locking.

Next all six waveguides were operated simultaneously. Diagonal-folded modes #1/#6 and #3/#4 were turned on, and then a small current of about 1.5 mA was run through channels #2 and #5. The folded cavity mode #2/#5 having lower coupling losses than the two long diagonal-folded cavity modes would otherwise swamp the outputs of #1/#6 and #3/#4. The fringe pattern of #1/#6, #3/#4, and #2/#5 is shown in Figure 52a). With the pupil at its minimum opening, still no array-mode formation was found. The laser array operated with three independent folded cavity modes as shown.

All of the above measurements using a ZnSe lens and a flat copper mirror were repeated next using a 99% reflectivity output coupler. The increased intracavity flux should have produced a higher interwaveguide energy coupling, but the interference patterns were identical to the previous 95% reflectivity output coupler results. After this, all the tests were repeated using a 25-cm focal length lens and the flat copper mirror. Again identical far-field energy distributions were measured. Figure 52b) shows folded cavity modes #1/#6, #3/#4, and #3/#5 with a 99% reflectivity coupler and the 25-cm focal length lens. In Figure

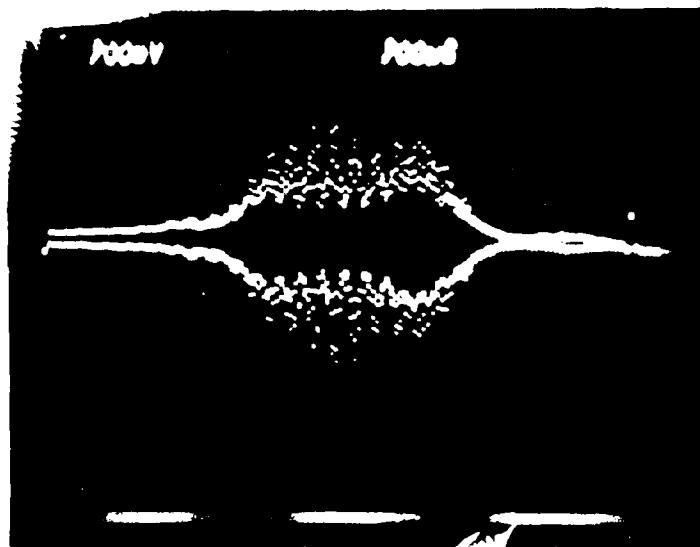


a) Detector Horizontal at Array Center, $z = 44$ cm

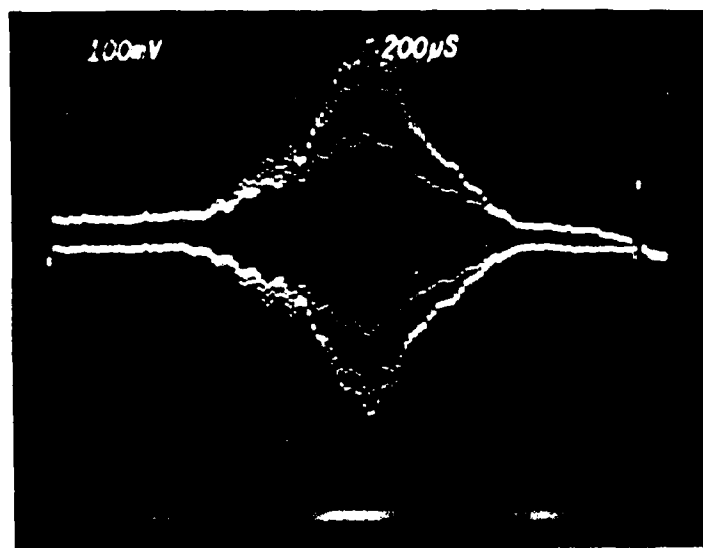


b) Detector Horizontal at Channel #3 and #6, $z = 44$ cm

FIGURE 51. TWO LONG DIAGONAL-FOLDED CAVITY MODES, #1/#6 AND #3/#4, ZnSe WALLS, LENS WITH FLAT MIRROR



a) Detector Horizontal, $z = 43$ cm, O.C. = 5%,
Focal Length 6.35 cm.



b) Same, $z = 53$ cm, O.C. = 1%, Focal Length 25 cm.

FIGURE 52. THREE FOLDED CAVITY MODES #1/#6, #3/#4, #2/#5,
ZnSe WALLS, LENS WITH FLAT MIRROR

55) the output of mode #3/#5 is somewhat higher than in Figure 52a) resulting in a higher central peak.

Also during this series of tests linear arrays of waveguide, #1, #2, #3, and #4, #5, #6, were tested for phase-locking and array mode formation. This was easily accomplished by translating the ZnSe lens to the center of either channel #2 or #4. Figure 53 shows the interference pattern of folded cavity mode #1/#3 using the 5% out-coupling and 6.35 cm focal length mirror. The current in channel #2 was then turned to a low value of about 1 mA so as not to swamp mode #1/#3, and the interference pattern was observed as shown in Figure 54. The pattern in Figure 54 is the interference pattern of folded cavity mode #1/#3 superimposed on the small Gaussian of #2. No phase-locking or array-mode formation was observed.

The polarization of both #1/#3 and #4/#6 were found to be horizontal, and from the previous measurements #2 and #5 were horizontally polarized as well. There was thus no polarization orthogonality to prevent phase-locking.

As a last effort with this resonator configuration, both the 6.35 cm and 25 cm focal length lenses were tried in the 2:2 configuration. As described in the Al_2O_3 interwaveguide plate experiments, it was a possibility that an array-mode would propagate as a spherical wave from the six apertures and thus behave as a geometrical optics wave front focusing in the 2:2 configuration. The optics were aligned as well as possible using the HeNe alignment laser, but no lasing was ever achieved. Reference 31 operated in the 1:1 configuration, however, indicating that an array-mode should propagate as a Gaussian although no folded cavity modes were reported in this article.

It should be emphasized that all of the folded cavity modes observed in the 1:1 configuration were not necessarily lasing on the same transition. Output powers were typically 100 mW per mode with a broad interference pattern between two waveguides, and they were too

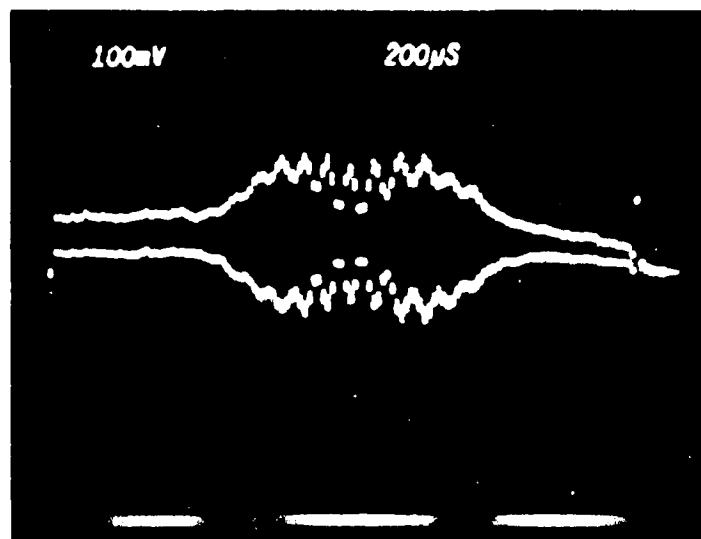


FIGURE 53. FOLDED CAVITY MODE #1/#3, VERTICAL DETECTOR,
5° O.C., FOCAL LENGTH 6.35 cm, $z = 54$ cm.

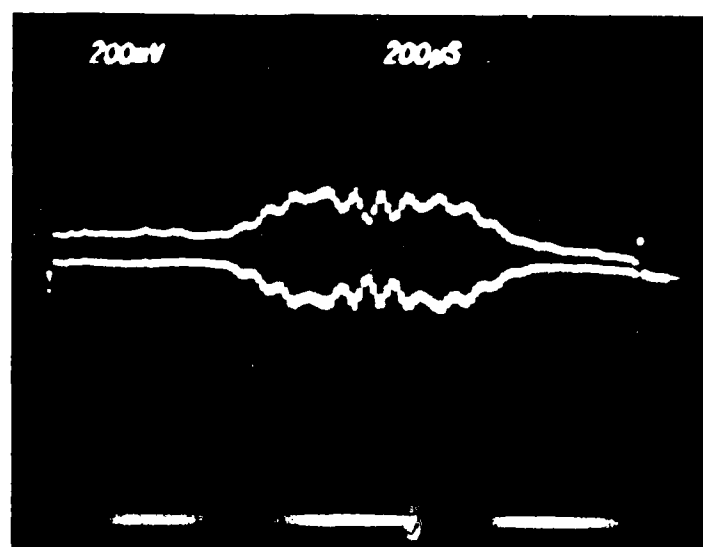


FIGURE 54. FOLDED CAVITY MODE #1/#3 AND #2, VERTICAL
DETECTOR, 1° O.C., FOCAL LENGTH 25 cm,
 $z = 58$ cm.

low power to observe with the CO_2 spectrum analyzer. However, we knew that the lasing lines ranged from P(12) to P(22) (or less because of higher losses) from the single copper mirror measurements. Consequently, by translating the flat total reflector by distances as large as ± 12.5 mm from the 1:1 configuration, at some point both or all three folded cavity modes must have been operating on the same laser transition. Nevertheless, no phase-locking of folded cavity modes was observed and thus, no array-modes could have been formed.

At this point it was decided to eliminate the folded cavity modes and the question of which line they were operating on by going directly to the reflection grating from the waveguide apertures. The increased diffraction losses would cause even more losses and, therefore, even lower powers but at least single line, single polarization could be assured based on the previous measurements. A new grating holder was fabricated to hold the grating as close as possible to the waveguide apertures, partially inside the endcap, which held the AR/AR window.

While the grating mount was being fabricated, a flat copper mirror was placed as close to the AR/AR window as possible, about 1.5 cm from the waveguide apertures. The individual polarizations were found to be:

#1 horizontal	#4 horizontal
#2 horizontal	#5 vertical
#3 horizontal	#6 80% vertical

Output powers were down to about 100 mW due to the coupling losses. All six waveguides could be operated simultaneously at these powers, however, and the far-field patterns were observed with pyroelectric array. Figure 55 shows the output of channels #4, #5, and #6. This is a noncoherent sum of the three Gaussians. The flat copper mirror was translated backwards up to about 5 mm before lasing ceased, but no interference fringes were observed during the continuous scan. At some point two channels must have been on the same transition, but no phase-locking was observed. Operation appeared as if there were no

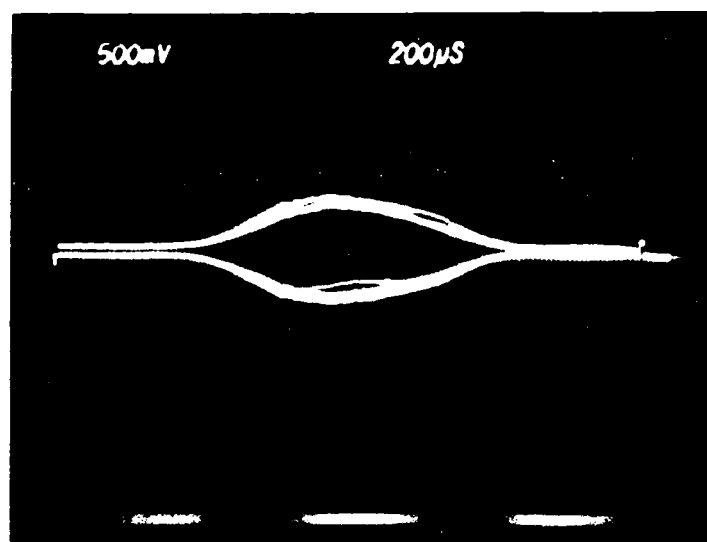


FIGURE 55. CHANNELS #4, #5, #6, ZnSe WALLS, FLAT MIRROR ONLY, 5% O.C., $z = 59$ cm.

interwaveguide coupling as in the Al_2O_3 interwaveguide plate test with flat reflectors.

When the grating mount with two axes of rotation and z axis translation was completed, the grating was installed and placed as close as possible to the six waveguide exit apertures. About 1.5 cm was the minimum waveguide aperture-to-grating distance allowable. Initially a 99% reflectivity output coupler was used for maximum intracavity flux. [Also, the zero order reflection from the grating represents almost 5% output coupling at the grating.]

The grating surface was rotated to be in the vertical plane, thus waveguides #1, #2, and #3, and the group #4, #5, and #6, were equidistant from the grating. The polarization of all channels was then in the horizontal plane due to the higher reflectivity perpendicular to the grooves as shown in Figure 22. Also, all channels were operating on a single transition as determined by the grating angle-of-incidence. This was shown in the earlier experiments with Al_2O_3 plates separating the waveguides.

Channels #4, #5, and #6 were found to lase weakly with about 100 mW power each due to the large coupling losses. No phase-locking or array-mode formation was observed, however. Instead, a noncoherent summation of Gaussian modes was found as shown in Figures 56 and 57. Figure 56 shows the noncoherent summation of channels #5 and #6. The grating was translated outward 5 mm continuously while maintaining lasing, but no interference fringes were observed. Figure 57 shows the outputs of channels #1 and #2. Because channels #1, #2, and #3 were further from the grating due to the grating angle, output powers were reduced to about 50 mW. Channels #1 and #2 showed no phase-locking either as the grating was translated outward.

A next attempt was made by going to a 96% reflectivity output coupler and trying the grating rotated by 90° . Figure 58 again shows noncoherent summation of channels #2 and #3 with 4% output coupling.

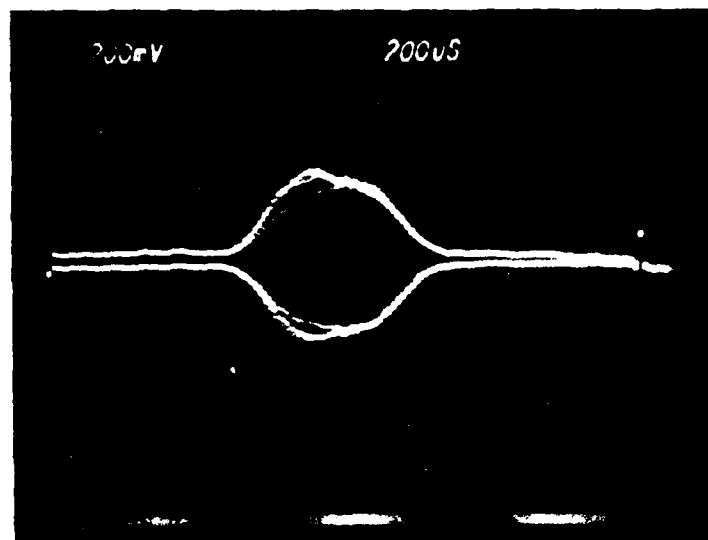


FIGURE 56. CHANNELS #5 AND #6, ZnSe WALLS, GRATING ONLY,
1% O.C., DETECTOR VERTICAL, $z = 47$ cm.

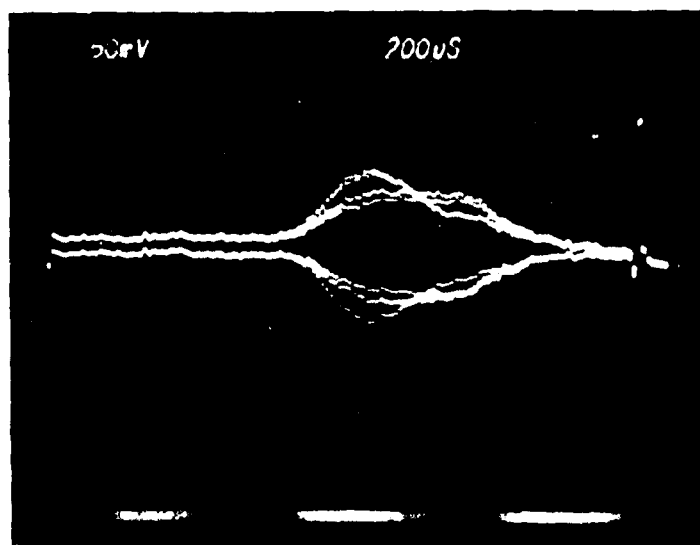


FIGURE 57. CHANNELS #1 AND #2, ZnSe WALLS, GRATING ONLY,
1% O.C., DETECTOR VERTICAL, $z = 52$ cm.

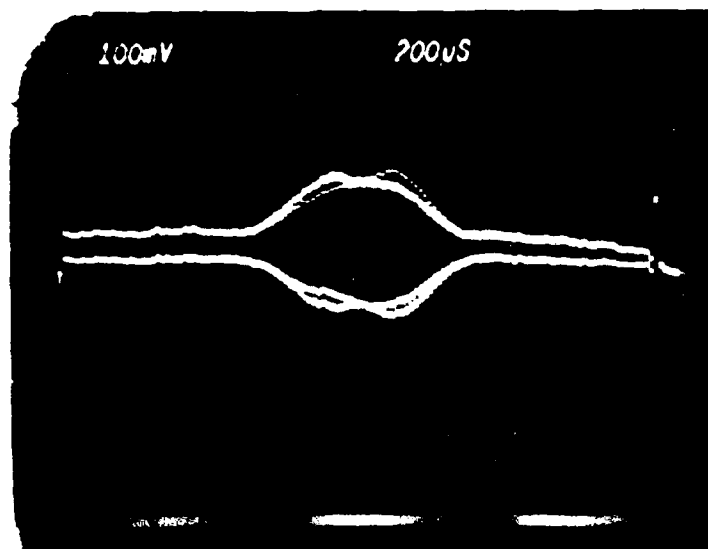


FIGURE 58. CHANNELS #2 AND #3, ZnSe WALLS, GRATING ONLY
4% O.C., DETECTOR VERTICAL, $z = 45$ cm.

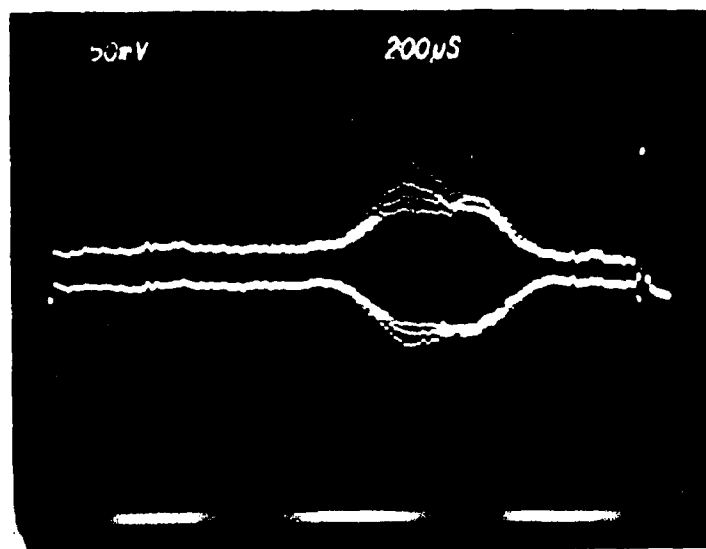


FIGURE 59. CHANNELS #2 AND #5, ZnSe WALLS, GRATING ONLY,
4% O.C., DETECTOR HORIZONTAL, $z = 45$ cm.

The grating was rotated 90° to shift polarization to the vertical plane and again noncoherent Gaussian summation was found. Figure 59 shows the outputs of channels #2 and #5 with the detector array horizontal; again a noncoherent Gaussian summation.

Summarizing, we see that in all the resonator configurations and with all the variable mirror separations tried, no phase-locking was observed. This must be attributable to the lack of interwaveguide coupling which was analyzed in Section 3.0. Recommendations for increasing this coupling, as well as another technique to achieve coherent beam addition, are disclosed in Section 7.0, Conclusions and Recommendations.

7.0 CONCLUSIONS AND RECOMMENDATIONS

During this Multiple Coupled Waveguide Laser Research effort, experimental hardware fabrication and analytical studies proceeded concurrently. After the midpoint of the contract period, the analyses of Section 3.2 and 3.3 were completed indicating very low optical coupling between waveguides and trapping of the radiation inside the optical quality ZnSe plates. At this point it was too late to modify the existing 1x7 or the nearly completed 2x3 devices to increase coupling. Hardware problems and time and funding constraints made this impossible. Also, in the previous 1x2 device shown in Figure 1 only four parts in 10⁴ was measured to leak through into the adjacent waveguide. Consequently, only very weak coupling should have been required to achieve phase-locking. Nevertheless, no phase-locking was observed in any of the resonator configurations tested. Table IV contains a list of the resonator configurations tested using the ZnSe walls.

TABLE IV. SUMMARY OF TESTED RESONATOR CONFIGURATIONS
USING ZnSe WALLS

Device	Flat Output Coupler (ρ)	Total Reflector
1x7	99%, 95%	Flat 2x20 mm mirror
1x7	99%	ML301 grating
2x3	99%, 95%, 90%	9 inch R.C. mirror
2x3	99%, 95%	6.35 cm f.l. lens/flat mirror
2x3	99%, 95%	25 cm f.l. lens/flat mirror
2x3	99%, 95%	Flat mirror
2x3	99%, 96%	6.35 cm f.l. lens/grating
2x3	99%, 95%	ML301 grating

It is thought that in the older 1x2 device, the clearly visible grain boundaries in the non-optical quality ZnSe walls scattered the leaked radiation at various angles into the adjacent waveguide. This then resulted in phase-locking as shown in Figure 3.

Indeed, contrary to what we initially thought, the results of Section 3 indicate that wall thickness is a second-order effect. The ZnSe walls should have been made thicker so that fewer plates (preferably one) could be used to separate the waveguides. This would have greatly reduced discharge cross-coupling which severely reduced simultaneous laser power. These lower simultaneous flux levels also reduced the waveguide coupling energies. In addition, the ZnSe plates should be a half-integer multiple $\lambda/(\epsilon_1/\epsilon_2 - 1)^{1/2}$ in thickness for optimum in-phase coupling as discussed in Section 3.0. The use of transverse or longitudinal RF excitation would reduce discharges through gaps and around the interwaveguide plates resulting in higher output powers.

In order to increase coupling of the leaked radiation into the adjacent guide, the ends of the interwaveguide plates should be beveled at about 45° to reflect the leaked radiation directly into the adjacent waveguide. Alternatively, it may be possible to put an anti-reflection coating on the plates to increase transmission of the internal leaked light at the almost critical angle of incidence shown in Figure 6. These unusual AR coatings have not been investigated.

Lastly, the concept of leaking radiation from one waveguide to another to achieve phase-locking may be superseded by the recent work of Veldkamp at Lincoln Laboratory³² with laser diode arrays. In this technique a binary phase grating is numerically designed to combine the outputs of an $n \times m$ array of lasers. The concept is shown in Figure 60. The individual waveguides can be made of low loss Al_2O_3 or BeO with no coupling and low distributed loss (compared to the ZnSe wall losses), and then combined at the phase grating as shown. The phase grating is located near a large beam waist so that flux density would be low. The

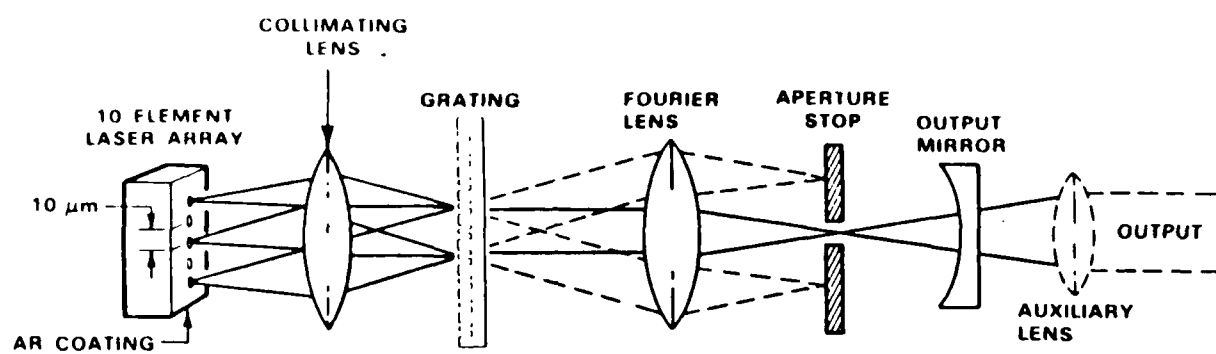


FIGURE 60. BINARY PHASE-GRATING COMBINATION RESONATOR
FOR $n \times m$ ARRAY OF WAVEGUIDE LASERS³²

individual lasers could be physically separated so that individual actuators would be easy to implement. It appears at the present time that the phase grating nxm combining of waveguide CO₂ lasers may offer a more mechanically tractable solution to obtaining coherent outputs of greater than 50 watts.

REFERENCES

1. Marcatili and Schmeltzer, "Hollow Metallic and Dielectric Waveguides for Long Distance Optical Transmission and Lasers," BSTJ, July 1964, p. 1783.
2. Abrams and Bridges, "Characteristics of Sealed-Off Waveguide CO₂ Lasers," IEEE JQE, Vol. 1, QE-9, No. 9, Sept. 1973, p. 940.
3. Abrams, "Coupling Losses in Hollow Waveguide Laser Resonators," IEEE JQE, Vol. QE-8, Nov. 1972, p. 838.
4. Krammer, "Field Configurations and Propagation Constants of Modes in Hollow Rectangular Dielectric Waveguides," IEEE JQE, Aug. 1976, p. 505.
5. Laakman and Steier, "Waveguides: Characteristic Modes of Hollow Rectangular Dielectric Waveguides," Applied Optics, Vol. 15, No. 5, May 1976, p. 1334.
6. Henderson, "Waveguide Lasers with Intracavity Electro-Optic Modulators: Misalignment Loss," Applied Optics, Vol. 15, No. 4, April 1976, p. 1066.
7. Degnan and Hall, "Finite Aperture Waveguide Laser Resonator," IEEE JQE Vol. QE-9, No. 9, Sept. 1973, p. 901.
8. Hill and Hall, "Coupling Loss Theory of Single Mode Waveguide Resonators," Appl. Opt., Vol. 24, No. 9, 1 May 1985.
9. Rigrod, "Saturation Effects in High Gain Lasers," Journal of Applied Physics, Vol. 36, Aug. 1965, p. 2487.
10. Casperson, "Laser Power Calculations: Sources of Error," Applied Optics, Vol. 19, No. 3, 1 Feb 1980, p. 422.
11. Carter and Marcus, "A High-power CO₂ Waveguide Laser," Appl. Phys. Lett., Vol. 35, No. 2, 15 July 1979.
12. Ripper and Paoli, Appl. Phys. Lett., Vol. 17, 1970, pg. 371.
13. Katz, Margalit, Yariv, Appl. Phys. Lett., Vol. 42, 1983, pg 554.
14. Scrifes, Burnham, Lindstrom, Streifer, Paoli, Appl. Phys. Lett., Vol. 42, 1983, p. 645.
15. Ackley and Engleman, Appl. Phys. Lett., Vol. 39, No. 1, July 1981, p. 27.

16. Streifer, W., Burnham, R., Scrfes, D., "Substrate Radiation Losses in GaAs Heterostructure Lasers," IEEE JQE, Vol QE-12, No 3, March 1976.
17. Scrfes, D., Streifer, W., Barnham, R., "Leaky Wave Room Temperature Double Heterostructure GaAs: GaA(As Diode Laser," Appl. Phys. Lett., Vol 28, No 1, 1 July 1976.
18. Ackley, D., Engleman, R., "High-power Leaky-mode Multiple-stripe Laser," Appl. Phys. Lett 39(1), 1 July 81.
19. Ackley, D., Engleman, R., "Twin-stripe Injection Laser with Leaky-mode Coupling," Appl. Phys. Lett. 37(10), 15 Nov 80.
20. Butler, J., Kressel, H., Ladany, I., "Internal Optical Losses in Very Thin CW Heterjunction Laser Diodes," IEEE JQE, Vol QE-11, 7, July 1975.
21. Butler, J., Ackley, D., Rotez, D., "Coupled Mode Analysis of Phase-locked Injection Laser Arrays," Appl. Phys. Lett., 44,(3), 1 Feb. 1984.
22. Kapon, E., Katz, J., Yariv, A., "Supermode Analysis of Phase-locked Arrays of Semiconductor Lasers," Optics Lett. 10,(4), April 1984.
23. Yariv, A. "Coupled Mode Theory for Guided-Wave Optics," IEEE JQE, 9,(9), Sept. 1973.
24. Hadley, G., "Cavity Supermodes for Gain-saturated Diode Laser Arrays," J. Appl. Phys., 58,(1), 1 July 1985.
25. Chen, K., Wang. S., "Spatial Hole Burning Problems in Evanescently Coupled Semiconductor Laser Arrays," Appl. Phys. Lett., 47, (6), 15 Sept 1985.
26. Hardy, A., Streifer, W., "Couple Mode Theory of Parallel Waveguide," J. Lightwave Tech., LT-3, (5), October 1985.
27. Gaskill, "Linear Systems, Four Transforms, and Optics," Chapter 10, John Wiley & Sons, Inc., 197
28. Vidaud, P., Hall, D., J. Appl. Phys 1 March 1985.
29. Youmans, D., "Phase-Locking of Adjacent Channel Leaky Waveguide CO₂ Lasers," Appl. Phys. Lett. 44(4), 15 Feb 1984.
30. Self, S. A., "Focusing of Spherical Gaussian Beams," Appl. Opt., 22, No. 5, 1 March 1983.

31. Yaeli, et al., "Array Mode Selection Utilizing an External Cavity Configuration," Appl. Phys. Lett. 47, No. 2, 15 July 1985.
32. Leger, Swanson, Veldkamp, "Coherent Beam Addition of GaAlAs Lasers by Binary Phase Gratings," Appl. Phys. Lett. 48(14), 7 April 1986.

END

4-87

DTIC